

DISS. ETH No. 25647

Nanoparticle levitation for the study of short-range interactions

A thesis submitted to attain the degree of
DOCTOR OF SCIENCES OF ETH ZURICH
(Dr. sc. ETH Zurich)

presented by

ROZENN EMELINE DIEHL

M. Sc. in Nanoscale Engineering, Ecole centrale de Lyon
born on 28.09.1991
citizen of France

accepted on the recommendation of
Prof. Dr. Lukas Novotny, examiner
Prof. Dr. Rachel Grange, co-examiner
Dr. James Millen, co-examiner

2018

*The only thing greater than the power of the mind
is the courage of the heart.*

– **John Nash**

Abstract

For centuries, scientists have been studying macroscopic forces, for instance by witnessing the motion of stars and planets, or the fall of an apple. But the twenty-first century has brought miniaturization and therefore the need to also investigate forces that act at the micro- and nanoscale. Force sensors have developed alongside, to become ever more sensitive. In this thesis, we use a nanoparticle, levitated with light very close to a surface, as a force sensor. Receiving the Nobel prize in Physics in 2018, optical levitation is perfectly suited for sensing due to the object's isolation from the environment, and the precise control we have over the levitated object. We develop a protocol for the precise positioning of a levitated dielectric particle at submicron distance from a planar surface, in order to measure short-range forces. We experimentally measure the separation between the sensing particle and the surface using an imaging method based on interferometry. Beyond measuring the particle-to-surface distance, we control it using an optical conveyor belt scheme. The ability of varying this distance is a requirement for the investigation of surface forces, that scale strongly with the separation between the two objects. However, these surface forces are weaker than the optical forces that trap the nanoparticle. Therefore, we employ a recently developed method, the free-fall of nanoparticles, that allows the trapping light to be switched off for a short time during the force measurement. We present an experiment that is the first step towards the application of our system for short-range forces measurement.

Résumé

Historiquement, la science est une discipline largement fondée sur l'observation, aussi les scientifiques ont-ils pu étudier les forces macroscopiques à l'oeuvre dans le mouvement des astres ou la chute d'une pomme. Toutefois, depuis plus d'un siècle la tendance à la miniaturisation encourage les chercheurs à approfondir notre compréhension du petit, du micro, du nanoscopique et notamment des forces intervenant à ces échelles. Les capteurs ou outils de mesure de ces forces invisibles à l'oeil nu évoluent alors eux aussi, gagnant en sensibilité et en précision.

Dans cette thèse, nous utilisons pour capteur une nanoparticule maintenue en lévitation à très faible distance d'une surface plane, par un laser. Reconnue par le Prix Nobel de Physique 2018, la lévitation optique est une technique parfaitement adaptée à la mesure des forces microscopiques puisqu'elle permet une isolation des perturbations extérieures ainsi qu'un contrôle précis de l'objet en lévitation. Nous mettons en place un protocole permettant de positionner précisément la nanoparticule à une distance submicronique de la surface plane, afin de mesurer les forces à courte portée. La distance entre la nanoparticule et la surface est mesurée expérimentalement à l'aide d'une méthode d'imagerie basée sur l'interférométrie. Cette distance est non seulement mesurée mais également contrôlée par un procédé de convoyeur optique. La capacité à faire varier cette distance est fondamentale à l'étude des forces de surface, fortement dépendantes de la distance entre les deux objets. Cependant ces forces de surface sont plus faibles que les forces optiques maintenant la nanoparticule en lévitation. Par conséquent, nous employons une méthode développée récemment, dite de chute libre des nanoparticules, nous permettant d'éteindre le laser du piège optique pendant une très courte durée, durant laquelle la mesure des

RÉSUMÉ

forces est réalisée. Le travail que nous présentons a pour ambition d'être un premier pas vers l'application de notre système pour la mesure des forces à courte portée.

Contents

Abstract	iii
Résumé	v
1 Introduction	1
2 Particle trapping in vacuum	7
2.1 Experimental setup	7
2.1.1 Optical setup	8
2.1.2 Detection of the particle motion	10
2.1.3 Vacuum setup	12
2.1.4 Trapping protocol and particle discharging	13
2.2 Trapping theory	16
2.2.1 Optical forces	16
2.2.2 Particle dynamics	20
2.2.3 Detecting the light scattered by the particle	23
2.2.4 Calibration of the particle motion	28
3 Approaching particles to planar surfaces	31
3.1 Experimental realization	32
3.1.1 Addition of the membrane	32
3.1.2 Determination of the membrane position relative to the focus	33
3.2 Potential mapping at large distances	36
3.2.1 Measurement of the trapping potential at large distances	37

3.2.2	Theoretical model: large distances analysis . . .	40
3.3	Potential mapping at short distances	47
3.3.1	Measurement of the trapping potential at short distances	48
3.3.2	Theoretical model: short distances analysis . . .	55
3.4	Conclusion	63
4	Interferometric measurement of distances	65
4.1	Experimental setup	66
4.2	Interferometric measurement	67
4.2.1	Back-focal-plane imaging: results and model . .	67
4.2.2	Measurement of d_{part} during the membrane ap- proach	72
4.3	Conclusion	79
5	Active control of the particle-to-surface distance	81
5.1	The optical conveyor belt concept	82
5.2	Experimental setup	82
5.3	Theoretical considerations	83
5.4	Experimental tuning of d_{part} with a conveyor belt . . .	87
5.5	Conclusion	88
6	Towards sensing of surface forces	91
6.1	A free-falling particle as a force sensor	93
6.2	Feedback cooling the center-of-mass motion of a particle	95
6.3	Free-fall measurement without surface	98
6.4	Perspectives	103
7	Outlook	107
7.1	Integrating optical traps on a chip	108
7.2	Radiative heat transfer at the microscale	109
7.3	Vacuum friction	112

Contents

List of Symbols	115
List of Figures	119
References	123
List of Publications	137
Curriculum Vitae	139

Chapter 1

Introduction

Deriving from the greek word for dwarf, the prefix *nano* is nowadays spreading beyond the scientific laboratories to enter our everyday life. The development of technologies is increasingly oriented towards miniaturization, reaching length scales of nanometers [1]. As devices become always smaller, new physical phenomena come into play and need to be investigated. At the nanoscale, the predominant players are short-range forces, such as the Van der Waals force, the Casimir force, the strong force or the weak force [2, 3]. In every scientific community, from biology to chemistry to quantum physics, understanding the interactions at the nanoscale level is of crucial importance, as these interactions for example dictate the structuring of matter, and therefore also the properties of materials. In order to understand these interactions, we need to measure them, a non-trivial task due to the fact that they fall off very quickly with increasing distance.

Amongst these short-range forces, there is the Van der Waals force. It is an attractive force between two objects, originating from the existence of vacuum fluctuations [4]. For example, the Van der Waals force is what binds graphene sheets together to make graphite. We

refer to the Van der Waals force when we investigate the interactions between atoms or molecules that are separated by a few nanometers maximum. When we consider objects with a separation exceeding a few nanometers, we refer to the same force as Casimir force [5]. Even though the Casimir force becomes negligible beyond a few microns separation, it is of relevance for everyday life applications, such as smartphones, inkjet printers or hard drives [6, 7]. Indeed, the effects of Casimir forces play a important role in the fabrication of micro/nano-electromechanical devices (MEMS/NEMS) where the size of the elements and the distance between them reach the submicron scale [8].

There are two different regimes where the Casimir force is well understood and has been extensively studied. We refer, amongst the two bodies subject to the Casimir force, to one as a sensor, that senses the Casimir force resulting from the presence of the second body. The two regimes are distinguished by the scaling of the sensor size l in relation to the separation length L , *i.e.*, either $l \gg L$ or $l \ll L$. The first regime, where the sensor size is much bigger than its separation to the second body ($l \gg L$), is called the regime of proximity force approximation (PFA) [9]. Systems such as a metal-coated sphere on an atomic force microscope (AFM) cantilever [10, 11, 12], where the deflection of the cantilever due to Casimir forces is measured, or micro-machined oscillators [13, 14], where the frequency change due to the Casimir forces is detected, allow the investigation of Casimir forces within the PFA. They also enable the study of corrections to the theory due to real metal properties, surface roughness, different configurations or temperature-induced modifications [15].

The other regime occurs when the separation L between the two objects subject to the Casimir force is much larger than the sensor size l , *i.e.*, $l \ll L$. As Casimir forces have an effect solely over short distances, scientists turned to atoms as a sensor due to the small size of atoms. Atom clouds [16], Bose-Einstein condensates [17], which consist of a large number of optically levitated atoms, or atomic beams [18]

have been utilized for such a purpose due to their high sensitivity to forces. Nevertheless, the intermediate regime, *i.e.*, when the separation is of the order of the sensor size, has remained unexplored and lacks a theoretical understanding to date [19].

Optically levitated dielectric nanoparticles [20, 21], *i.e.*, particles spatially confined in the focus of a laser beam, constitute a very good force sensing system due to the decoupling from the environment, in contrast to mechanically clamped nano-devices (except for specifically engineered structures using soft clamping [22]). Historically operated first in liquids or in air at atmospheric pressure, optical tweezers allow the measurement of biologically relevant forces [23, 24], rewarding Arthur Ashkin, the father of optical tweezers, with the Nobel prize in Physics in 2018 [25]. However, in this overdamped regime, the impact of the environment on the particle is still too significant for the detection of weak forces such as the Casimir force. The outstanding force sensitivity of optical levitation unfolds when used in vacuum [26]. Indeed, in vacuum (underdamped regime), the particle oscillates in the trap and the damping the particle experiences can not only be dramatically reduced but also finely tuned by controlling the surrounding gas pressure. The particle position can also be accurately determined and controlled via the trapping laser field [27, 28, 29, 30], yielding an unprecedented sensitivity to weak forces for vacuum levitated sensors [31, 32, 33, 34, 35]. By positioning a levitated dielectric nanoparticle with a diameter of a few hundreds of nanometers at a submicron distance from a surface, the study of Casimir forces in the intermediate regime therefore becomes possible [19].

However, placing a surface in close proximity from a levitated particle in order to sense surface forces is a non-trivial task. Indeed, the presence of the surface will disturb the trapping field. The reflection of the trapping light from the surface generally creates a standing wave-like intensity distribution [36, 37, 38, 39]. It has recently been realized that optically levitated nanoparticles in such a configuration

are sensitive enough to measure weak forces [36, 39, 40].

Outline of the thesis

In this thesis, we develop an experimental technique to position an optically levitated nanoparticle at a subwavelength distance from a dielectric interface. With optical levitation of dielectric particles being at the heart of this work, Chap. 2 is devoted to a review of the principle of optical trapping of dielectric nanoparticles. We introduce the experimental setup to perform optical trapping, and explain the strongly focused beam theory that applies in our conditions. With the goal to bring the levitated particle in close proximity to a surface, we study the consequences of introducing a dielectric membrane in the beam path after the particle in Chap. 3. The experimental modifications compared to a standard optical trap are described as well as how the membrane position is calibrated. We then investigate, for the first time in vacuum, the effects of the membrane on the optical potential and therefore on the particle dynamics when the membrane is far away and when it is close to the particle in two successive sections. First, the experimental results are presented, followed by the corresponding theoretical description, providing a comparison between theory and experiments. We conclude by discussing the limitations of our theoretical model.

Because the particle is used as a probe to map out the optical potential, it is of crucial importance to know the absolute distance between the particle and the membrane. We use an interferometric measurement technique in Chap. 4 to determine the absolute distance between the particle and the membrane, independently from the optical trap. Together with the experimental results, we present a theoretical model used to analyze the interference patterns and extract the distance between the particle and the membrane. We address at the end the

existence of the Gouy phase for focused beams and its implication in our results.

In addition to the measurement of the particle-to-surface distance, we are interested in gaining more control over this distance. To this end, we present a technique based on phase modulation in Chap. 5, liberating us from the stationary standing wave restrictions that dictate the position of the particle regarding the surface.

Having established a powerful sensing system with a levitated nanoparticle at a precisely measured submicron distance from an interface, we propose an experiment inspired by Ref. [41] in Chap. 6, that should enable the measurement of short-range surface forces. We introduce the feedback cooling scheme used to cool the center-of-mass motion of the particle [27], provide a proof-of-principle of the Casimir force measurement, and suggest an experimental realization.

Besides the sensing of short-range forces, the precise positioning of a levitated dielectric nanoparticle at a subwavelength distance from an interface developed in this thesis can be utilized for other applications. To this end, in the outlook, we discuss the benefit of our system in thermodynamics studies and in the development of building blocks for integrated photonic circuits.

Chapter 2

Particle trapping in vacuum

In this chapter, we review the standard optical trap for dielectric nanoparticles that has been extensively studied and constitutes the state-of-the-art of optical levitation in vacuum [19, 27, 28, 29, 42, 43, 44, 45, 46, 47, 48]. We first introduce the standard experimental setup, measurement techniques, and trapping protocols that are common in many optical trapping experiments. In the second part, we summarize the theoretical background necessary to understand optical trapping and particle detection. We finish by explaining the calibration method used to measure the particle position (in nm) (detailed and discussed in Ref. [49]).

2.1 Experimental setup

To experimentally levitate a dielectric nanoparticle in vacuum and to control its motion and charge state, we need an optical setup that includes

- an optical trap formed by a laser beam focused through a lens or an objective,
- a detection system to read out the position of the trapped particle as a function of time,
- a vacuum chamber, equipped to measure and control the pressure and thus the damping the particle experiences, and
- a charge control system, to monitor and modify the charge-to-mass ratio of the levitated sphere.

All these elements will be detailed in the following sections of this chapter. Whenever elements need to be added to the standard vacuum levitation setup for a specific experiment, they will be introduced in the corresponding chapter.

2.1.1 Optical setup

All the experiments in this thesis are carried out on an optical table, floating on vibration-isolating legs to hinder vibrations from the outside from coupling to the optical setup. A schematic of the setup is shown in Fig. 2.1. The trapping laser is a solid state Nd:YAG laser¹, emitting at a wavelength of 1064 nm with a 1 kHz linewidth. This particular wavelength was chosen because it has proven to be suitable for particle trapping in vacuum [43]. The relative intensity noise (RIN) of this laser is specified to be below -140 dB/Hz. A low RIN is important because a fluctuation in the intensity results in an uncontrolled modulation of the optical trap, which can lead to heating of the particle's center-of-mass motion [50]. The laser beam is sent into a polarization-maintaining single-mode fiber (PMSM) to clean the profile of the beam and to improve its pointing stability. A careful alignment of this optical

¹Coherent Mephisto 2W

2.1. Experimental setup

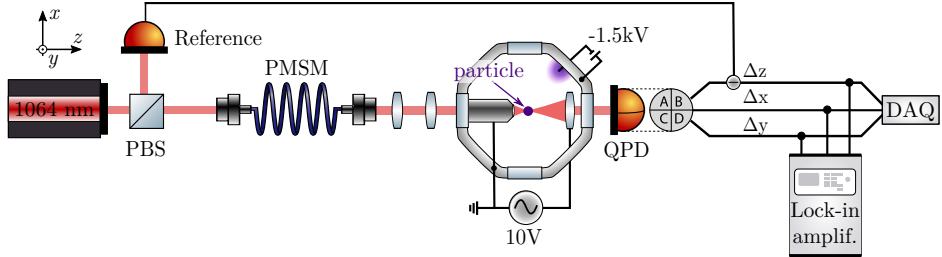


Figure 2.1: Schematic of the basic optical trapping setup with the charge control system. A silica nanoparticle is trapped inside a vacuum chamber in the focus of a laser beam (1064 nm), which is spatially filtered by a polarization-maintaining single-mode fiber (PMSM). A telescope then expands the beam to match the objective’s back aperture size. The forward-scattered light from the nanoparticle is detected by a quadrant photodetector (QPD). While the detection along the transverse directions is self balanced through alignment, the detection along the optical axis direction requires a reference beam picked up before the trap, using a PBS. The signals from the QPD are sent to a lock-in amplifier and recorded by a data acquisition card (DAQ) as a function of time. The recorded time traces represent the particle motion. To monitor the charge-to-mass ratio of the particle, we create a capacitor with the grounded objective and the metallic holder of the collection lens as capacitor plates. We apply a sinusoidal voltage of amplitude 10 V between those plates. To control the charge-to-mass ratio, we create a plasma by applying -1.5 kV to a wire inside the chamber. Free charges are generated and eventually collide with the trapped particle, modifying its charge.

fiber (using a half-wave plate placed before the fiber and a polarizer after the fiber [51, pp. 11f.]) is necessary to minimize temperature or strain-induced intensity fluctuations at the output of the PMSM. We place a telescope after the fiber to match the beam size to the back aperture of the objective. The polarization of the trapping beam may be controlled by adding additional wave plates in the beam path (not drawn here). A high numerical aperture (NA) objective provides a strong confinement of the trapping field. Throughout this thesis, we

2. PARTICLE TRAPPING IN VACUUM

use a Nikon objective². Only in Chaps. 5 and 6 do we use an Olympus objective³. The optical power in the focus is around 100 mW.

In the laser focus, we trap silica nanoparticles⁴ of nominal radius 68 nm. Silica is well suited for trapping at visible and near-infrared (NIR) wavelengths because it has a low absorption [52], leading to minor heating under the illumination of a laser beam. The nanoparticles are provided in a monodisperse solution, which we dilute with isopropanol. We use a nebulizer⁵, which consists of a 2- μ m mesh attached to a piezoelectric actuator. It produces small droplets of the liquid solution. These droplets are sprayed inside the chamber, close to the laser focus. As a drop with a particle inside falls towards the focus, the isopropanol evaporates and the particle can be trapped. Assuming a drop volume of about 10 fL, we have adjusted the dilution concentration such that we expect one silica nanoparticle per drop [42, p. 35].

2.1.2 Detection of the particle motion

To detect the particle motion, we collect the forward scattered light from the particle with a collection lens. To collect the maximum of the light, we use a high NA lens (NA = 0.83). This lens is placed such that its focus coincides with the particle position, so that the light from the focus of the objective (light from the particle and forward propagating trapping beam) is transformed into a collimated beam by the collection lens. We then send this beam onto our quadrant photodetector (QPD). For the detection of the motion along the optical axis z , we pick up a reference beam with a polarizing beam splitter (PBS) before the

²TU Plan Fluor 100x (NA = 0.9, focal length $f = 2$ mm, working distance = 1 mm)

³100x (NA = 0.85, focal length $f = 1.8$ mm)

⁴microparticles SiO₂-R-L2902

⁵Omron MicroAir U22

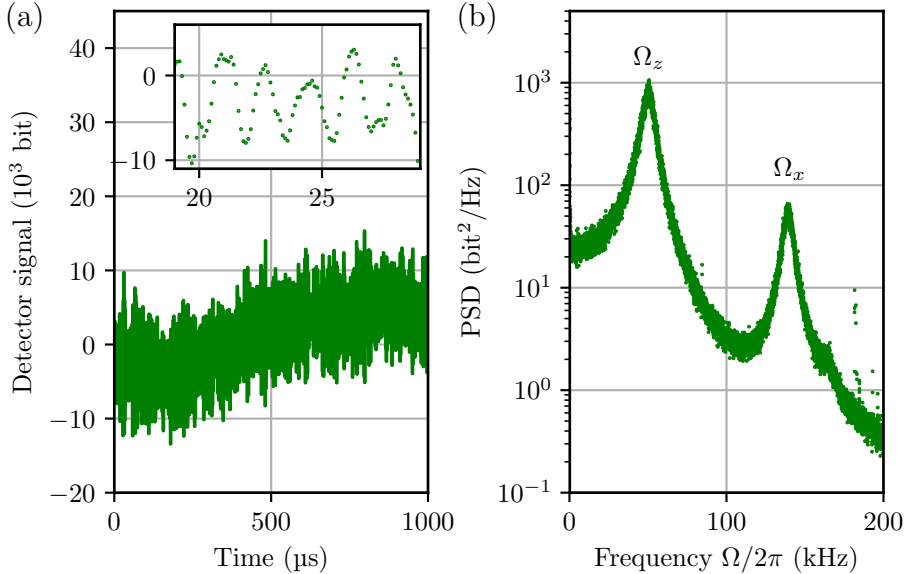


Figure 2.2: (a) Time trace of the particle motion recorded at 10 mbar on the z -detector. (b) PSD obtained by Fourier transforming the time trace in (a). We distinguish the oscillation peak of the z -mode at 50 kHz but also the peak corresponding to the oscillation along x (around 140 kHz) which appears due to optical cross-talk.

PMSM, as shown in Fig. 2.1, to perform the balanced detection [43]. The electronic signals are then sent both to a lock-in amplifier⁶ and to a data acquisition card⁷ to record the voltages from the detector, which are proportional to the particle position.

Figure 2.2(a) shows a sample of a typical time trace of the particle position from the z -detector, recorded at 10 mbar. The inset shows the motion on a shorter time scale so that we can observe the oscillations of the particle. As we are interested in the oscillation frequencies, we

⁶Zurich Instruments HF2LI

⁷GaGe card CSE4342

transform the time trace into Fourier space and calculate the power spectral density [43, 42, 44] [see also Sec. 2.2.2], plotted in Fig. 2.2(b). We observe an oscillation along the optical axis z at around 50 kHz. We also see the peak corresponding to the x -mode at $\Omega_x \approx 2\pi \times 140$ kHz because of optical cross-talk. Indeed, a slight misalignment of the laser beam at the photodetector, in this case an imbalance between left and right half of the QPD, or a slight misalignment of the collection lens, results in the z -channel of the detector being also sensitive to the motion along x .

To perform any quantitative measurements, we need a calibration factor to translate a voltage or a digital signal in bits into a particle displacement in nm. This calibration step is crucial. Indeed, it is needed to calculate the energy of the particle or the amplitude of the oscillation. A detailed study of the calibration process has been done in Refs. [42, 49] and we will explain the methods used for this thesis in Sec. 2.2.4.

2.1.3 Vacuum setup

The optical trap and the collection lens are placed in a vacuum chamber⁸. The pressure inside the chamber is controlled by two pumps (a backing and a turbo pump⁹) and is monitored with a gauge¹⁰ with an accuracy of $\pm 10\%$. This gauge uses a combination of Pirani and hot cathode sensors. The Pirani sensor, used for high pressures, measures the heat conduction of gases with a heated wire and infers the total gas pressure from the resistance of the wire. The hot cathode sensor, used typically for pressures lower than 10^{-4} mbar, ionizes the gas by electron bombardment, attracts the ionized gas molecules to an electrode, and measures the resulting current which is proportional to the

⁸Kimball Physics MCF600-SphOct-F2C8

⁹Edwards T-STATION 75

¹⁰Smartline Vakuum Transmitter VSH89DL from Thyracont

gas pressure [53]. The generation of free charges during this pressure measurement plays an important role since it can eventually impact our measurements, as we will explain in Chap. 6. With our system, we can reach a pressure of 10^{-7} mbar inside the vacuum chamber. Controlling the pressure enables us to tune the gas damping the particle experiences. We can therefore transition from the overdamped regime, where the particle only undergoes Brownian motion (above 10 mbar), to the underdamped regime, where the particle's motion is dominated by sustained oscillations at its characteristic frequencies.

2.1.4 Trapping protocol and particle discharging

To perform an experiment with a levitated particle, we need to prepare the particle in a suitable initial state. We do so by following the protocol explained in this section.

1. At ambient conditions, we spray particles inside the chamber using the nebulizer until one particle gets trapped in the laser focus.
2. We start pumping down while monitoring the oscillation frequencies of the particle, until we observe a sudden change in the frequencies (usually around 1×10^{-1} mbar) [42, pp. 89f.]. We believe this change is due to a modification of the structure of the nanoparticle. Indeed, as the pressure in the chamber goes down, fewer and fewer gas molecules are available for the particle to thermalize. The internal temperature of the silica sphere therefore increases due to absorption, possibly enough to cause a phase change of the material. The particle, initially made of porous Stöber silica, transforms into fused silica with a higher density ($\rho_{\text{Stöber}} = 1840(10) \text{ kg/m}^{-3}$, $\rho_{\text{SiO}_2} = 2200 \text{ kg/m}^{-3}$ [54]). We conjecture that residues of the solvent, here isopropanol, got trapped

2. PARTICLE TRAPPING IN VACUUM

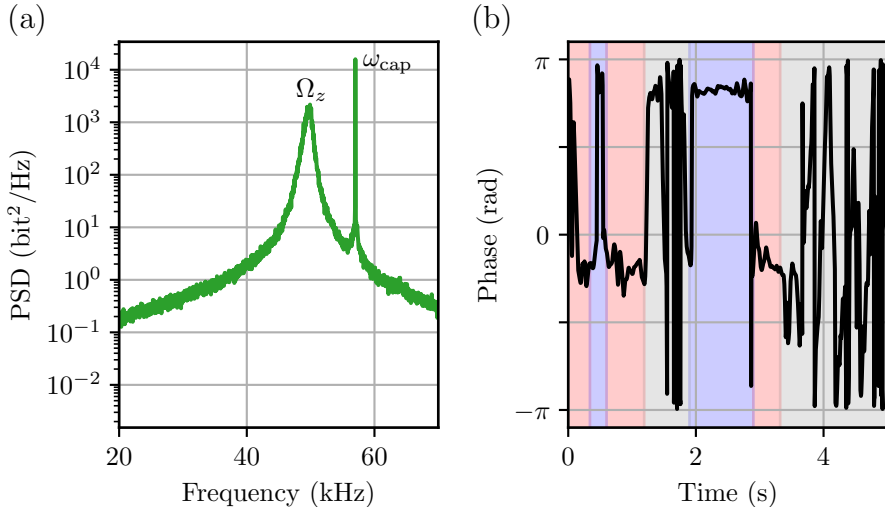


Figure 2.3: (a) Power spectral density of the z -peak under electric driving. The response of the particle to this drive is the narrow peak at 57 kHz. (b) Phase of the particle's response with respect to the drive over time, when the plasma is activated. The phase is either π (in blue regions) or 0 (in red regions), depending on the sign of the particle charge. In grey areas, the phase is undefined, corresponding to a neutral particle. For this particular measurement, we switch off the plasma after 4 s, to keep the particle in a neutral state.

in the pores of the sphere, and are then released during the glass restructuring. As the oscillation frequency scales inversely with the density [42, p. 90], we expect a drop in frequency (a few kHz), which is what we observe experimentally. We also note that this abrupt change in phase leads to a change in charge-to-mass ratio of the particle.

3. Once the particle has reached its final structure, we want to assure that it is neutral, to avoid electrostatic interactions with its environment [55]. To measure and to remove the charges

that it carries, we use the technique described in Ref. [56] and illustrated in Fig. 2.1. The grounded objective and the metallic housing of the collection lens form a capacitor. We apply a voltage $V(t) = V_0 \cos(\omega_{\text{cap}}t)$ to the lens holder ($V_0 = 10V$), creating an electric field in the region where the particle levitates. The particle feels a force $F = Q\mathcal{E}$ where Q is the charge of the particle and $\mathcal{E} = \mathcal{E}_d \cos(\omega_{\text{cap}}t)$. Given our configuration, \mathcal{E}_d is around 1 kV/m. If we choose ω_{cap} close to Ω_z , then the particle is driven by the electric field, and we observe an additional peak in the PSD, as shown in Fig. 2.3 (a), where $\omega_{\text{cap}} = 2\pi \times 57$ kHz and $\Omega_z = 2\pi \times 50$ kHz. We monitor the phase difference between the driving signal and the response peak with a lock-in amplifier. The phase value (in or out of phase) depends on the sign of the charges on the particle (a correspondence can be established using the transfer function of the electronics, but it was not done here, as we are only interested in the neutral state). From the data shown in Fig. 2.3 (a), we can deduce the charge-to-mass ratio of the particle. However, we also need to control this charge-to-mass ratio. To this end, we create a plasma in the chamber (in purple in Fig. 2.1) by applying a high voltage (-1.5 kV) to a wire fixed inside the chamber. The air around this wire is ionized, and positive and negative charges are emitted, whose travel range depends on the pressure. Experimentally, pressures between 1×10^{-1} and 4×10^{-1} mbar turn out to be well suited for controllably modifying the charge of the particle. We rely on these charges colliding with the trapped particle and changing its charge state. As we are continuously monitoring the charge-to-mass ratio, we are able to switch off the plasma as soon as the phase becomes undefined, *i.e.*, once the particle does not respond to the electric drive anymore and its charge is 0 (see Fig. 2.3 (b)). Once the plasma is switched off, the charge state of the particle remains unchanged, as shown in Ref. [56].

4. Finally, we increase the pressure back to 10 mbar to perform the calibration of the particle motion. For this purpose, we record a time trace of a few seconds of the particle position and extract a calibration factor as described in Sec. 2.2.4. Then the particle is ready for any further measurements.

2.2 Trapping theory

2.2.1 Optical forces

An object irradiated with an electromagnetic field is subject to optical forces. If we assume a monochromatic field at wavelength λ and a small spherical object of radius r , so that $2r \ll \lambda$, with no static dipole moment and with an isotropic polarizability, we can use the dipole approximation and express the force on the particle as [57, p. 457]

$$\langle \mathbf{F}_{\text{opt}} \rangle = \frac{\alpha'}{2} \sum_i \text{Re} \{ \mathcal{E}_i^* \nabla \mathcal{E}_i \} + \frac{\alpha''}{2} \sum_i \text{Im} \{ \mathcal{E}_i^* \nabla \mathcal{E}_i \}, \quad (2.1)$$

where $\alpha = \alpha' + i\alpha''$ is the complex-valued polarizability of the particle, and \mathcal{E}_i is the complex field amplitude along the spatial coordinate $i \in \{x, y, z\}$. The first term in Eq. (2.1) corresponds to a conservative force as it can be expressed as the gradient of a potential U ($\mathbf{F}_{\text{grad}} = -\nabla U$) and is called the *gradient force*. It is proportional to the real part of the polarizability α' , and attracts the particle to extrema of the intensity. If $\alpha' < 0$, for example for metallic particles, the gradient force attracts the particle towards regions of low field intensity. On the other hand, if $\alpha' > 0$, for instance for dielectric particles, the gradient force attracts the particle towards region of high field intensity. That's why we can use a focused laser beam to spatially confine a dielectric particle in the focal region, where the intensity is maximal.

For a homogeneous sphere of volume \mathcal{V} and complex relative permittivity $\epsilon(\omega)$, the polarizability α is given by the Clausius-Mossotti relation [58]

$$\alpha(\omega) = 3\epsilon_0\mathcal{V}\frac{\epsilon(\omega) - \epsilon_m(\omega)}{\epsilon(\omega) + 2\epsilon_m(\omega)}, \quad (2.2)$$

where ω is the light frequency, ϵ_0 is the vacuum dielectric constant and $\epsilon_m(\omega)$ is the relative permittivity of the surrounding medium and equals 1 for vacuum.

However, to take into account the radiation reaction [57], *i.e.*, the change of electric field due to the scattering of the dipole, we need to add a correction to the polarizability to obtain an effective polarizability

$$\alpha_{\text{eff}}(\omega) = \frac{\alpha(\omega)}{1 - i\frac{k^3}{6\pi\epsilon_0}\alpha(\omega)} \approx \alpha(\omega) + i\frac{k^3}{6\pi\epsilon_0}\alpha^2(\omega) \quad (2.3)$$

with the wavenumber $k = 2\pi/\lambda$ in air or vacuum¹¹.

The second term in Eq. (2.1) is a non-conservative force, the *scattering force*, also known as radiation pressure. This force pushes the object in the direction of the field propagation. Both scattering and gradient forces compete in the focus of a laser beam, therefore only allowing stable trapping whenever the scattering force cannot push the particle out of the potential formed by the gradient force [43]. If the scattering force is too strong, the particle can still be spatially confined by adding a counteracting force, such as gravity [21] or a counter-propagating beam [20]. We see [from Eq. (2.3)] that the scattering force scales with r^6 whereas the gradient force scales with r^3 , such that for small enough particles, the gradient force always dominates.

¹¹the approximation is valid if we assume $\left(\frac{k^3}{6\pi\epsilon_0}\right)^2\alpha^2(\omega) \ll 1$.

2. PARTICLE TRAPPING IN VACUUM

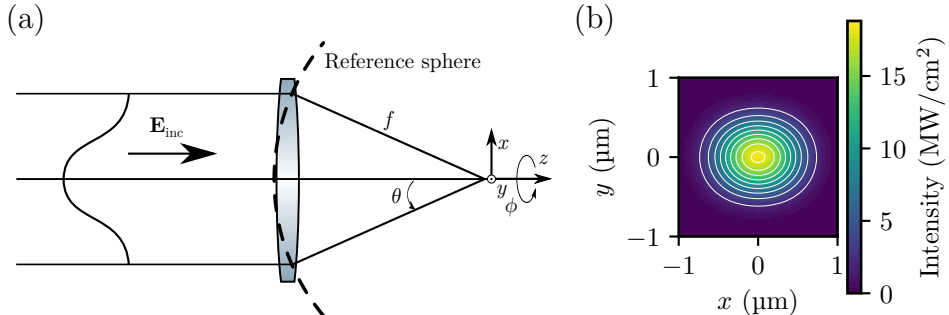


Figure 2.4: (a) Schematic of the incoming Gaussian beam \mathcal{E}_{inc} focused by a lens. The reference sphere of radius f is depicted as a dashed line. The relation between Cartesian and spherical coordinates is also illustrated. (b) Intensity map in the xy plane for $z = 0$ in the focus. We see that the waist of the focus is larger in the x direction than in the y direction, due to the polarization of the beam along x . The white contour lines are a guide for the eye.

We have seen that focusing a laser beam allows us to create an optical trap for dielectric particles. Now we want to have a look at the electric field distribution in the focal region where the particle is confined. We assume here that a Gaussian beam (in the paraxial approximation) polarised along x enters the objective. Following the theory described in Ref [57], we write this field as $\mathcal{E}_{\text{inc}} = \mathcal{E}_{\text{inc}} \mathbf{n}_x$. We only consider the transverse electric (0,0) mode and thus write the field on the reference sphere before the objective in spherical coordinates (sketched in Fig. 2.4(a), adapted from Ref [57]) as

$$\mathcal{E}_{\text{inc}} = \mathcal{E}_0 e^{-f^2 \sin^2(\theta)/w_0^2}, \quad (2.4)$$

where \mathcal{E}_0 is the field amplitude, f is the focal length of the objective and w_0 is the waist of the beam. $|\mathcal{E}_0|$ is given by the total power P of the incoming beam as $|\mathcal{E}_0| = \sqrt{4P/(c\epsilon_0\pi w_0^2)}$ where c is the speed of light. The field directly after the objective on the reference sphere can

be written as

$$\boldsymbol{\mathcal{E}}_\infty = \boldsymbol{\mathcal{E}}_{\text{inc}} \left(\frac{k_x}{k}, \frac{k_y}{k} \right) \begin{bmatrix} k_y^2 + k_x^2 k_z / k \\ -k_x k_y + k_x k_y k_z / k \\ 0 - (k_x^2 + k_y^2) k_x / k \end{bmatrix} \frac{\sqrt{k_z/k}}{k_x^2 + k_y^2}, \quad (2.5)$$

where we have used $k_x = k \sin(\theta) \cos(\phi)$, $k_y = k \sin(\theta) \sin(\phi)$ and $k_z = k \cos(\theta)$. We are interested in the field in the focal region, where we use the fact that the angular spectrum is proportional to the far-field $\boldsymbol{\mathcal{E}}_\infty$ [57, p. 55]. Then, propagating the field from the reference sphere into the focus and transforming back to real space, we find the focal field

$$\boldsymbol{\mathcal{E}}_f(x, y, z) = -\frac{if e^{-ikf}}{2\pi} \iint_{k_x, k_y} \boldsymbol{\mathcal{E}}_\infty \left(\frac{k_x}{k}, \frac{k_y}{k} \right) \frac{1}{k_z} e^{i(k_x x + k_y y + k_z z)} dk_x dk_y. \quad (2.6)$$

This field can be numerically calculated (contrary to the Gaussian beam approximation, where the focused field can be analytically solved) and an intensity map in the xy plane in the focus ($z = 0$) is shown in Fig. 2.4(b). We note that the intensity distribution is not circularly symmetric in this plane, the focus being tighter along the y axis, which is perpendicular to the polarization axis. We can use $\boldsymbol{\mathcal{E}}_f$ as the electromagnetic field in Eq. (2.1) to calculate the forces applied to the trapped nanoparticle in the focus of the laser beam. For the gradient force, we calculate the optical potential at the particle position \mathbf{q} using

$$U(\mathbf{q}) = \frac{-\alpha'_{\text{eff}} I(\mathbf{q})}{2 c \epsilon_0}, \quad (2.7)$$

where $I(\mathbf{q}) = \frac{c \epsilon_0}{2} |\boldsymbol{\mathcal{E}}(\mathbf{q})|^2$ is the field intensity and α'_{eff} is the real part of the effective polarizability [Eq. (2.3)]. We plot in Fig. 2.5(a) the calculated optical potential in the xz plane corresponding to the intensity

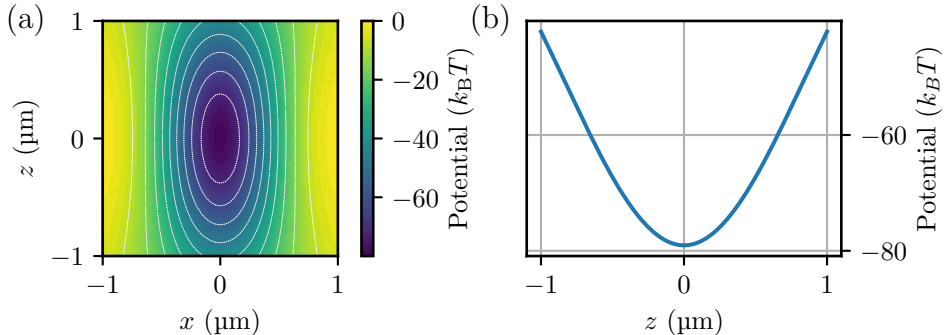


Figure 2.5: (a) Calculated optical potential in the xz plane of a strongly focused beam. The white contour lines are a guide for the eye. (b) Calculated optical potential profile along the optical axis z .

distribution shown in Fig. 2.4(b). Figure 2.5(b) shows a potential profile along the optical axis z of the same potential. Expanding Eq. (2.7) to second order shows a quadratic spatial dependence of the optical potential [42, p. 11]. An expansion to fourth order reveals quartic terms, that are only relevant for large oscillation amplitudes, when the particle explores the non-linearities of the optical potential. The odd expansion orders cancel out due to symmetry reasons.

2.2.2 Particle dynamics

After investigating the optical forces existing in the focus, we can study the motion of a trapped particle subject to those forces. As previously mentioned, the potential is to first approximation quadratic and, for small oscillation amplitude, we can work under the harmonic oscillator approximation and treat the three-dimensional harmonic oscillator as three decoupled 1D harmonic oscillators with oscillation frequencies

defined as

$$\Omega_q = \sqrt{\frac{k_q}{m}}, \quad (2.8)$$

where $q \in \{x, y, z\}$, Ω_q is the angular oscillation frequency of the particle along the direction q , m is the nominal particle mass (2.01 fg), and the coefficient k_q is the trap stiffness along the direction q . These trap stiffnesses cannot be calculated analytically if we consider the strongly focused field described in Eq. (2.6). However, if we work under the paraxial approximation, and assume the focused field to be a Gaussian field, we obtain the expressions derived in Ref. [42, p. 12]. It is important to notice that k_q is inversely proportional to the waist of the beam along direction i . In particular, as we have seen in Fig. 2.4(b), $k_y > k_x$ leads to $\Omega_y > \Omega_x$.

Besides optical forces, the particle also interacts with the surrounding gas molecules, leading to damping and driving forces. The equation of motion of the particle reads

$$\ddot{q}(t) + \gamma\dot{q}(t) + \Omega_q^2 q(t) = \frac{1}{m} \left[F_{\text{fluct}}^{(q)}(t) + F_{\text{scat}}^{(q)}(t) \right], \quad (2.9)$$

where γ is the damping rate, $F_{\text{scat}}^{(q)}(t)$ is the scattering force along the axis q and $F_{\text{fluct}}^{(q)}(t)$ is the total fluctuating force along q , related to the damping rate γ through the fluctuation-dissipation theorem, which states [27, 59, 60]

$$\langle F_{\text{fluct}}(t) F_{\text{fluct}}(t + \tau) \rangle = 2m\gamma k_B T \delta(\tau), \quad (2.10)$$

where k_B is the Boltzmann constant, T is the bath temperature and δ is the Dirac delta distribution. This autocorrelation of F_{fluct} is zero for $\tau \neq 0$, which means that this fluctuating force at time t does not depend on its values at previous times.

2. PARTICLE TRAPPING IN VACUUM

A convenient way of characterizing an oscillator is to work in frequency space. Throughout this thesis, we will use the following definition for the Fourier transform of $q(t)$:

$$\tilde{q}(\Omega) = \frac{1}{2\pi} \int q(t) e^{i\Omega t} dt. \quad (2.11)$$

As we are interested only in the frequency of the oscillator and in the amplitude of the motion, but not in the phase, we can work with the quantity $|\tilde{q}(\Omega)|^2$, which is related to the double-sided power spectral density (PSD) by

$$S_{qq}(\Omega) = 2\pi \lim_{\tau \rightarrow \infty} \frac{1}{\tau} |\tilde{q}(\Omega)|^2. \quad (2.12)$$

The Wiener-Khinchin theorem [61, 62] states

$$S_{qq}(\Omega) = \frac{1}{2\pi} \int_{-\infty}^{+\infty} \langle q(t)q(t+\tau) \rangle e^{i\Omega\tau} d\tau, \quad (2.13)$$

which is the Fourier transform of the autocorrelation function defined as

$$\langle q(t)q(t+\tau) \rangle = \lim_{\tau \rightarrow \infty} \frac{1}{\tau} \int_{-\tau/2}^{\tau/2} q(t)q(t+\tau) dt. \quad (2.14)$$

Now, if we take the inverse Fourier transform of Eq. (2.13), we find that

$$\int_{-\infty}^{+\infty} S_{qq}(\Omega) d\Omega = \langle q(t)^2 \rangle, \quad (2.15)$$

where $\langle \cdot \rangle$ represents a time average. Accordingly, the variance of the particle position $\langle q(t)^2 \rangle$ is the integrated area below the power spectral density. We also know that the potential energy of the particle

along one axis can be expressed as $\langle E_{\text{pot}} \rangle = \frac{1}{2}m\Omega_0^2 \langle q(t)^2 \rangle = \frac{1}{2}k_{\text{B}}T$, with Ω_0 the center oscillation frequency, and its kinetic energy as $\langle E_{\text{kin}} \rangle = \frac{1}{2}m \langle \dot{q}(t)^2 \rangle$. We can therefore calculate the total energy of the particle as $\langle E_{\text{tot}} \rangle = \langle E_{\text{kin}} \rangle + \langle E_{\text{pot}} \rangle$. We can also estimate the root-mean-square amplitude of the oscillations at room temperature for a particle of mass $m = 2.01$ fg, using typical frequencies of $\Omega_z = 2\pi \times 50$ kHz, $\Omega_x = 2\pi \times 140$ kHz and $\Omega_y = 2\pi \times 165$ kHz. Doing so, we find $\sqrt{\langle z(t)^2 \rangle} \approx 150$ nm, $\sqrt{\langle x(t)^2 \rangle} \approx 50$ nm and $\sqrt{\langle y(t)^2 \rangle} \approx 44$ nm.

We note that one might be interested in other characteristics of the oscillation, for example the center oscillation frequency Ω_0 or the width of the oscillation peak, which is related to the damping γ . To access these parameters, we transform the equation of motion [Eq. (2.9)] into Fourier space [42, p. 16]. Using Eqs. (2.10, 2.12, 2.13), we find that close to resonance in the underdamped regime ($\Omega \approx \Omega_0$ and $\gamma \ll \Omega_0$), we can approximate the peak in the spectrum with a Lorentzian¹²

$$S_{qq}(\Omega) = \frac{k_{\text{B}}T}{2\pi m\Omega_0^2} \frac{\frac{\gamma}{2}}{(\Omega - \Omega_0)^2 + (\frac{\gamma}{2})^2}. \quad (2.16)$$

with $k_{\text{B}}T/(m\Omega_0^2)$ being the area under the curve.

2.2.3 Detecting the light scattered by the particle

In this section, we study the detection mechanism of the particle in more detail. We consider the different fields that are impinging on the photodetector, in order to understand the effect of the particle motion on the detector signal. However, the goal of this section is not to derive analytical formulae but to get an understanding of what affects the signal that we measure with the photodetectors.

We determine the particle position by collecting the light it scatters. Considering only elastic scattering, the scattered light has the same

¹²the mathematical equality $\int \delta(\tau)e^{i\Omega\tau} d\tau = 1$ is useful here

2. PARTICLE TRAPPING IN VACUUM

wavelength and polarization as the trapping beam. The phase of the scattered field varies depending on the position of the particle within the trap. We therefore use a phase sensitive interferometric detection mechanism to detect the particle position.

The particle is illuminated by the focal field \mathcal{E}_f [see Eq. (2.6)]. Since the particle is much smaller than the wavelength, we can use the dipole approximation. The induced dipole moment of the particle at position \mathbf{q} is therefore [57, p. 235]

$$\mathbf{p} = \alpha \mathcal{E}_f(\mathbf{q}). \quad (2.17)$$

Let's examine the polarization of \mathcal{E}_f , which is determined by \mathcal{E}_∞ according to Eq. (2.6). The expression given in Eq. (2.5) is not convenient to estimate the field component, especially along the optical axis where $k_x = k_y = 0$. An equivalent expression [57, p. 60] reads

$$\mathcal{E}_\infty = \mathcal{E}_{\text{inc}}(\theta, \phi) \frac{1}{2} \begin{bmatrix} (1 + \cos \theta) - (1 - \cos \theta) \cos(2\phi) \\ -(1 - \cos \theta) \sin(2\phi) \\ -2 \cos \phi \sin \theta \end{bmatrix} \sqrt{\cos \theta} \quad (2.18)$$

and provides a more intuitive idea of what happens. On the optical axis ($\theta = 0$), only the x -component of \mathcal{E}_∞ survives, which is the axis along which the incident trapping beam is polarized. Away from the optical axis, y - and z -components can be non-zero. If the particle is displaced by 100 nm from the optical axis, which corresponds to a typical oscillation amplitude (see Sec. 2.2.2), the y - and z -components are at least 20 times smaller than the x -component. Therefore, we will assume from now on that the induced dipole moment is directed along x .

The fields of an electric dipole at an observation point \mathbf{r} are determined by the Green function $\overleftrightarrow{\mathbf{G}}(\mathbf{r}, \mathbf{q})$ [57, p. 235]. As we are collecting the scattered light several mm away from the particle, we can account

only for the far-field component, which is described in free space by

$$\overleftrightarrow{\mathbf{G}}_{\text{FF}}(\mathbf{r}, \mathbf{q}) = \frac{e^{ikR}}{4\pi R} \left[\overleftrightarrow{\mathbf{I}} - \frac{\mathbf{R}\mathbf{R}^T}{R^2} \right] \quad (2.19)$$

with $\mathbf{R} = \mathbf{r} - \mathbf{q}$, $R = |\mathbf{r} - \mathbf{q}|$, and $\overleftrightarrow{\mathbf{I}}$ the identity tensor. Assuming the observation point is far enough from the particle, and remembering that the position information is contained in the phase of the emitted field, we can approximate the emitted field as ¹³

$$\mathcal{E}_{\text{dp}}(\mathbf{r}) \approx \omega^2 \mu_0 \overleftrightarrow{\mathbf{G}}_{\text{FF}}(\mathbf{r}, \mathbf{q}) \mathbf{p} = \frac{\omega^2 \mu_0 |\mathbf{p}|}{4\pi |\mathbf{r}|} \exp \left[i \left(k |\mathbf{r}| - k \frac{\mathbf{r} \cdot \mathbf{q}}{|\mathbf{r}|} \right) \right] \mathbf{n}_x, \quad (2.20)$$

where μ_0 is the vacuum permeability.

This emitted field is collected by a lens with focal length f , which mathematically transforms spherical wavefronts on the reference sphere $\mathbf{r}_{\text{ref}} = (r_x, r_y, r_z^{\text{ref}})^T$ of radius f into plane waves and vice versa. Thus, the collimated field after the collection lens at a position $\mathbf{r}' = (r_x, r_y, r_z - f)^T$ reads [42, p. 40]

$$\begin{aligned} \mathcal{E}'_{\text{dp}}(\mathbf{r}', \mathbf{q}) &= \mathcal{E}_{\text{dp}}(\mathbf{r}_{\text{ref}}) \exp(-ikf) \exp[ik(r_z - f)] \\ &\approx \frac{\omega^2 \mu_0 |\mathbf{p}|}{4\pi f} \exp \left[i \mathbf{k}' \mathbf{r}' - ikz \left(1 - \frac{\rho^2}{2f^2} \right) \right] \mathbf{n}_x, \end{aligned} \quad (2.21)$$

where we used $r_z^{\text{ref}} = \sqrt{f^2 - r_x^2 - r_y^2} \approx f - \rho^2/2f$, $\rho^2 = r_x^2 + r_y^2$ and $\mathbf{k}' = k(-x/f, -y/f, 1)^T$. We see in Eq. (2.21) that a displacement of the particle in the transverse directions x and y modifies the angle of the phase fronts of the emitted field (first term in the exponent) and a displacement along the optical axis z causes a global phase

¹³detailed derivation can be found in Ref. [42, pp. 39f.]. Only the field component along x survives for small observation angles, *i.e.*, in the paraxial approximation.

shift (second term in the exponent). As we want to detect a phase change, we need to implement an interferometric detection scheme. It is most straight forward to use the interference naturally occurring between the forward scattered light from the particle and the trapping laser propagating beyond the particle. This configuration is commonly called “common-path interferometry”. If we would like to use the backward scattered light from the particle, we would need to interfere it with an external reference field. Intrinsically, such a measurement configuration is more sensitive to drifts as the path lengths of both beams can drift independently, and drift-triggered phase difference adds to the phase difference due to the particle motion, reducing the quality of the detection. A way to circumvent these drifts is to use a heterodyne interferometric technique, where the reference beam, usually called “local oscillator”, is frequency shifted compared to the measurement beam [44, p. 28]. In this thesis, the particle motion was only detected with the forward scattering scheme.

The signal that hits the detector is an interference signal, namely

$$\begin{aligned} I(\mathbf{r}', \mathbf{q}) &= \frac{c\epsilon_0}{2} \left| \mathcal{E}'_{\text{dp}}(\mathbf{r}', \mathbf{q}) + \mathcal{E}'_{\text{trap}}(\mathbf{r}') \right|^2 \\ &= \frac{c\epsilon_0}{2} \left| \mathcal{E}'_{\text{trap}} \right|^2 + c\epsilon_0 \text{Re}[\mathcal{E}'_{\text{trap}} \mathcal{E}'_{\text{dp}}^*] + \frac{c\epsilon_0}{2} \left| \mathcal{E}'_{\text{dp}} \right|^2, \end{aligned} \quad (2.22)$$

where $\mathcal{E}'_{\text{trap}}(\mathbf{r}')$ is the collimated trapping beam (that didn't interact with the particle) after the collection lens. The last term is much weaker than the first and the second terms, so it can be neglected. The first term does not depend on the particle position. Accordingly, all the information sits in the middle interference term. To calculate $\mathcal{E}'_{\text{trap}}(\mathbf{r}')$, we apply similarly the transfer function of the lens on the field \mathcal{E}_f . To calculate $\mathcal{E}'_{\text{dp}}(\mathbf{r}', \mathbf{q})$ as a function of \mathcal{E}_f , we use the relations (2.17) and (2.21). We do not provide here further analytical formulae for $\mathcal{E}'_{\text{trap}}(\mathbf{r}')$ and $\mathcal{E}'_{\text{dp}}(\mathbf{r}', \mathbf{q})$ as the focal field distribution \mathcal{E}_f cannot be expressed in a brief analytical form but remains a double integral.

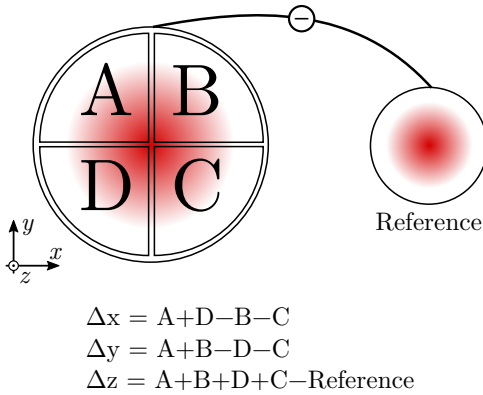


Figure 2.6: Working principles of the quadrant photodetector (QPD) and the balanced detection.

This interference signal is sent onto a quadrant photo detector (QPD) developed and built within the Photonics group at ETH Zurich [42, pp. 46ff.]. The principle is to use a balanced detection scheme to eliminate the first term of Eq. (2.22). To detect the longitudinal motion of the particle, we integrate the entire beam on the photodiode and shine a reference beam of equivalent power, picked up before the trap, on the reference photodiode. After subtracting these two signals, $|\mathcal{E}'_{\text{trap}}|^2$ cancels out, as does the classical intensity noise in the trapping laser, which is common to the reference and the particle signal. For the transverse motion detection, the integrated power on the upper half of the detector is subtracted from the integrated power on the lower half (for y motion), as illustrated in Fig. 2.6. For the x motion, we subtract the right half to the left half of the detector. As a result, for small oscillation amplitudes, the detector signals are proportional to the particle position in the optical trap [42, p. 44]. The advantage of using a QPD over a D-shaped mirrors scheme (see Ref. [43]) is an easier implementation and more stable alignment but also a theoretically higher signal to noise ratio as the power does not need to be split for

detecting the particle motion along three axes.

2.2.4 Calibration of the particle motion

The displacement of the trapped particle is recorded as a voltage generated by the photodetector. To convert this signal into a displacement, we need a conversion factor, that we call the *calibration factor*, in units of Volt/nm or bit/nm.

If the oscillator can be approximated as harmonic, we can calculate the calibration factor c_{calib} using the equipartition theorem [49], which states that the mean of the potential energy for each oscillation mode of a harmonic oscillator in thermal equilibrium is

$$\langle E_{\text{pot}} \rangle = \frac{1}{2} m \Omega_0^2 \langle q^2 \rangle = \frac{1}{2} m \Omega_0^2 \frac{\langle V^2 \rangle}{c_{\text{calib}}^2} = \frac{1}{2} k_B T_{\text{bath}}, \quad (2.23)$$

with T_{bath} the bath temperature, q the position displacement of the particle and V the measured voltage. To calculate the variance of the signal $\langle V^2 \rangle$, we integrate the PSD S_{VV} over the frequencies [according to Eq.(2.15)], *i.e.*, we calculate the area under the curve. The boundaries chosen for the integration of the PSD are crucial here. A wrong choice can lead to underestimation of the energy or attribution of energy to the wrong mode, especially in case of optical cross-talk, as observed in Fig. 2.2. To circumvent this issue, we fit the PSD with Lorentzian peaks [see Eq.(2.16)] and integrate the fit over all frequencies, as illustrated in Fig. 2.7. We then calculate

$$c_{\text{calib}}^2 = \frac{m \Omega_0^2 \langle V^2 \rangle}{k_B T_{\text{bath}}} \quad (2.24)$$

for each mode, assuming that the particle is in thermal equilibrium with the surrounding gas at room temperature, *i.e.*, $T_{\text{bath}} = 300$ K.

Unfortunately, this calibration method has two limitations [42, 49]. First, the calibration factor may change over time (due to drifts of the

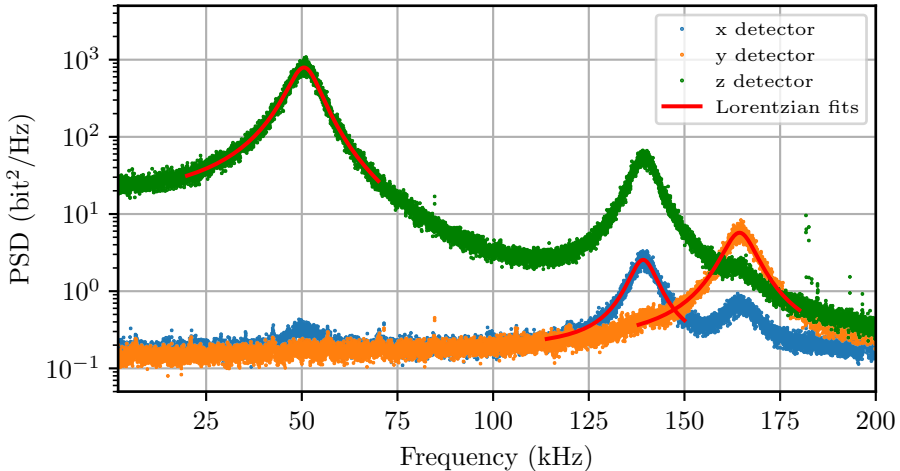


Figure 2.7: Power spectral densities of the x -, y - and z -detectors recorded at 10 mbar. The Lorentzian fits are calculated using Eq.(2.16). The calibration factor for each mode is calculated by integrating the area under the fit for the corresponding mode.

optics inducing misalignment), especially if we perform experiments at low pressures, that require some time to pump down. A solution would be to perform this calibration procedure directly at low pressures. However, in the low pressure regime, we cannot assume a bath temperature of 300 K anymore. Indeed, the energy transfer between the particle and gas molecules, due to convection, is decreased because of the reduced number of gas molecules. Therefore, the laser absorption leads to an increase of the particle internal temperature, resulting in an unknown increased effective bath temperature [63] ($T_{\text{eff.bath}} > 300 \text{ K}$). A method using the particle response to a driving electrostatic field can provide a solution for a calibration method resistant to variations with time [49]. It is however unusable in our case as it requires the particle to carry

2. PARTICLE TRAPPING IN VACUUM

at least one charge, and we want a neutral particle for the experiments close to a surface, to avoid electrostatic interactions with the latter. Moreover, the electrostatic field strength would be modified by the presence of the surface (which acts as a capacitor plate) and therefore would depend on the surface position.

Second, the Lorentzian fitting function used to calculate the variance of the signal assumes a harmonic oscillator. In reality, our oscillator is slightly non-linear. We infer an overestimation of the calibration factor by 5 to 10% [42, pp. 69ff.]. Nevertheless, we will employ the described method to calibrate the time traces of the particle position throughout the thesis, in the absence of a more suitable method.

Chapter 3

Approaching particles to planar surfaces

Optically levitated nanoparticles have enabled scientists to study isolated systems due to their very low coupling with the environment. On one side, many studies have focused on the investigation of the levitated nanoobject itself, its mechanical, optical and electronic properties [27, 28, 48]. On the other side, the levitated nanostructures have been utilized as sensors due to their outstanding sensitivity [63, 64, 65]. Placing a nanoparticle close to another object allows studies of the interactions between the levitated particle and the object. However, any added elements will modify the initial optical trap and therefore the particle dynamics. Hence, we first need to understand the modifications of the trap before studying any direct interaction between the particle and the close object, in our case, a planar surface.

In this chapter, we add to the previously described setup a planar surface, a membrane, to study the behavior of the trapped particle when the membrane is close. A surface placed in the beam path reflects

some of the trapping light. The presence of the membrane creates a standing wave, inducing a trapping optical potential with several local minima, as depicted in Fig. 3.2 [66]. There are two distances that are of importance in this thesis, and whose distinction is crucial. d_{foc} is the distance between the membrane surface and the focal plane of the objective, and d_{part} is the distance between the particle and the membrane surface. Especially for short focus-to-surface distances, the particle will not reside in the focal plane, therefore d_{foc} and d_{part} will be different. In this entire chapter, the experiments are performed with a 500 nm-thick silicon nitride membrane. In Chap. 5, membranes with different thicknesses will be used, because the reflection coefficient, and therefore the trapping potential, highly depend on the membrane thickness.

3.1 Experimental realization

3.1.1 Addition of the membrane

Adding a surface to an optical trap brings modifications mainly inside the vacuum chamber. The new experimental configuration is illustrated in Fig. 3.1. The silicon nitride (SiN) membrane¹ is placed in the beam path between the particle and the collection lens. It is fixed to a metal holder and mounted onto a piezo-electric stage² to enable 3D positioning, with a precision of 1 nm. The piezoelectric stage has position sensors, so that it can operate in closed loop and provides its absolute position. The membrane holder as well as the positioners are electrically grounded. The membrane is semi-transparent for a wavelength of 1064 nm, which allow us to still detect the particle motion in forward direction. An additional photodetector (PD1) and a quarter-

¹Norcada NX series

²Smaract SLC 1720

3.1. Experimental realization

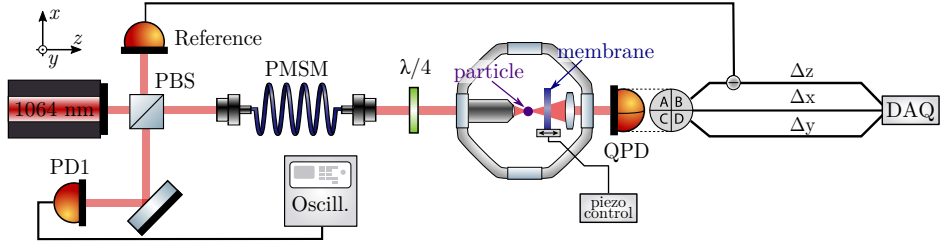


Figure 3.1: Modifications of the experimental setup to add a surface close to the trapped particle. The silicon nitride (SiN) membrane is fixed on a piezoelectric stage, to enable 3D motion. These piezoelectric elements are independently controlled with a controller box, operated either manually or through a computer, with a precision of 1 nm. A quarter-wave plate ($\lambda/4$) and a photodetector (PD1) allow for the detection of back scattered light for calibration purposes. The signal from PD1 is recorded with an oscilloscope.

wave plate are used to calibrate the position of the membrane relative to the trap, as explained in the following section. We read the voltage from PD1 with an oscilloscope³. In this schematic, the charge control elements, described in the previous chapter, have been omitted for clarity, but they are still present in this configuration and allow to control the particle charge even with the surface inside the vacuum chamber. Working with a neutral particle is crucial to avoid undesired electrostatic interactions with the membrane [55].

3.1.2 Determination of the membrane position relative to the focus

We first need to calibrate the z position of the membrane relative to the vacuum chamber. The reference point chosen for that purpose is the focus of the trapping objective. Accordingly, we will calibrate the stage

³Lecroy Waverunner 610Zi

3. APPROACHING PARTICLES TO PLANAR SURFACES

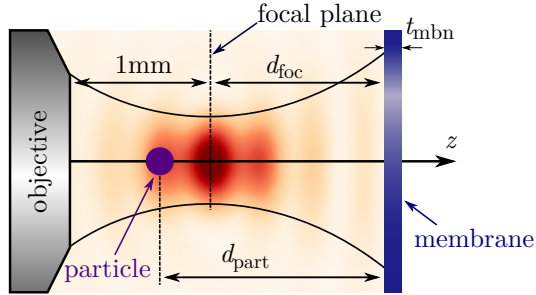


Figure 3.2: Relevant geometrical parameters (not to scale) in the configuration with the membrane of thickness t_{mbn} . d_{foc} is the distance between the focal plane of the objective and the front surface of the SiN membrane. The optical potential illustrated in red, resulting from the interference between the trapping beam and the reflections from the membrane, determines the distance d_{part} between the particle and the membrane surface.

position relative to the focus position, *i.e.*, we want the stage position to be zero when the membrane is in the focal plane. To this end, we place the quarter-wave plate as described in Fig. 3.1 before the objective in the optical path, such that the polarization of the back-reflected light is turned by 90° . This enables to separate the forward propagating trapping beam from the reflected beam with a polarizing beam splitter (PBS). The PMSM acts as a spatial filter, so that the maximum power collected by the photodetector PD1 corresponds to the surface being in the focus of the trapping laser. This means we are effectively imaging the focal plane of the objective on the photodetector. We then move the membrane along the z direction through the focus and we record the light scattered back from the surface on the photodetector PD1. Fig. 3.3 shows as blue points the voltage recorded on PD1, as the stage position is swept through the focus. The envelope of the curve has a bell-like shape, originating from the spatial filter, *i.e.*, the fiber. The modulation on top of the envelope comes from the interference between the field reflected from the membrane and the back-reflected light

from other optic surfaces in the beam path. To determine the precise position where the membrane is in the focus, we fit the measured intensity profile with a simple model explained in the following.

We only consider the fields along the optical axis that are propagating backwards and that reach the detector PD1. We assume a strongly focused beam [see Eq. (2.6)] that has been reflected from the membrane. This reflected field interferes with a back-propagating plane wave, originating from reflections from the surfaces of optics in the laser path. We model this field as $\mathcal{E}_{\text{pl}}e^{i\xi}$ where \mathcal{E}_{pl} represents the amplitude and ξ is the phase. We fit the blue data points in Fig. 3.3 with such a model. In the fitting function, we allow for an offset and a scaling factor as free parameters, together with \mathcal{E}_{pl} and ξ . Let us note here that we have to use Eq.(2.6) with the argument $2(z - z_{\text{foc}})$ instead of just z , where z_{foc} represents the position of the focus along the z axis⁴, to consider the focused beam that has been reflected from the membrane. Figure 3.3 shows in orange the resulting fit of the intensity profile. We extract the focus position in the coordinate system of the stage $z_{\text{foc}} = 125.56 \mu\text{m}$. We remark that the intensity of the peaks do not perfectly agree with the measurement, because of the assumptions we have made for the model. Indeed, we calculated the intensity in the geometrical focus and not on the detector PD1, neglecting the intensity that is not on the optical axis, but that still contributes to the detector signal. However, this approximation does not influence the determination of the focus position, as the latter only relies on the phase information and the fact that the intensity is maximum when the membrane sits in the focal plane. Repeating the measurement several times, we average the extracted focus positions and obtain $z_{\text{foc}} = (125.54 \pm 0.03)\mu\text{m}$. We can therefore set this value as the zero for the stage readout, as $d_{\text{foc}} = 0$. From now on, the stage readout

⁴ z_{foc} is the position of the focal plane in the coordinates system of the piezo stage.

3. APPROACHING PARTICLES TO PLANAR SURFACES

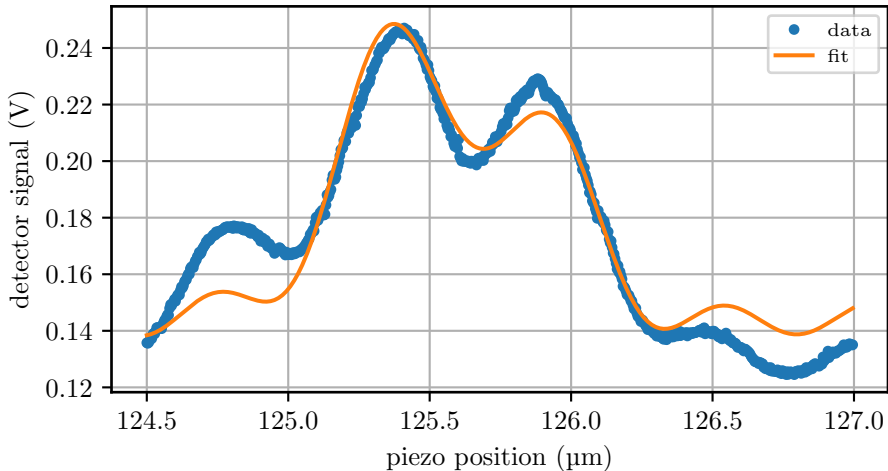


Figure 3.3: Voltage recorded on the photodetector PD1 as the membrane position is swept across the focus towards the objective (blue). We fit (orange) the measurement according to a simple model taking into account back reflections from optics surfaces in the beam path as a plane wave. We extract from the fit the parameter $z_{\text{foc}} = 125.56 \mu\text{m}$, which is the position of the focus along the z axis in the coordinate system of the stage.

gives directly the distance d_{foc} .

3.2 Potential mapping at large distances

Experimentally, the membrane is introduced in the beam path at large distances from the particle ($\approx 1 \text{ mm}$) and is slowly moved towards the particle. In this section, we want to study the particle behavior during the membrane approach for distances $d_{\text{foc}} > 20 \mu\text{m}$. We will first present the experimental results and then propose a theoretical model to qualitatively explain the experimental observations.

3.2.1 Measurement of the trapping potential at large distances

In order to study the optical potential in the presence of the membrane, we measure the particle behavior as the distance between the membrane and the particle is reduced. To this end, we trap a silica nanoparticle in the way described in the previous chapter, when the membrane is retracted, *i.e.*, not in the laser path⁵. Moreover, to avoid contamination of the membrane during the spraying of the particles, we manually cover the membrane. We remove this cover once a particle has been trapped. We perform the first pump down to trigger the structural change observed around 1×10^{-1} mbar (see Sec. 2.1.4) and we discharge the particle. Then we position the membrane in the laser path⁶ at a pressure of 1.5 mbar, approximately 1 mm away from the focus ($d_{\text{foc}} = 1$ mm). The focus-to-surface distance d_{foc} has been calibrated prior to the loading of the particle into the trap with the method explained in Sec. 3.1.2. We then move the membrane along the optical axis, towards the particle, at a constant speed of 20 nm/s. The approach speed is not a critical parameter. The only requirement is that the approach stays slow enough for the particle to thermalize at every position. As the membrane approaches the particle, the surface's influence on the trapping field increases. We observe a modulation of the oscillation frequency Ω_z . The modulation amplitude increases during the approach. We plot in Fig. 3.4(a) the PSD calculated from 30 s-long time traces of the particle position (recorded at 1.5 mbar) as a function of the distance d_{foc} around 40 μm . These time traces are calibrated using the method explained in Sec. 2.2.4. The salient feature in each spectrum represents the oscillation frequency Ω_z , which varies between 20 and 85 kHz with a periodicity of ≈ 540 nm.

⁵This is performed by maximally displacing the piezo-electric stage along the x direction.

⁶using the piezo-actuator motion in the transverse directions

3. APPROACHING PARTICLES TO PLANAR SURFACES

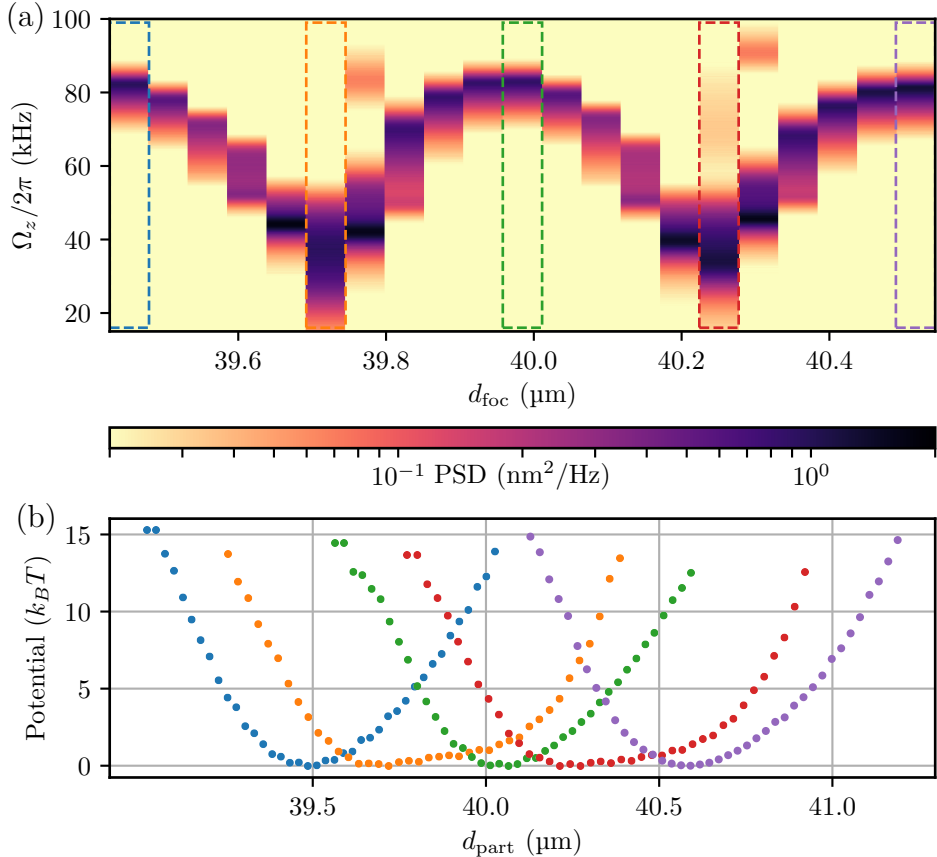


Figure 3.4: (a) Power spectral densities calculated from measured 30 s-long time traces of the particle position along z , recorded at 1.5 mbar, as a function of the distance focus-to-surface d_{foc} . The dark feature represents the oscillation frequency peak at Ω_z , which oscillates with a period of $\lambda/2$ between 20 and 85 kHz. (b) Optical potentials reconstructed from the time traces used in (a), assuming a Boltzmann distribution of the particle positions along z . The particle is oscillating around its equilibrium position, which corresponds to d_{foc} since the optical potential minimum is in the focal plane. The color code indicates to which d_{foc} position, *i.e.*, to which time trace, each potential corresponds. We observe a $\lambda/2$ -periodic variation in the shape of the optical potential, corresponding to the $\lambda/2$ periodicity of a standing-wave pattern.

3.2. Potential mapping at large distances

We can intuitively understand the experimentally observed variations of the oscillation frequency while approaching the membrane by considering the intensity distribution created by a laser beam focused near an dielectric interface. The interference of the trapping beam with the back-reflected field from the membrane creates a standing wave, which has an intensity distribution that is $\lambda/2$ -periodic along the optical axis z . We also observe that the width of the peak is larger when the oscillation frequency is low and that the peak shape is not Lorentzian anymore. As the oscillation frequency is related to the trap stiffness, as seen in Eq. (2.8), we conjecture that the variation of Ω_z is due to a change in the optical potential shape. To investigate this further, we can reconstruct the optical potential probed by the particle, for every time trace of the particle position along z used in Fig. 3.4(a). To this end, we histogram the particle positions. We assume a Boltzmann distribution of the positions along z , *i.e.*, $p(z) \propto e^{-U(z)/k_B T}$ [42, 67], where $p(z)$ is the probability to find the particle at position z . $U(z)$ represents the optical potential profile, that we can therefore reconstruct, and that we plot in Fig. 3.4(b) for 5 values of d_{foc} [the colors of the data points correspond to the colored rectangles outlined in Fig. 3.4(a)]. The optical potential is plotted in units of $k_B T$. We observe that the orange and red potentials, taken for d_{foc} values separated by $\lambda/2$, are very similar in shape compared to the three others potentials. Indeed, they appear wider and less quadratic, which fits with the observation of a deviation of the particle behavior from the harmonic oscillator, in the regions of low frequencies [Fig. 3.4(a)]. Similarly, the blue, green and purple potentials, taken for d_{foc} positions again separated by $\lambda/2$, look also alike.

3.2.2 Theoretical model: large distances analysis

Theory of strongly focused field near surfaces

In this section, we describe in more detail the standing-wave pattern created by the interference of the trapping beam with the reflections from the membrane. Similarly to Sec. 2.2.1, we want to investigate the electromagnetic field in the focal region. However, we have now positioned an interface at $z = d_{\text{foc}}$ ($z = 0$ corresponds to the focus position), which reflects the focused field. In a similar way as in Eq. (2.6), we derive for the reflected field [57]

$$\mathcal{E}_r(x, y, z) = -\frac{if e^{-ikf}}{2\pi} \iint_{k_x, k_y} \mathcal{E}_\infty^r \left(\frac{k_x}{k}, \frac{k_y}{k} \right) \frac{1}{k_{z1}} e^{i(k_x x + k_y y - k_{z1} z)} dk_x dk_y \quad (3.1)$$

with

$$\mathcal{E}_\infty^r = -\mathcal{E}_{\text{inc}} \left(\frac{k_x}{k}, \frac{k_y}{k} \right) e^{2ik_{z1} d_{\text{foc}}} \begin{bmatrix} -r^s k_y^2 + r^p k_x^2 k_{z1}/k \\ r^s k_x k_y + r^p k_x k_y k_{z1}/k \\ 0 + r^p (k_x^2 + k_y^2) k_x/k \end{bmatrix} \frac{\sqrt{k_{z1}/k}}{k_x^2 + k_y^2}, \quad (3.2)$$

where we introduce $k_{z1} = 2\pi n_{\text{air}}/\lambda$ with $n_{\text{air}} = 1$ the refractive index of air, and the Fresnel reflection coefficients r^s and r^p , for s- and p-polarized field components respectively [57, p. 22].

Notice that the sign of k_{z1} in $\mathcal{E}_r(x, y, z)$ changed in the exponent compared to Eq. (2.6) because the reflected field is propagating in the opposite direction than the incoming trapping beam. The total field between the objective and the surface is given by $\mathcal{E}_{\text{tot}} = \mathcal{E}_f + \mathcal{E}_r$. We can integrate Eqs. (2.6) and (3.1) numerically for $\phi \in [0, 2\pi]$ and $\theta \in [0, \theta_{\text{max}}]$ where $\theta_{\text{max}} = \arcsin(\text{NA})$.

3.2. Potential mapping at large distances

Whenever we are only interested in the field along the optical axis z , \mathcal{E}_{tot} can be further analytically simplified into⁷

$$\begin{aligned} \mathcal{E}_{\text{tot}}(0, 0, z) = \frac{ikf\mathcal{E}_0 e^{-ikf}}{2} \mathbf{n}_x \int_0^{\theta_{\text{max}}} \mathcal{E}_{\text{inc}} e^{ikz \cos(\theta)} \sin(\theta) \sqrt{\cos(\theta)} \\ \left[\cos(\theta) \{1 - r^{\text{p}}(\theta) e^{-2ik(z-d_{\text{foc}})\cos(\theta)}\} + \right. \\ \left. \{1 + r^{\text{s}}(\theta) e^{-2ik(z-d_{\text{foc}})\cos(\theta)}\} \right] d\theta, \end{aligned} \quad (3.3)$$

where a single integral remains, saving computation time.

So far, we considered a single interface. To take into account the finite thickness of the membrane, which will result in multiple reflections inside the membrane, we just need to replace the reflection Fresnel coefficients r^{s} and r^{p} by [57, p. 319]

$$r_{\text{slab}}^{(\text{p,s})} = \frac{r_{1,2}^{(\text{p,s})} + r_{2,3}^{(\text{p,s})} e^{2ik_{z2}t_{\text{mbn}}}}{1 + r_{1,2}^{(\text{p,s})} r_{2,3}^{(\text{p,s})} e^{2ik_{z2}t_{\text{mbn}}}}, \quad (3.4)$$

where the subscripts indicate the media forming the interfaces, $k_{z2} = 2\pi n_{\text{SiN}}/\lambda$ with $n_{\text{SiN}} = 2.54$ the refractive index of SiN at a wavelength of 1064 nm, and t_{mbn} is the thickness of the membrane. We then plot in Fig. 3.5(a) the intensity distribution in the xz plane for a 500 nm-thick membrane at a distance of $d_{\text{foc}} = 40 \mu\text{m}$, and in (b) the intensity along the optical axis, *i.e.*, for $x = y = 0$. We notice a slight change in the intensity distribution compared to an optical trap without membrane (dashed orange line), due to the reflections. Yet, this perturbation is very subtle and we still have a global intensity maximum centered around $z = 0$.

⁷based on a private note by L.Novotny

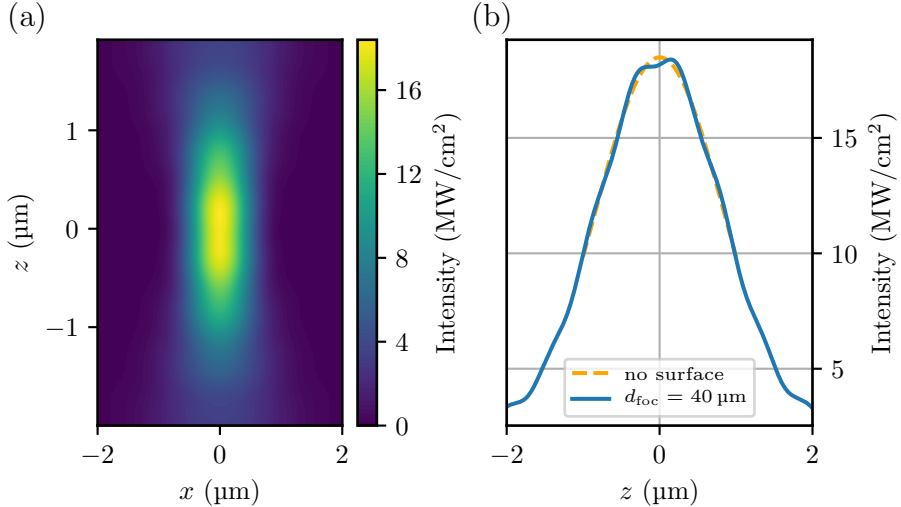


Figure 3.5: (a) Intensity distribution in the xz plane when the membrane is $40 \mu\text{m}$ away from the focus ($d_{\text{foc}} = 40 \mu\text{m}$). (b) Intensity profile along the optical axis z for $x = y = 0$ and $d_{\text{foc}} = 40 \mu\text{m}$ (blue). For comparison, we plot the intensity when there is no surface as a dashed orange line.

Optical potential in the standing wave configuration

Using Eq. (2.7), we calculate the optical potential from the intensity distribution in Fig. 3.5 in units of $k_{\text{B}}T$ and plot a potential map in the xz plane in Fig. 3.6(a). The corresponding potential profile along the optical axis z is shown in Fig. 3.6(b). Again, as for the intensity, we observe a small modification of the optical potential. To help visualizing the influence of the membrane position on the optical potential, we plot the potential for two other membrane positions $d_{\text{foc}} = 40.26 \mu\text{m}$ and $d_{\text{foc}} = 40.53 \mu\text{m}$ in Fig. 3.6(c) and (d), respectively. We observe firstly that the little feature at the bottom of the potential moves as the membrane approaches. Secondly, we notice that after the membrane has been displaced by 532 nm , the potential profile repeats itself. The

periodicity of 532 nm matches the $\lambda/2$ periodicity expected from a standing-wave pattern when using $\lambda = 1064$ nm and matches also the periodicity of the frequency variations observed experimentally. It therefore confirms that the potential shape modification is the origin of the variations of Ω_z . Importantly, the optical potential is henceforth not quadratic anymore and we cannot use the harmonic oscillator approximation to analytically calculate the oscillation frequency of the particle, as mentioned in Sec. 2.2.2. Therefore, we will implement a dynamic simulation of the particle motion in an arbitrarily shaped optical potential.

Simulation of the particle motion in a potential landscape

In order to investigate the particle behavior in optical potentials like the ones described in the previous section (Fig. 3.6), we implement a simulation of the particle oscillating in such a potential⁸. This simulation is performed using the Gaussian beam approximation, and not the strongly focused beam model, to reduce the computation time. Indeed, whereas the Gaussian approximation can be expressed as an analytical formula, the focused beam model requires solving numerical integrals (as mentioned in Sec. 2.2.1), which is computationally significantly more expensive.

In the simulation, we first calculate the optical field from the focused laser beam using the Gaussian beam approximation and then add the reflected Gaussian beam. We obtain the values for the optical field of the standing wave at every point in space. We then calculate the optical forces (gradient force and scattering force) and the random fluctuating force that acts on the particle, as described by the equation of motion in Eq. (2.9). We do not provide all computational details [42, pp. 153ff.],

⁸The initial code is described in the appendix A of Ref. [42, pp. 153ff.] and has been modified to take into account the standing wave created by the reflections from the membrane.

3. APPROACHING PARTICLES TO PLANAR SURFACES

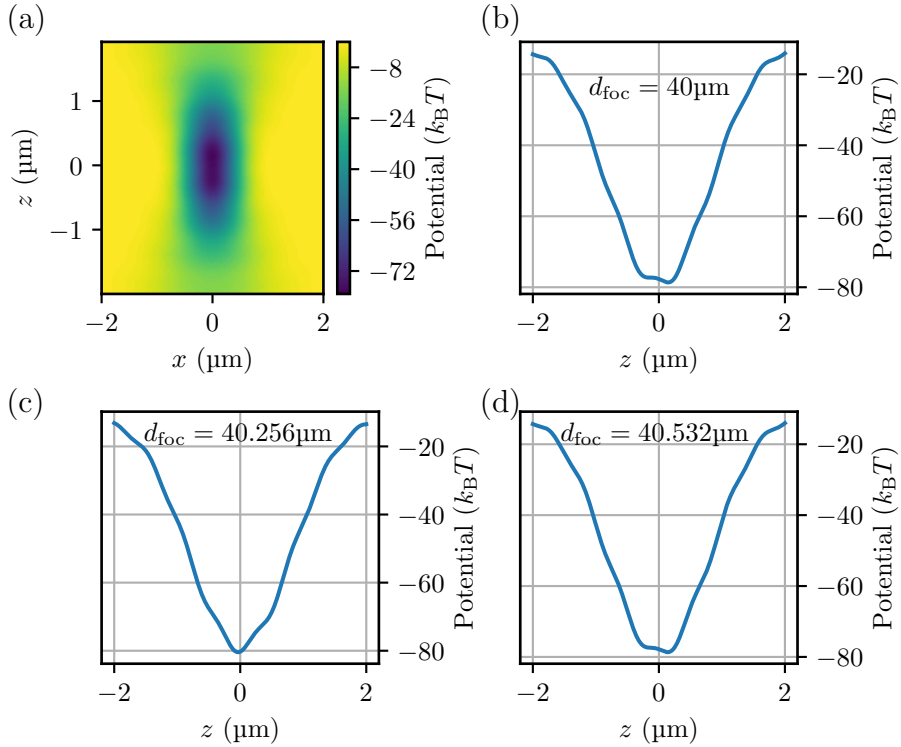


Figure 3.6: (a) Optical potential map in the xz plane when the membrane is $40 \mu\text{m}$ away from the focus ($d_{\text{foc}} = 40 \mu\text{m}$). (b,c,d) Optical potential profile along the optical axis z for $x = y = 0$ and for $d_{\text{foc}} = 40 \mu\text{m}$, $40.266 \mu\text{m}$ and $40.532 \mu\text{m}$ respectively. We observe a periodicity of $\lambda/2 = 532 \text{ nm}$ of the potential shape as a function of distance focus-to-surface d_{foc} .

3.2. Potential mapping at large distances

but we just remind that this simulation solves an initial value problem formulated by $\dot{\mathbf{w}}(t) = \mathbf{f}(t, \mathbf{w}(t))$, where $\mathbf{w}(t) = (q_x, q_y, q_z, \dot{q}_x, \dot{q}_y, \dot{q}_z)$. To initiate the simulation, we provide initial potential and kinetic energies to the particle, and fix the focus-to-surface distance d_{foc} . We set a time step for solving the initial value problem (20 ns), and the length of the time trace (50 ms) to be calculated for each distance d_{foc} . At the end of each time-trace simulation, the final values for the positions and the velocities of the particle are stored and used as initial values for the next time-trace calculation. This way, we realize a dynamic simulation which resembles closely the experiment where the membrane is constantly moved. Typical computation time is around 1.5 hour for a time trace of 50 ms. Laser noise is not included in the simulation.

We show in Fig. 3.7 the result of a simulation performed with the parameters summarized in Table 3.1. We calculate the PSD for each 50-ms time trace and plot the spectra as a function of the distance d_{foc} . We are interested in the evolution of the oscillation frequency Ω_z over time when the membrane is approached. We observe a periodic variation of Ω_z with a period of $\lambda/2$, which agrees with both the standing-wave periodicity and the experimental observations (Fig. 3.4). The Ω_z peak is wider (and not Lorentzian-shaped) for low oscillation frequencies whereas the peak becomes narrower for high Ω_z . This observation goes along with the anharmonicity of the optical potential found in Fig. 3.6(b,d). We note a deviation for the absolute values of Ω_z compared to the Fig. 3.4 (a), that we attribute to the Gaussian beam approximation and to a possible slight mismatch between the power in the simulation compared to the experimental value. However, the striking qualitative agreement between the model and the experiment leads us to consider that the Gaussian beam approximation is a good model for the optical field when the surface is a few tens of Rayleigh lengths away from the focus.

3. APPROACHING PARTICLES TO PLANAR SURFACES

Table 3.1: Parameters used in the simulation of the nanoparticle in the optical trap for large distances of the membrane.

Parameter	Value
Time step	20 ns
Length of the timetrace	50 ms
Power in focus	120 mW
Step size for membrane approach	20 nm
Initial d_{foc}	41 μm
Final d_{foc}	39 μm
Number of time traces	100
Particle diameter	136 nm
COM temperature	300 K
Waist along x [43]	687 nm
Waist along y [43]	542 nm
Rayleigh length [43]	1362 nm
Wavelength	1064 nm
Refractive index of fused silica	1.45
Density of the particle	2200 kg/m^3
Damping rate γ	$2\pi \times 1000$ Hz
Membrane thickness	500 nm
Refractive index of SiN	2.54

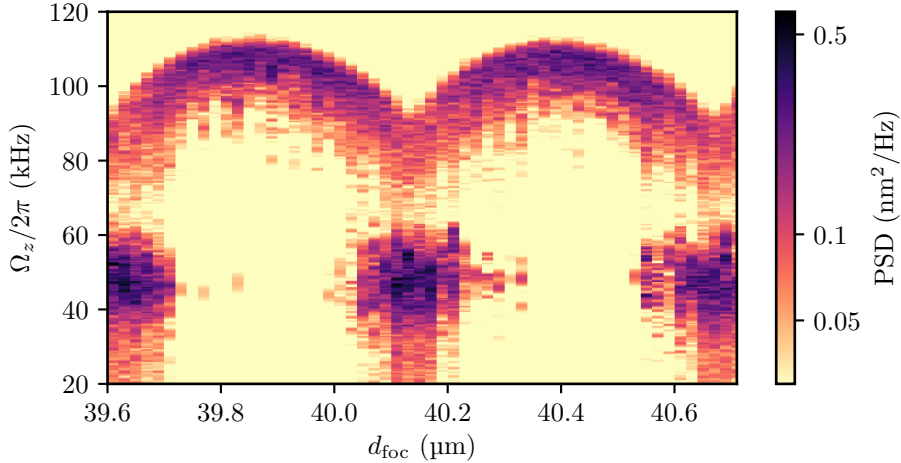


Figure 3.7: Simulation of the particle oscillations along z for a membrane approach from $41\ \mu\text{m}$ to $39\ \mu\text{m}$. We calculate a 50-ms-long time trace for each membrane position and derive the corresponding PSD. We plot these PSDs and display the frequency Ω_z as a function of the focus-to-surface distance d_{foc} . We observe a $\lambda/2$ -periodic variations of Ω_z . We also note that the width of the oscillation peak is larger for low Ω_z and narrower for high Ω_z .

3.3 Potential mapping at short distances

As the membrane is brought even closer to the focal region, its influence on the electromagnetic field distribution grows stronger. We study in this section the optical potential and the behavior of the particle for focus-to-surface distances d_{foc} smaller than 10 micrometers. Similarly to the previous section, we first interrogate our oscillator experimentally, and then try to understand the observation through a theoretical model.

3.3.1 Measurement of the trapping potential at short distances

Frequency behavior during the membrane approach

During the last few micrometers of the approach (speed of the membrane of 20 nm/s), we continuously record time traces of the particle motion of 600 ms with a sampling rate of 667 kHz. For every single time trace, we calculate the PSD and we plot it in Fig. 3.8(a) as a function of the focus-to-surface distance d_{foc} . The salient feature corresponds to the z oscillation at frequency Ω_z . Until d_{foc} is reduced to 3 μm , we continue to observe the periodic oscillatory pattern that we already observed in the case of larger distances d_{foc} . The modulation amplitude of Ω_z is however larger than before, reaching up to $\Omega_z/(2\pi) = 150$ kHz. We show in Fig. 3.8(b) the PSD recorded at $d_{\text{foc}} = 540$ nm and $d_{\text{foc}} = 3.78$ μm respectively [indicated by the dashed lines in Fig. 3.8(a)]. For smaller d_{foc} , we observe a more significant frequency increase, reaching more than 250 kHz for $d_{\text{foc}} = 0$, *i.e.*, when the membrane is exactly in the focus of the laser beam. In Fig. 3.8(a), we note that the frequency Ω_z also undergoes discrete “jumps”, for example at $d_{\text{foc}} \approx 1.9$ μm and at $d_{\text{foc}} \approx 1.1$ μm . We observe also two weaker peaks corresponding to the oscillations of the particle in the transverse directions, with frequencies $\Omega_x \approx 2\pi \times 150$ kHz and $\Omega_y \approx 2\pi \times 175$ kHz. These peaks can be observed on the z detector due to optical cross-talk, as referred to in Sec. 2.1.2. Ω_x and Ω_y decrease significantly for $d_{\text{foc}} < 0.5$ μm , a behavior that we attribute to the widening of the potential along the transverse directions as well 1 is pushed away from the focal plane.

For small distances d_{foc} , the intensity in the focal plane, of the field reflected from the membrane is stronger, enough to create an intensity distribution with several local intensity maxima. As we have seen with Eq. (2.7), the intensity maxima correspond to optical

3.3. Potential mapping at short distances

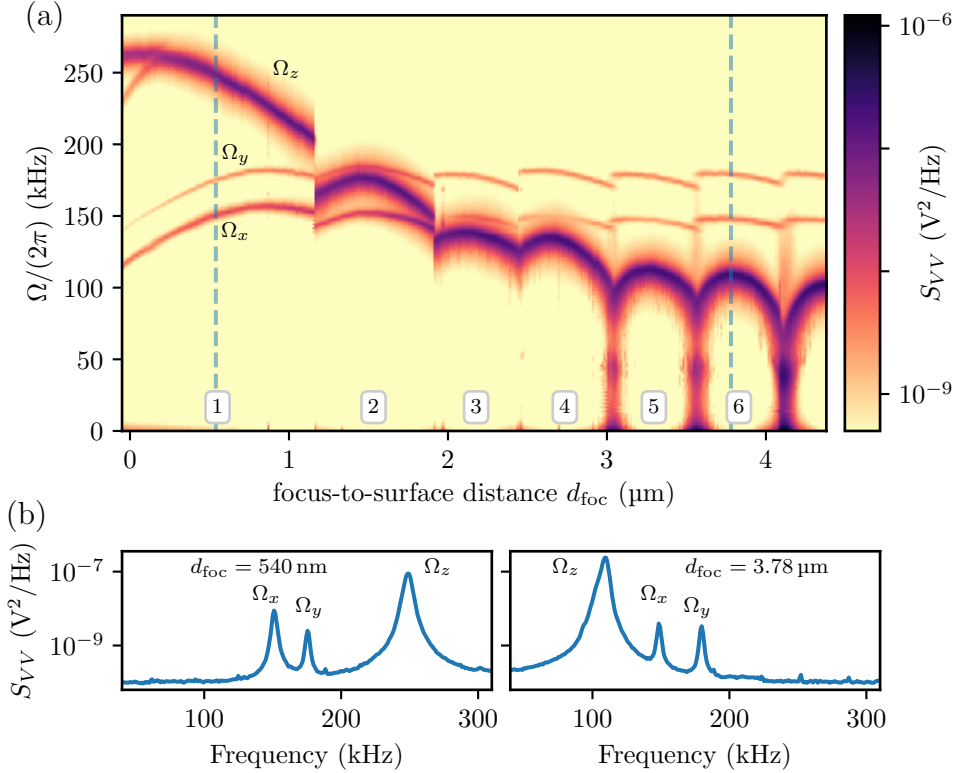


Figure 3.8: (a) Measured power spectral density of the particle motion for decreasing focus-to-surface distances d_{foc} , recorded on the z detector. The strongest peak corresponds to the oscillation mode along z with frequency Ω_z and increases for shorter d_{foc} while being subject to periodic modulations. The two weaker peaks, around 150 kHz and 175 kHz correspond to the oscillations along x and y , respectively. We observe that Ω_z performs discrete jumps for $d_{\text{foc}} < 2 \mu\text{m}$. The boxed numbers indicate in which well the particle is, the wells are numbered starting from 1 for the closest to the membrane. (b) Two examples of PSD, extracted from (a) at the position of the dashed blue lines, for $d_{\text{foc}} = 540 \text{ nm}$ (left spectrum) and $d_{\text{foc}} = 3.78 \mu\text{m}$ (right spectrum). We mainly notice the change in frequency of the z peak.

potential minima, where our dielectric nanoparticle is confined. There are now several stable traps for the particle, and it can hop from one to another as the overall potential landscape is modulated by the approaching membrane, as we will investigate in more detail in the following section. The wells are numbered starting from 1 for the well closest to the membrane, based on the interferometric measurement technique explained in Chap. 4.

To study in more detail what happens when the frequency “jumps”, we plot in Fig. 3.9 a sample of the time trace of the particle position, corresponding to the “jump” around $d_{\text{foc}} \approx 1.9 \mu\text{m}$. We observe that the position of the particle along the z axis undergoes a discrete step of an amplitude of $\approx 350 \text{ nm}$ exactly when the frequency Ω_z jumps, corresponding to the jump from well 3 to well 2. The jump amplitude read on the detector signal is slightly smaller than a separation of $\lambda/2$ between two intensity maxima for a standing wave. We attribute this discrepancy to multiple origins: an error in the calibration of the position axis, the non-linearity of the detector transfer function and the AC filter of the detector [42, p. 44].

$2\Omega_x$ peak due to non-linearities

We witness the appearance in Fig. 3.8(a) of an additional peak in the PSD for $d_{\text{foc}} \approx 0$, around 250 kHz. This peak corresponds to twice the oscillation frequency Ω_x and appears because the particle starts to probe the non-linearities of the optical potential along the x axis⁹. Indeed, we already mentioned that for $d_{\text{foc}} < 0.5 \mu\text{m}$, well 1 does not longer reside in the focal plane. This results in the particle being confined in an asymmetric potential. In this case, the Taylor expansion of the optical potential [see Eq. (2.7)] reveals third order terms, in particular the terms in zx^2 , zy^2 . The derivative of the potential with

⁹and also along y but it is not visible on this measurement

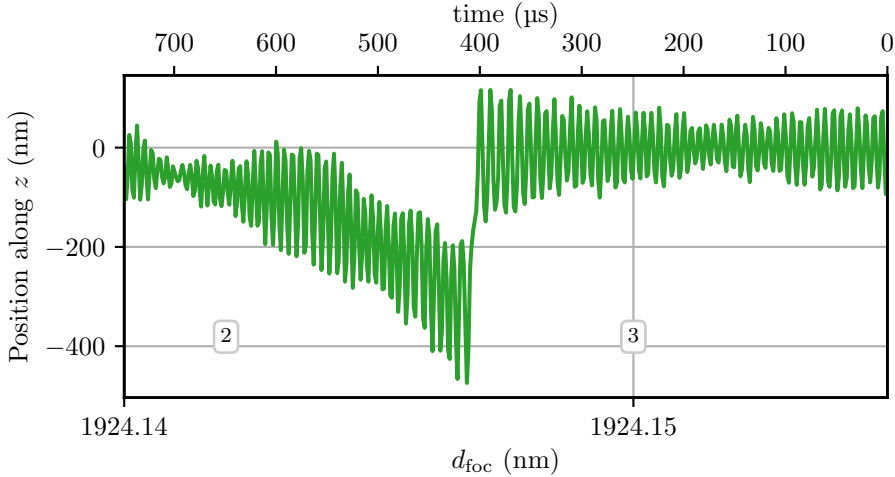


Figure 3.9: Time trace of the particle position along the z axis around $d_{\text{foc}} = 1.924 \mu\text{m}$. The time axis was started at an arbitrary position and just illustrates the time frame of the jumping process. The position along the z axis has been calibrated using the method described in Sec. 2.2.4. We observe the particle jumping from well 3 into well 2 (indicated by the boxed numbers).

respect to z , expressing the force exerted on the particle along z , yields the Ω_z component as usual, but also the components $2\Omega_x$ and $2\Omega_y$, hence the appearance of the peak at $2\Omega_x$ in the PSD.

Anti crossing between modes

For other measurements similar to the one described in Fig. 3.8(a), a slightly different alignment (mostly due to drifts of optics over time) or a different trapping objective leads to slightly different oscillation frequencies, and we can sometimes observe an overlap of Ω_x or Ω_y with Ω_z , for $1.1 \mu\text{m} < d_{\text{foc}} < 1.9 \mu\text{m}$. We show in Fig. 3.10 the example of such a measurement, where we observe an avoided crossing between

3. APPROACHING PARTICLES TO PLANAR SURFACES

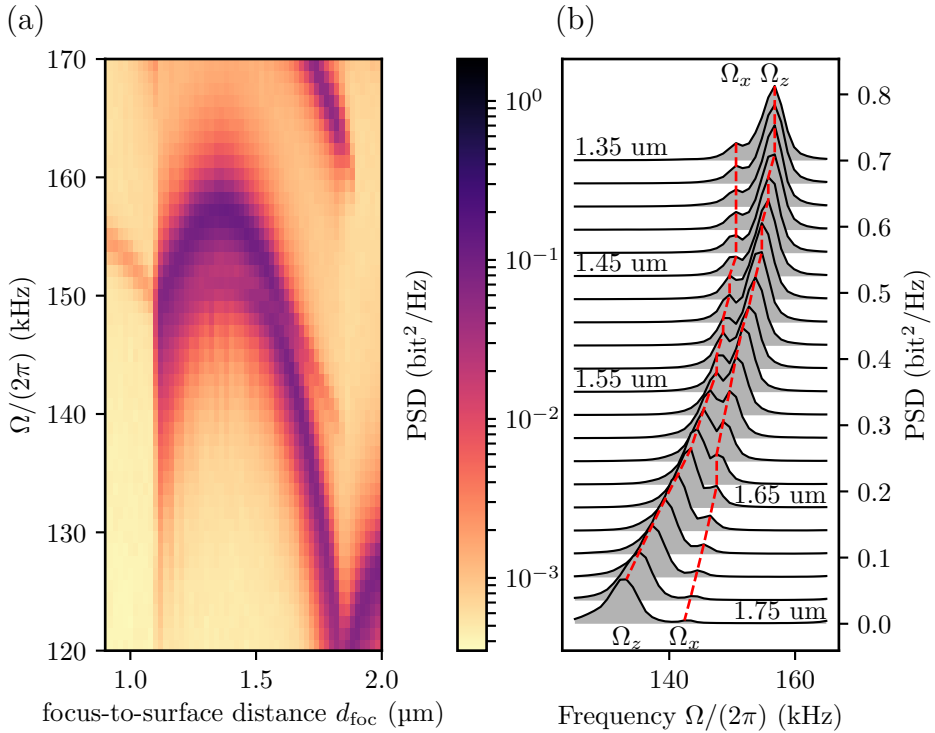


Figure 3.10: (a) Measured power spectral density of the particle motion for decreasing focus-to-surface distances d_{foc} , recorded on the z detector, for a different measurement than in Fig. 3.8. We display the region around $d_{\text{foc}} = 1.5 \mu\text{m}$ to observe the anti crossing between the z - and x -modes. (b) Another way of plotting the PSD as a function of d_{foc} where the anti crossing between Ω_z and Ω_x is more visible. The dashed red lines are a guide for the eye to follow the trajectory of the frequency peaks. The curves for $d_{\text{foc}} < 1.75 \mu\text{m}$ are offset for clarity.

Ω_x and Ω_z . This is indicating a coupling between the oscillator modes. To characterize a coupling as weak or strong [68], we need to compare the frequency splitting to the sum of the peak linewidths. In our case the frequency splitting is smaller than the sum of the linewidths so we are in the weak coupling regime. We conjecture that the coupling mechanism is the anharmonicity of the potential, which is probed by a particle with large oscillation amplitudes, as mentioned for the $2\Omega_x$ peak. This coupling can be reduced by cooling the oscillators center-of-mass motion (Sec. 6.2).

Potential reconstruction

As we have seen in Sec. 2.2.2, the frequencies Ω_x , Ω_y and Ω_z are a direct measure of the curvature of the optical potential where the particle is trapped. As for the case of large distances d_{foc} (Sec. 3.2.1), we can reconstruct the optical potential probed by the particle at any time. To do so, we record a 60 s-long time trace of the particle motion at 1.5 mbar, for example at $d_{\text{foc}} = 390$ nm. Using again the Boltzmann distribution assumption, we extract from the histogrammed particle positions the potential $U(z)$ and plot it in Fig. 3.11. If we assume a harmonic oscillator, we can write along the optical axis

$$U(z) = \frac{1}{2}m\Omega_z^2z^2. \quad (3.5)$$

By fitting the reconstructed potential $U(z)$ with a quadratic function of the form βz^2 (green line in Fig. 3.11), we obtain the fit parameter $\beta = \frac{1}{2}m\Omega_z^2$. We can therefore calculate the oscillation frequency corresponding to the reconstructed potential and we find $\Omega_z = 2\pi \times 224$ kHz. This frequency shows a 12% deviation from the frequency $\Omega_z = 2\pi \times 256$ kHz that we observe in the PSD in Fig. 3.8(a). This deviation most likely originates from an inaccuracy in the calibration of the z axis [49, p. 80]. Moreover, we note that the reconstructed optical

3. APPROACHING PARTICLES TO PLANAR SURFACES

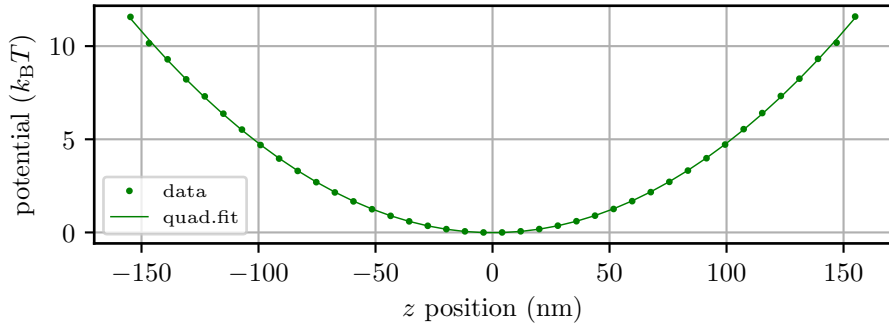


Figure 3.11: Reconstructed optical potential (green data points) along the z axis from a 60 s-long time trace of the particle position recorded at 1.5 mbar, for $d_{\text{foc}} = 390$ nm. To reconstruct the potential, we histogram the particle positions and assume they follow a Boltzmann distribution. We fit a quadratic function (green line) to the data and we extract an oscillation frequency $\Omega_z = 2\pi \times 224$ kHz.

potential appears very harmonic. It is not in contradiction with the remark we made in the previous paragraph about the anharmonicity of the potential showed by the avoided crossing and the presence of the $2\Omega_x$ peak. The reconstructed potential may appear quadratic even if it is in reality non-linear. Indeed, the oscillation frequency Ω_z is higher at $d_{\text{foc}} = 390$ nm than at $d_{\text{foc}} \approx 1.5$ μm , which means that a particle with constant energy probes less of the potential at $d_{\text{foc}} = 390$ nm than it does at $d_{\text{foc}} \approx 1.5$ μm [see Eq. (2.23)], especially not the outer regions of the potential, which feature the non-linearities.

3.3.2 Theoretical model: short distances analysis

In this section, we explain the expected modifications of the trapping field due to the presence of the membrane within a few micrometers from the focus.

Similar to the standard trapping experiment, the dielectric particle will be attracted towards regions of high intensity. In the standing wave configuration, where the membrane is closer than a few micrometers, there exist several local intensity maxima where the particle can be spatially confined, as we show in Fig. 3.12 with an intensity distribution in the xz plane (a) and along the optical axis z (b), for $d_{\text{foc}} = 0.5 \mu\text{m}$. Consequently, there are now several local optical potential minima, as we observe in Fig. 3.12 in the xz plane (c) and along the optical axis (d). These potential wells are deep enough to confine the particle [43]. We do not know *a priori* in which well the particle resides. This highly depends on the history of the potential landscape during the approach. As the membrane is approached, the potential landscape is constantly modified. To visualize more easily this constantly evolving optical potential, we plot it along z in Fig. 3.13 as a function of d_{foc} , *i.e.*, the membrane position. The potential profile displayed in Fig. 3.13(a) corresponds to $d_{\text{foc}} = 1.4 \mu\text{m}$. As we vary d_{foc} , we obtain many profiles that we gather in Fig. 3.13(b), for membrane positions ranging from $2 \mu\text{m}$ to $-0.2 \mu\text{m}$. We see in this figure how the different wells are pushed through the focus ($z = 0$) and how the depth of each well changes when we approach the membrane (represented by the purple slice) towards the focus.

Oscillation Frequencies in the multiple wells landscape

As we already explained, for a harmonic oscillator, we can deduce Ω_z from the optical potential, for each well.

3. APPROACHING PARTICLES TO PLANAR SURFACES

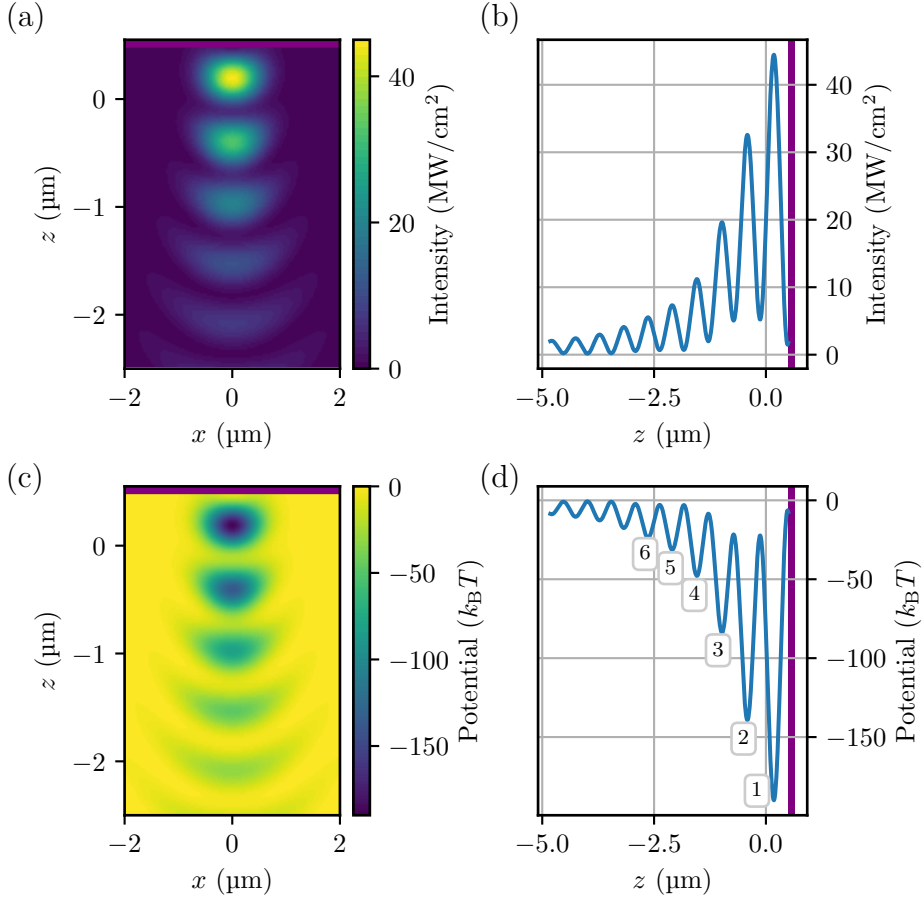


Figure 3.12: Calculated intensity distribution for $d_{\text{foc}} = 500$ nm, in the xz plane (a) and along the optical axis z (b). Corresponding calculated optical potential landscape in the xz plane (c) and along the optical axis z (d). The boxed numbers indicate the well numbers (starting with 1 for the closest to the membrane). The purple stripe represents the membrane position.

3.3. Potential mapping at short distances

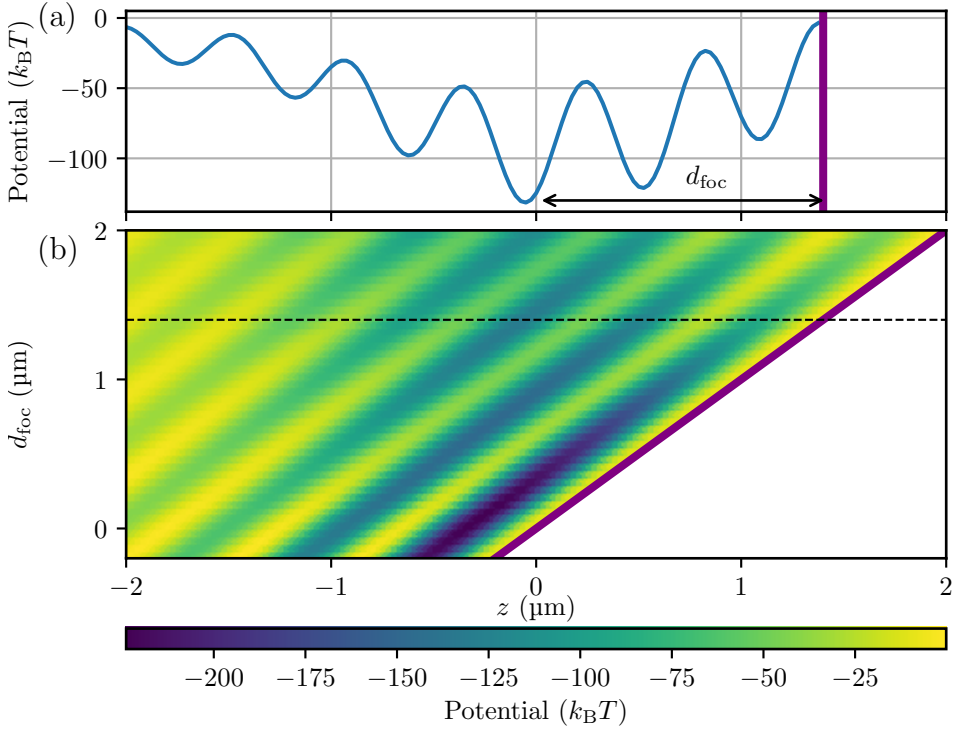


Figure 3.13: (a) Calculated optical potential profile along z for a distance $d_{\text{foc}} = 1.4 \mu\text{m}$. The membrane is schematically represented by the purple slab (thickness not to scale). (b) Evolution of the calculated potential landscape around the focal region as we vary d_{foc} . For $d_{\text{foc}} = 2 \mu\text{m}$, we observe many wells that are not very deep as the color contrast stays low. The two deepest wells are located around $z = 0$. On the contrary, for $d_{\text{foc}} < 0$, we see that one well is much deeper than the other ones (high color contrast). During the approach of the membrane, which corresponds to reading the plot in (b) vertically downwards, every potential well is scanned through the focal plane in the $-z$ direction, and its depth first increases when approaching the focal plane and then decreases as the well is shifted beyond the focal plane.

It is also possible to deduce Ω_x and Ω_y if we have the potential as a function of x and y but we focus here on the behavior of the

3. APPROACHING PARTICLES TO PLANAR SURFACES

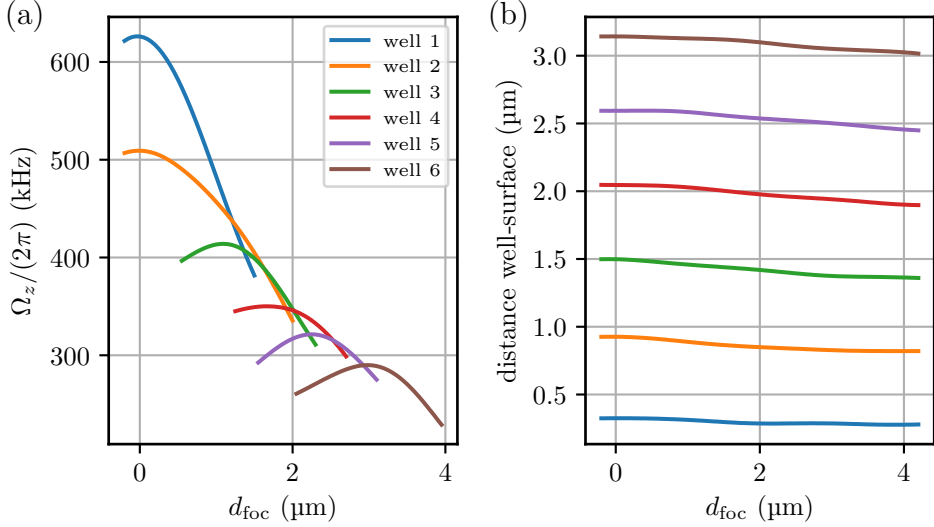


Figure 3.14: (a) Calculated oscillation frequency Ω_z as a function of focus-to-surface distance d_{foc} for the first six wells. (b) Separation between the bottom of the well and the membrane as a function of the distance d_{foc} , for the first six wells. The distance between two adjacent wells is roughly $\lambda/2$ and is increasing for decreasing d_{foc} values due to the contribution of the Gouy phase (see Chap. 4.2.2).

particle along the optical axis. For every position of the membrane, *i.e.*, for every d_{foc} value, the potential landscape is different from the one for the previous membrane position. Therefore, for every d_{foc} , the trap frequency of each well is also different. We can repeat the calculations from Eq. (3.1), *i.e.*, derive the Taylor expansion of the potential $U(z)$ for varying focus-to-surface distances d_{foc} , to get an idea of the evolution of the oscillation frequency during the experimental approach of the membrane towards the particle. In Fig. 3.14(a), we plot the trap frequencies Ω_z as a function of the focus-to-surface distance d_{foc} for the first six wells, calculated from the strongly focused beam model. We observe that, for $d_{\text{foc}} > 1 \mu\text{m}$, during the approach, the

frequency Ω_z of a well first rises until its maximum and then decreases. The frequency maximum is reached when the well is located close to the focal plane and is the deepest. For $d_{\text{foc}} < 1 \mu\text{m}$ (wells 1 and 2), Ω_z increases and reaches its maximum when the membrane is in the focus ($d_{\text{foc}} = 0$). The frequency evolution over the entire range of d_{foc} agrees qualitatively with the experiment in Fig. 3.8(a). In Fig. 3.14(b), we plot the distance between each well and the membrane as a function of d_{foc} . We notice that this separation stays rather constant, slightly increasing for decreasing d_{foc} . Furthermore, we remark that well 1 is displaced by $\sim 350 \text{ nm}$ when the membrane is in the focus.

Dynamics of the particle in a multiple-well landscape

We have analyzed the evolution of the potential landscape created by the trapping beam and its reflections from the membrane. Now we want to understand the motion and trajectory of the particle in such a landscape. To try to visualize the dynamics of our oscillator, we sketch three consecutive potential configurations in Fig. 3.15 and retrace the particle trajectory along the optical axis z . In (a), the particle is in well 4. As the membrane is moved towards the focal plane, the potential landscape is shifted towards the left and the particle is displaced along with the standing wave, staying in well 4. As the membrane is approached even further, the optical potential configuration becomes such that the potential barrier between well 4 and well 3 is small enough for the thermally activated particle to jump into well 3 [depicted in (b)]. With the particle now in well 3, the further approach of the membrane again shifts the potential landscape towards the left and the particle moves along, staying in well 3 (c) until the barrier between wells 3 and 2 will become small enough for the particle to cross. This process repeats itself until the particle sits in well 1 and is at the shortest distance to the membrane.

3. APPROACHING PARTICLES TO PLANAR SURFACES

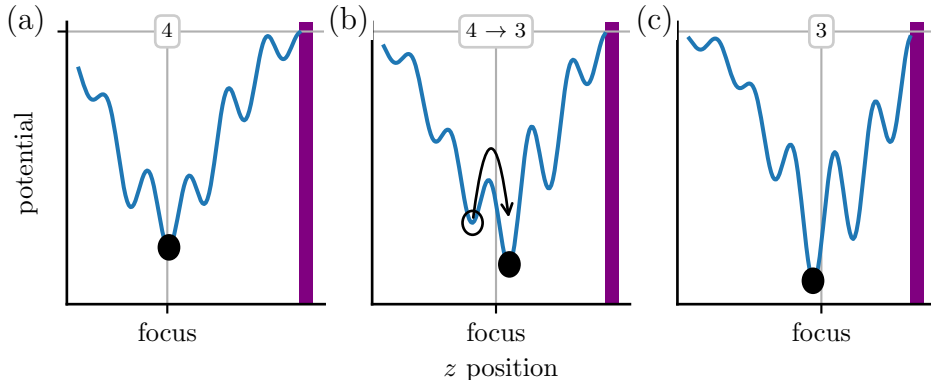


Figure 3.15: Sketches of the optical potential along the optical axis as the membrane is moved towards the focal plane, illustrating the transition of the particle from well 4 to well 3. (a) The particle is in well 4. (b) As the membrane is moved towards the focal plane, the optical potential landscape is shifted towards the left, and the particle is moved along. When the potential barrier between well 4 and well 3 is small enough, the particle can jump into well 3. (c) The particle now sits in well 3.

Simulation of the particle motion in a multiple-well landscape

For distances $d_{\text{foc}} < 5 \mu\text{m}$, we can perform similar simulations than for large focus-to-surface distances, still using the Gaussian beam approximation. However, the results of these simulations do not agree with the experimental observation. For example, simulating the membrane approaching from $d_{\text{foc}} = 2.4 \mu\text{m}$ to $d_{\text{foc}} = 0.4 \mu\text{m}$ predicts that the particle should stay in well 3 (the same parameters than in Table. 3.1 have been used). This is not what we observe experimentally in Fig. 3.8(a), where the particle jumps to from well 3 to well 2 and then to well 1. We consider this mismatch as a strong indication that the strongly focused beam model is even more indispensable when the region of interest is the focus itself. Unfortunately, a simulation including the strongly focused beam model has not yet been realized due to its very

high computational cost.

Limitations of the model

We have compared our experiments and the theoretical model we use to understand the particle behavior as the membrane is brought closer to the particle. Although we have observed qualitative agreements, we also notice some discrepancies which we discuss in this section.

The observation is that the model predicts deeper potential wells and higher oscillation frequencies Ω_z [Fig. 3.14(a)] than in the measurement [Fig. 3.8(a)]. We suspect that some experimental details have not been accounted for in the model.

The particle back action has already been taken into account by using the effective polarizability of the particle in the calculation of the optical potential [Eq. (2.7)]. But other forces than the optical forces have not been included in the model. Surface forces such as Casimir forces could have an influence on the particle, especially when it is close to the membrane. However, estimations [19] show a variation of the oscillation frequencies Ω_z of less than 1 kHz, which can not explain our observation. A more detailed analysis of the surface forces will be done in Chap. 6.

We then consider that experimental parameters might have been wrongly estimated for the model calculation, such as the trapping NA (which can be overestimated if the laser beam is not exactly of the diameter of the back aperture of the objective), the filling factor (which again depends on the diameter of the laser beam) or the dielectric constant of the SiN membrane [given by the manufacturer with a tolerance range ($6 \sim 7$)]. Experimental inaccuracies such as laser beam misalignment also impact the trap stiffness and therefore the oscillation frequencies. A tilted beam entering the objective would for example lead to effectively reducing the power transmitted through the objective and reducing the filling factor. However, varying these parameters in

3. APPROACHING PARTICLES TO PLANAR SURFACES

an experimentally reasonable range could not explain fully the lower experimental Ω_z .

Another assumption incriminates the surface roughness of the membrane, that can be due to material characteristics or to particles that adhered to the membrane (silica, dust). These imperfections would act like scatterers of the trapping light impinging on the membrane and therefore reduce the intensity of the reflected light that forms the standing wave. But the difference of factor 2 between expected and measured Ω_z would require only 1/16 of the trapping power to be reflected, while the rest is being scattered by these surface defects, which seems unreasonable.

So far, we assumed the membrane to be a rigid surface. But in reality, it is a drum that can vibrate and be displaced. The first mechanical mode is estimated to be around 2 kHz at room temperature, which is too low to impact on the particle motion. But radiation pressure from the trapping laser can in fact push the membrane in the propagation direction. An estimation¹⁰, assuming point load (which we consider to be an upper limit for the displacement due to radiation pressure [69, 70]) yields a displacement of the membrane of the order of 100 nm when the membrane is in the focal plane ($d_{\text{foc}} = 0$). The effect of radiation pressure is therefore to stretch non-uniformly the horizontal axis in Fig. 3.14(a) but does not affect the vertical axis Ω_z if we consider the membrane to stay a *planar* surface from the particle point of view. If the membrane would be deformed and acquire a finite radius of curvature, then the reflected field forming the standing wave would be affected and maybe the curvatures of the potential wells would be modified, resulting in different oscillations frequencies (see also Chap. 4). However, we conjecture that a curved membrane would result in higher intensities in the focal region, leading to higher oscillation frequencies, which is not what we see.

¹⁰based on a private note from L.Novotny

Finally, we consider the existence of electrostatic gradients that could affect the particle to second order. Indeed, in a homogeneous electrostatic field, the uncharged particle is not subject to a force. But if the electrostatic field has a gradient, the particle would get polarized and then feel a force. To rule out this hypothesis, we did the same measurement as the one shown in Fig 3.8 with a particle carrying one charge. This charged particle should be subject to an electrostatic force arising from the homogeneous electrostatic field, which is much stronger than possible gradients. However, the frequencies Ω_z measured during the membrane approach were exactly the same than in the case of the uncharged particle, showing that the electrostatic gradients can not be the reason for the deviation of the experimental Ω_z compared to the model.

3.4 Conclusion

In this chapter, we have approached a SiN membrane to an optically levitated silica nanoparticle. We have mapped the optical potential created by the trapping field and the field reflected from the membrane, using the levitated particle as a probe. To this end, we have observed the frequency behavior of the particle when the membrane was at large distances but also at short distances from the particle. In both situations, we have proposed a theoretical model to explain the experimental observations, supported by dynamic simulations whenever it was possible. We have found qualitative agreements between the experiments and the theory and have discussed the limitations of our model.

Chapter 4

Interferometric measurement of distances

So far, we have conducted all of our measurements as a function of the focus-to-surface distance d_{foc} . We have probed the optical potential created by the trapping beam and its reflection from the SiN membrane as a function of d_{foc} . However, for short distances d_{foc} , we have seen that the potential wells are deep enough for the particle not to reside in the focal plane but that it can be moved away from the focus. In such situations, the distance focus-to-surface d_{foc} and the distance particle-to-surface d_{part} are different. Since the particle is our optical potential probe, we need a precise measurement of its separation from the membrane surface. Therefore, in this section, we establish an independent interferometric measurement of the particle-to-surface distance d_{part} . It is important to note that, in the following section, we consider the distance d_{part} averaged over the particle oscillations. On the contrary, we have previously observed the variation of d_{part} over one oscillation in Fig. 3.4 (b).

4.1 Experimental setup

To measure the particle-to-surface distance d_{part} , we use an interferometric technique based on the interference between the scattered light from the particle and the light which is scattered by the particle and is then back reflected from the membrane.

The experimental setup is shown in Fig. 4.1. Because most of the light back reflected from the membrane is originating from the trapping beam ($\lambda_{\text{trap}} = 1064 \text{ nm}$) that did not interact with the particle, the signal to noise ratio of the trapping-light interference signal is expected to be very low. To circumvent this issue, we use a green laser ($\lambda_{\text{G}} = 532 \text{ nm}$) to illuminate the optically trapped particle from the side. Using a different wavelength than 1064 nm allows us to minimize noise and background signals by spectrally separating the green light from the trapping light. Therefore, in addition to the previously explained optical trapping setup, a green laser beam (80 mW), linearly polarized along y , is focused on the particle from the side using a low NA lens to obtain a weakly focused green laser beam, with a waist of a few tens of micrometers. The green light scattered by the particle is collected with the trapping objective and separated from the 1064 nm light using a dichroic mirror (DM). The lenses L1 ($f_1 = 250 \text{ mm}$) and L2 ($f_2 = 200 \text{ mm}$) are placed such that the back focal plane of the objective is imaged on the camera (CCD). The signal impinging on the CCD is the interference between the light directly scattered by the particle, and the light scattered by the particle and reflected by the membrane, similar as in self-interference microscopy [71].

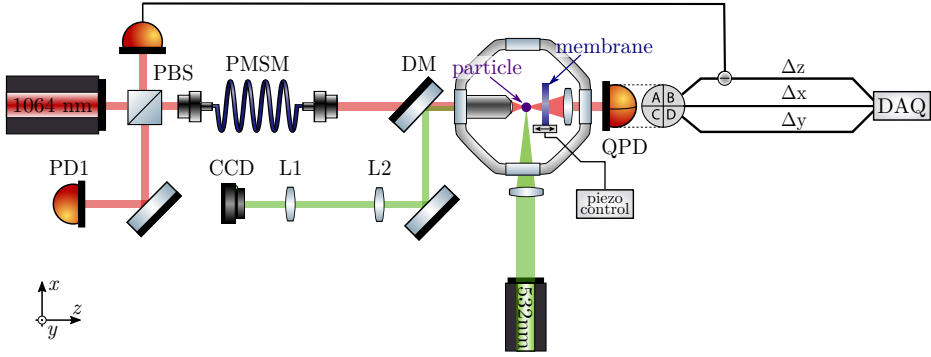


Figure 4.1: Experimental setup with the addition of a green laser for the interferometric measurement of d_{part} . The green beam ($\lambda_G = 532 \text{ nm}$, $\approx 80 \text{ mW}$) is weakly focused on the particle from the side. The trapping objective collects the scattered green light that gets separated from the back-reflected trapping light by a dichroic mirror (DM). The back focal plane of the objective is imaged on a camera (CCD) by the means of two lenses (L1 and L2). The signal imaged on the CCD originates from the interference of the light scattered by the particle directly and the light scattered by the particle which is then reflected from the membrane.

4.2 Interferometric measurement

4.2.1 Back-focal-plane imaging: results and model

By imaging the back focal plane of the objective [72], we observe the dipolar radiation pattern of a point scatterer, modulated with a specific ring pattern, in which the information about the distance between the particle and the surface is encoded. We display such an image in Fig. 4.2(a), recorded for $d_{\text{foc}} \approx 4.2 \mu\text{m}$. The ring structure (7 concentric bright rings) is an interference pattern that depends on the phase difference between the two fields interfering, *i.e.*, that depends on the distance d_{part} between the point scatterer and the reflecting surface. The components of the wave vector k_x and k_y are related

4. INTERFEROMETRIC MEASUREMENT OF DISTANCES

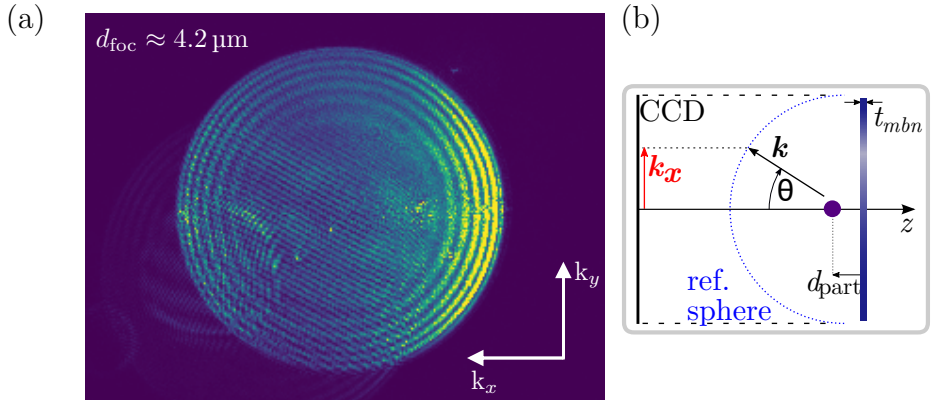


Figure 4.2: (a) Measured back-focal-plane image for $d_{\text{foc}} \approx 4.2 \mu\text{m}$. We witness the interference pattern of concentric bright rings. The very narrow straight fringes and the lateral intensity asymmetry are experimental imperfections. (b) Geometry of the interferometric measurements. k_x and k_y denote the in-plane components of the wavevector. The intensity distribution evaluated on the reference sphere is projected onto the CCD. The position on the CCD depends on the emission angle of the light, which depends on the particle-to-surface distance d_{part} .

to the emission angle θ by $k \sin(\theta) = \sqrt{k_x^2 + k_y^2}$. The geometry of the measurement is depicted in Fig. 4.2(b). The intensity asymmetry along k_x appears due to unwanted reflection of the green light from other optical elements in the vacuum chamber. However, the sides being brighter than the top and bottom is a characteristic of linearly polarized dipole emission (polarization along y). We also observe a lot of straight and faint stripes at a higher spatial frequency, that are caused by reflections from the other elements in the vacuum chamber.

Our goal is to extract the particle-to-surface distance d_{part} from these back-focal-plane images. To this end, we implement a theoretical model that predicts the back-focal-plane images depending on parameters gathered in Tab. 4.1, amongst which the distance d_{part} is listed. We

leave the membrane thickness t_{mbn} as a fitting parameter as we *a priori* do not know its exact value within the tolerance range provided by the manufacturer. The theoretical model is based on Ref. [57, pp. 312ff.] and we summarize the main points below.

We are interested in the far-field emission of a dipole close to a planar interface between two media, in our case air and SiN. The excitation field \mathcal{E}_{exc} (green laser beam) is linearly polarized along the y axis. Therefore the dipole moment of the particle is

$$\begin{bmatrix} p_x \\ p_y \\ p_z \end{bmatrix} = \begin{bmatrix} 0 \\ \alpha \mathcal{E}_{\text{exc}}^y \\ 0 \end{bmatrix}. \quad (4.1)$$

We can then evaluate the far-field \mathcal{E}_{FF} using [57, p. 325]

$$\begin{aligned} \mathcal{E}_{\text{FF}} &= \begin{bmatrix} \mathcal{E}_\theta \\ \mathcal{E}_\phi \end{bmatrix} \\ \mathcal{E}_{\text{FF}} &= \frac{k^2}{4\pi\epsilon_0\epsilon_{\text{air}}} \frac{\exp(ikr)}{r} \begin{bmatrix} (p_x \cos \phi + p_y \sin \phi) \cos \theta \Phi^{(2)} - p_z \sin \theta \Phi^{(1)} \\ -(p_x \sin \phi - p_y \cos \phi) \Phi^{(3)} \end{bmatrix} \end{aligned} \quad (4.2)$$

with

$$\begin{aligned} \Phi^{(1)} &= \exp(-ikd_{\text{part}} \cos \theta) + r_{\text{slab}}^{\text{p}}(\theta) \exp(ikd_{\text{part}} \cos \theta), \\ \Phi^{(2)} &= \exp(-ikd_{\text{part}} \cos \theta) - r_{\text{slab}}^{\text{p}}(\theta) \exp(ikd_{\text{part}} \cos \theta), \\ \Phi^{(3)} &= \exp(-ikd_{\text{part}} \cos \theta) + r_{\text{slab}}^{\text{s}}(\theta) \exp(ikd_{\text{part}} \cos \theta), \end{aligned} \quad (4.3)$$

where θ and ϕ are the angles defined in Fig. 2.4(a), ϵ_{air} is the dielectric constant of air, r the radius of the reference sphere where we evaluate the electric field [as defined in Fig. 2.4(a)] and $r_{\text{slab}}^{\text{p}}(\theta), r_{\text{slab}}^{\text{s}}(\theta)$ the Fresnel reflection coefficients for the membrane defined in Eq. (3.4), depending on the incident angle of the light θ .

4. INTERFEROMETRIC MEASUREMENT OF DISTANCES

The field components \mathcal{E}_θ and \mathcal{E}_ϕ are then calculated for $\theta \in [0, \pi/2]$, $\phi \in [0, 2\pi]$, which correspond to the half sphere of back-scattered light. We can deduce the intensity on this half sphere by $I_{\text{tot}} \propto (\mathcal{E}_\theta \mathcal{E}_\theta^* + \mathcal{E}_\phi \mathcal{E}_\phi^*)$. As we want to calculate the intensity distribution representing a back-focal-plane image, the distribution on the half sphere needs to be projected onto a plane. Therefore, we plot $I_{\text{tot}}/\cos\theta$ for theoretical back-focal-plane images. To take into account the collection NA, we only plot the calculated intensity for $\sin\theta < 0.9$. To represent the experimental conditions in our model more accurately, we also consider the oscillation amplitude of the particle in our calculations. Indeed, the oscillation causes a variation of the particle position along the z axis in time, causing a concomitant variation of the ring pattern in the back focal plane. Since the particle oscillations are much faster than the acquisition time of one back-focal-plane image with the CCD, the resulting image is an average over several ring patterns. We therefore calculate the superposition of the different patterns by calculating the

Table 4.1: Parameters used in the back-focal-plane imaging model. Besides the overall power, the fitting parameters are d_{part} and t_{mbn} .

Parameter	Value
Collection NA (trapping objective)	0.9
Particle diameter	136 nm
Wavelength λ_G	532 nm
Refractive index of fused silica	1.45
Nominal mass of the particle	2.01×10^{-18} kg
Membrane thickness t_{mbn}	fitting parameter
Distance d_{part}	fitting parameter
Refractive index of SiN	2.54

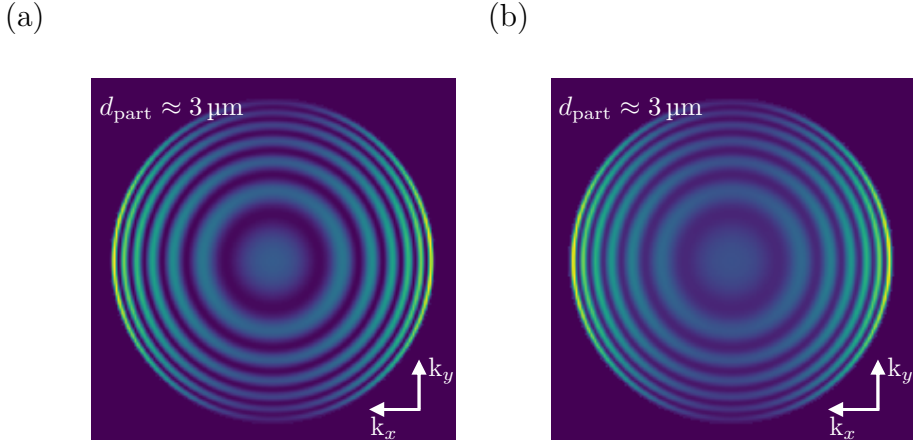


Figure 4.3: Calculated back-focal-plane intensity distribution, using the parameters from Tab. 4.1, $d_{\text{part}} = 3 \mu\text{m}$ and $t_{\text{mbn}} = 500 \text{ nm}$. (a) The particle position along z is fixed at $3 \mu\text{m}$. (b) The back-focal-plane images are averaged according to the particle positions distribution, corresponding to an oscillation frequency $\Omega_z = 100 \text{ kHz}$, *i.e.*, a root-mean-square oscillation amplitude around 50 nm . We observe that the averaging only results in a decrease of the fringe visibility but does not affect the spatial distribution of the interference rings.

intensity pattern for several particle positions and weighing them with the position probability, assuming a Boltzmann distribution for the potential energy of the particle, like in Sec. 3.2.1. Thus, our weighing function is

$$\mathcal{W} = \frac{1}{B} \exp\left(\frac{-m\Omega_z^2(z - d_{\text{part}})^2}{2k_{\text{B}}T}\right) \quad (4.4)$$

with the normalization factor $B = \sqrt{\frac{2\pi k_{\text{B}}T}{m\Omega_z^2}}$.

Resulting theoretical back-focal-plane images are shown in Fig. 4.3 for $d_{\text{part}} = 3 \mu\text{m}$ and a membrane thickness of $t_{\text{mbn}} = 500 \text{ nm}$, (a)

without and (b) with the averaging over the particle positions, respectively. We recognize the bright sides, resulting from the linear polarization of the dipole scatterer and the interference ring pattern (6 bright rings). We notice that the averaging over the particle positions only modifies the image slightly, resulting in a decrease of the contrast between bright and dark fringes. But the spatial distribution of the rings stays identical as expected. All the theoretical back-focal-plane images shown in the rest of this chapter have taken into account the particle oscillations in the intensity distribution. We can now measure the back-focal-plane images of the trapped particle and obtain d_{part} continuously during measurements by fitting those measurements with the developed theoretical model. We perform this interferometric measurement simultaneously with the approach of the membrane performed in Fig. 3.8(a) and therefore deduce the value of d_{part} for each value of d_{foc} .

4.2.2 Measurement of d_{part} during the membrane approach

While performing the membrane approach shown in Fig. 3.8(a), we record the back-focal-plane images every 250 ms with the CCD camera. We display the recorded image at $d_{\text{foc}} = 2.34 \mu\text{m}$ (particle in well 3) in Fig. 4.4(a, left). Comparing recorded 2D images with theoretical ones is not a very accurate way of determining the distance d_{part} from the measured image. To precisely extract d_{part} from a measured back-focal-plane image, we therefore radially average the intensity distribution and obtain an intensity profile plotted with blue data points in Fig 4.4(b). On the horizontal axis, we plot the sine of the angle θ , with $\sin \theta_{\text{max}} = 0.9 = \text{NA}$. To eliminate the intensity signal coming from directly scattered light not originating from the particle (that is considered as *noise* in the intensity profile), we subtract the

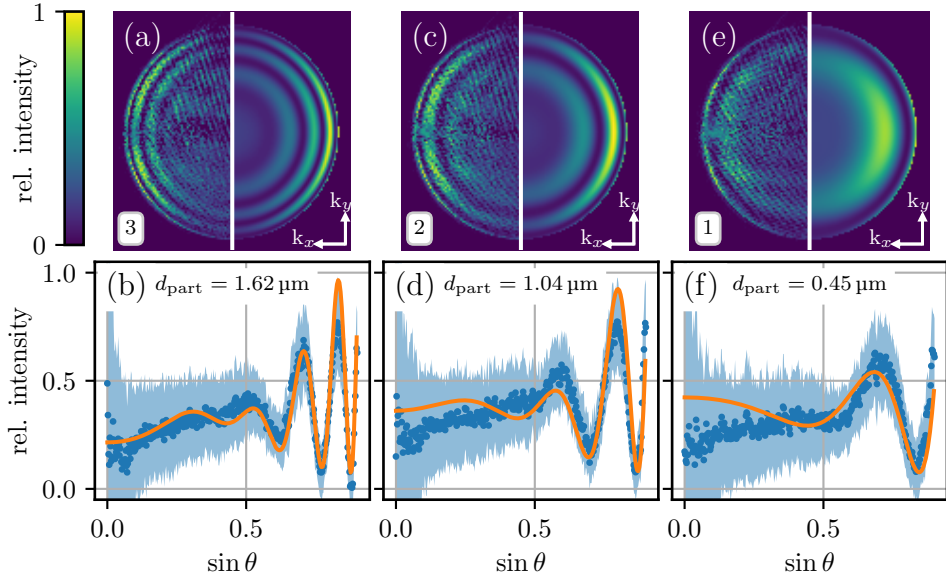


Figure 4.4: Back-focal-plane imaging of a nanoparticle levitated in front of a SiN membrane. (a, left) Measured back-focal-plane image at $d_{\text{foc}} = 2.34 \mu\text{m}$. (a, right) Calculated back-focal-plane image intensity distribution for a scatterer levitated at $d_{\text{part}} = 1.62 \mu\text{m}$ [extracted from the fit in (b)]. (b) Radially average intensity profile (blue points) of the measured image in (a). The blue shaded area represents the experimental standard deviation. We fit (orange curve) the intensity profile according to our model and extract the value $d_{\text{part}} = 1.62 \mu\text{m}$. Panels (c,d) and (e,f) analog to (a,b) but for images recorded at $d_{\text{foc}} = 1.62 \mu\text{m}$ (particle in well 2) and $d_{\text{foc}} = 0.18 \mu\text{m}$ (particle in well 1), respectively. Adapted with permission from Ref. [66].

4. INTERFEROMETRIC MEASUREMENT OF DISTANCES

background intensity from the measurement intensity profile with particle. Note that removing the background in this way does not eliminate the interference between the signal and the background. The background intensity profile is recorded at exactly the same position d_{foc} as the measurement intensity profile but without particle. The blue shaded area indicates the experimental standard deviation after background subtraction. We note that the standard deviation is much smaller for high $\sin\theta$ values, which originates from the fact that a radial average contains more data points for the outer radii than for the central part of the image. We then fit the intensity profile with the model described previously [orange curve in Fig 4.4(b)]. Our fitting function is based on the least squares model, with d_{part} and t_{mbn} as fitting parameters¹ and weighs the importance of each data point in the minimization residuals according to the measured standard deviation. In other words, the fitting function attributes a higher importance to the intensity points at large $\sin\theta$ values. We obtain the best fit for $d_{\text{part}} = [1.62 \pm 0.05(\text{sys}) \pm 0.0002(\text{stat})] \mu\text{m}$. We estimate the systematic error on d_{part} based on the residuals from the fit (twice the minimum residual). The statistical error is calculated by evaluating d_{part} for repeated measurements at the same membrane position, and amounts to 0.2 nm. For visual comparison, we display in Fig. 4.4(a, right) the theoretical image calculated for the extracted value $d_{\text{part}} = 1.62 \mu\text{m}$. We observe a good agreement. We go through the same process for back-focal-plane images recorded at $d_{\text{foc}} = 1.62 \mu\text{m}$ (particle in well 2) and $d_{\text{foc}} = 0.18 \mu\text{m}$ (particle in well 1), and display these images in Fig. 4.4(c, left) and (e, left) respectively. We observe that the number of rings decreases for smaller distances d_{foc} , as expected. Our analysis of the corresponding radially averaged intensity profiles [shown in Fig. 4.4(d)

¹We left the membrane thickness t_{mbn} as a fitting parameter for all the images, as a sanity check regarding the meaningfulness of the fit. An unreasonable value of t_{mbn} would mean that the fit probably failed and the corresponding d_{part} value should be ignored.

and (f)] yields particle-to-surface distances of $d_{\text{part}} = 1.04 \mu\text{m}$ and $d_{\text{part}} = 450 \text{ nm}$. We acknowledge a smaller agreement between the theory and the experiment in Fig. 4.4(f), that we attribute to the fact that, in well 1, the particle-to-surface distance and the particle size become of similar order of magnitude, which does not fully correspond to the point-dipole-scattering assumption we have made in the model.

We show in Fig. 4.5 the extracted d_{part} as a function of d_{foc} , during the entire membrane approach. The data points circled in orange correspond to the images displayed in Fig. 4.4. We firstly notice the discrete steps in d_{part} values to coincide exactly with the frequency discontinuities observed in Fig. 3.8(a), because both effects arise from the particle jumping from one well to another. Secondly, we note that besides the overall power and d_{part} , the membrane thickness t_{mbn} is also extracted for every image. We consistently obtain a value $t_{\text{mbn}} = (516 \pm 1) \text{ nm}$, which lies within the tolerance range provided by the membrane manufacturer $[(500 \pm 25) \text{ nm}]$. Finally, we measure the step size in d_{part} to be around $\lambda/2$, which correspond to the spacing between intensity maxima in a standing wave and therefore further supports our theoretical model, which is based on the standing wave structure. However, two peculiarities are observed in the measurement displayed in Fig. 4.5, namely that the step size increases for small d_{foc} and that the distance d_{part} in well 1 is larger than expected from our calculation in Fig. 3.14(b). We will discuss these two points successively.

We attribute the increase in the step height for small d_{foc} values to the Gouy phase that is acquired in the focus of a laser beam. To justify this attribution, we proceed with a simplified calculation of a Gaussian beam reflected from a planar single dielectric interface located at d_{foc} (the focal plane is located at $z = 0$) and we calculate the intensity distribution along the optical axis z . We assume the Gaussian beam

4. INTERFEROMETRIC MEASUREMENT OF DISTANCES

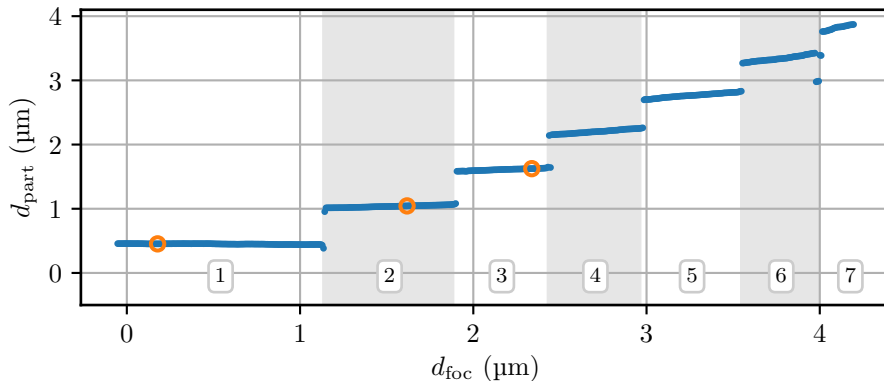


Figure 4.5: Values of d_{part} extracted from the fit of the measured back-focal-plane images as a function of d_{foc} . We observe steps in d_{part} , corresponding to the jump of the particle into the next well. The corresponding values of d_{foc} for these steps perfectly match the positions of the frequencies discontinuities witnessed in Fig. 3.8(a). The step height increases for decreasing d_{foc} due to the existence of the Gouy phase in the focus. The boxed numbers indicate the well number. The orange circles locate the three examples of back-focal-plane images shown in Fig. 4.4.

of the form [43] :

$$\mathcal{E}_{\text{Gauss}}(z) = \mathcal{E}_0 \left(1 + \frac{z^2}{z_0^2} \right)^{-1/2} \exp(i\Phi), \quad (4.5)$$

where $\Phi = kz - \eta(z)$ with $\eta(z) = \arctan(z/z_0)$ being the Gouy phase and z_0 the Rayleigh length. We calculate the intensity I as

$$I = [\mathcal{E}_{\text{Gauss}}(z) + R\mathcal{E}_{\text{Gauss}}(2d_{\text{foc}} - z) \exp(i\pi)] \times [\mathcal{E}_{\text{Gauss}}^*(z) + R\mathcal{E}_{\text{Gauss}}^*(2d_{\text{foc}} - z) \exp(-i\pi)] \quad (4.6)$$

with R the reflection Fresnel coefficient for this dielectric interface (R is real) and $\exp(i\pi)$ coming from the reflection-induced phase shift.

After simplification, we find

$$I = B^2 + C^2 - 2BC \cos[2k(z - d_{\text{foc}}) + \eta(2d_{\text{foc}} - z) - \eta(z)] \quad (4.7)$$

with $B = \mathcal{E}_0 \left(1 + \left(\frac{z}{z_0}\right)^2\right)^{-1/2}$, $C = R\mathcal{E}_0 \left(1 + \frac{4d_{\text{foc}}^2 - 4d_{\text{foc}}z + z^2}{z_0^2}\right)^{-1/2}$. The term $2k(z - d_{\text{foc}})$ is the propagation-induced phase delay. To know the position of the potential wells along the optical axis, we need to look for the intensity maxima, *i.e.*, when the cosine term is minimal. We plot in Fig. 4.6(a) this cosine function as a blue curve, for $d_{\text{foc}} = 100$ nm and $z_0 = 1362$ nm [43, pp. 31f.]. For comparison, we plot in orange the same function but for no Gouy phase ($\eta = 0$). We measure the separation between two consecutive minima and plot it in Fig. 4.6(b), for both cases, with or without Gouy phase. We observe that in the absence of Gouy phase (similarly to a plane wave case), the separation between adjacent wells is constant and equal to $\lambda/2$. On the contrary, in the presence of Gouy phase, this separation increases the closer the wells are from the surface. This corresponds to our observation in Fig. 4.5 and was also observed in Fig. 3.14(b) in the simulation which accounts for the Gouy phase. Additionally, we note a slight displacement of well 1 due to the Gouy phase.

We now turn to the discussion concerning the value $d_{\text{part}} = 450$ nm for well 1. This distance is set by the complex reflection coefficient of the dielectric membrane and depends on both the refractive index and the thickness of the membrane. Some analytical expressions can be found in the literature [73, 74] that relate the position of the closest well with the refractive index and the membrane thickness. However, in Refs. [73, 74], the weakly focused beam approximation was made, from which we know that it does not describe our experiment accurately. Estimations from both the literature and our calculation in Fig. 3.14(b) seem to underestimate the distance between well 1 and the surface (by 25% for our model, by 40% for literature models). A possible reason for

4. INTERFEROMETRIC MEASUREMENT OF DISTANCES

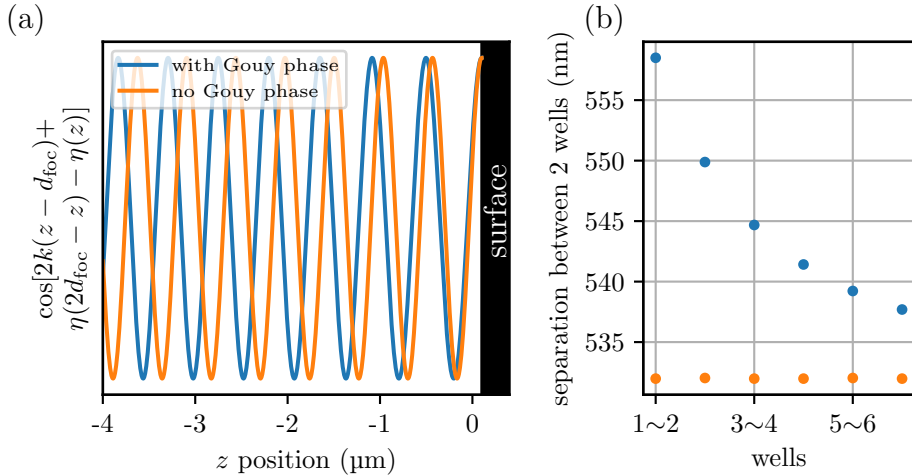


Figure 4.6: (a) Calculation of the interference term of a Gaussian beam with wavelength $\lambda = 1064$ nm reflected from a semi-infinite dielectric surface along the optical axis z , located at $d_{\text{foc}} = 100$ nm. The blue plot takes into account the existence of the Gouy phase, the orange plot does not (similar to a plane wave). We plot the cosine component of the intensity, and we look at the minima of the cosine function, which correspond to the positions of optical potential wells. We see that the existence of the Gouy phase shifts the minima position away from the surface. (b) We measure the separation between two consecutive minima of the cosine function in (a) and plot it as a function of well number. The terminology “1 ~ 2” signifies “between well 1 and well 2”. We observe that for a plane wave model (no Gouy phase), the separation between two consecutive wells is constant (orange points) whereas it increases for the model including the Gouy phase the closer we are to the surface (blue points).

this mismatch could be the fact that the membrane acquires a curvature due to radiation pressure, and we want to verify this hypothesis in the following. From the membrane displacement due to radiation pressure calculated in Sec. 3.3.2, which is around 100 nm, we can estimate the radius of curvature of the deformed membrane. Assuming the membrane is deformed spherically where the laser beam is impinging, and is linearly stretched otherwise, we find a corresponding radius of curvature of 5 mm. Using a simplified model based on ABCD matrix for a weakly focused beam reflected on a curved surface with radius of curvature 5 mm, we can estimate the displacement of well 1 due to this curvature. We find a displacement of the order of a few nm (away from the membrane).

We conclude that both the Gouy phase and the deformation of the membrane contribute to a minor displacement of well 1 away from the membrane. However, the approximations performed do not allow us to conclude that these two effects are solely responsible for the discrepancy between model and experiments.

4.3 Conclusion

We have measured the particle-to-surface distance d_{part} for all membrane positions using an interferometric technique. Our particle having a radius of 68 nm, we claim a minimum net distance between the surface of the particle and the surface of the membrane of 380 nm. We have discussed the discrepancy between our theoretical model and the experiment regarding the distance between well 1 and the surface of the membrane, identifying the Gouy phase and the membrane deformation as possible causes. Additionally, we note that the extraction of d_{part} using the back-focal-plane images is very sensitive to the NA of the objective, whose value we assumed constant and equal to 0.9, as provided by the manufacturer of the objective.

Chapter 5

Active control of the particle-to-surface distance

We have mapped out the optical potential created by a strongly focused beam reflected from a SiN membrane, using a levitated silica nanoparticle as a probe. We have been able to precisely position the nanoparticle anywhere within this potential landscape, and especially at subwavelength distance from the membrane. Indeed, when the particle resides in the potential well closest to the membrane, the particle-to-surface distance was measured to be $d_{\text{part}} = 450$ nm. Yet, this distance is set by experimental parameters, like the membrane thickness and the membrane refractive index, which cannot be tuned in-situ. It would be interesting to be able to tune the distance d_{part} to bring more versatility to the experiments we can perform. To this end, we introduce in this chapter an additional electromagnetic field, to control the standing-wave pattern where the particle is trapped. The experiments and the calculations are carried out with a 200 nm-thick SiN membrane.

5.1 The optical conveyor belt concept

The idea behind an optical conveyor belt is to spatially displace a standing-wave pattern generated by two counter-propagating beams. This technique is already used in the atom-trapping community [75, 76], where acousto-optic modulators are utilized to detune the two counter-propagating beams in frequency in order to create a moving standing wave. Optical conveyor belts have also been applied in optical tweezer applications [77, 78]. Instead of a frequency detuning between the two counter-propagating beams, we will, in the following, consider shifting the phase of one of the fields constituting the standing wave. Let's consider two counter-propagating monochromatic plane waves expressed as $\mathcal{E}_1 e^{i(kz - \omega t)}$ and $\mathcal{E}_2 e^{i(-kz - \omega t + \phi_{CB})}$, where ϕ_{CB} is the phase difference between the two waves. These two waves interfere to form a standing wave with the intensity $I = |\mathcal{E}_1|^2 + |\mathcal{E}_2|^2 + 2|\mathcal{E}_1||\mathcal{E}_2| \cos(2kz - \phi_{CB})$. We can see that adjusting the phase ϕ_{CB} results in spatially displacing the standing wave along the propagation axis z . This is the concept we will use to spatially shift the trapping potential.

5.2 Experimental setup

We sketch in Fig. 5.1 the experimental setup used to realize a controllable standing wave. After the vacuum chamber, we introduce a beamsplitter (90:10) that picks up 90% of the power of the beam to focus it on an additional mirror (not present in the setup used in the previous chapters) through the lens L3 ($f_3 = 100\text{mm}$). This additional mirror is fixed to a piezoelectric actuator (we call it piezo-mirror for clarity) and can be displaced along the optical axis with a precision below 0.05 nm over a range of 3 μm . Note that in this chapter, the trapping objective is an Olympus 100x (NA = 0.85, focal length $f = 1.8\text{mm}$). In the inset of Fig. 5.1, we illustrate the new field configuration in the

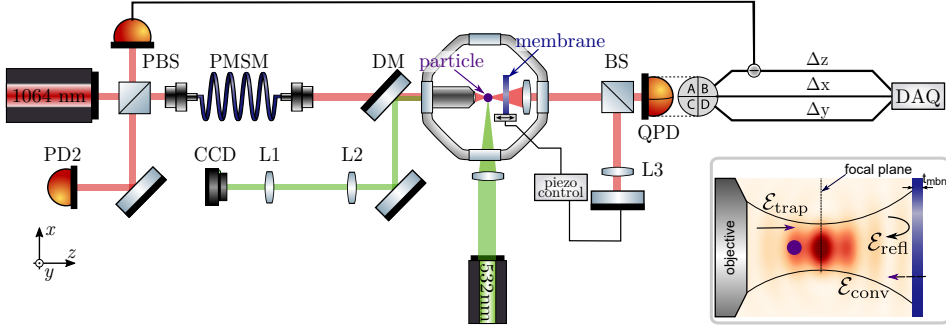


Figure 5.1: Experimental setup allowing for a shift of the potential wells along the optical axis. The setup is identical as previously introduced in Chap. 4, except for the trapping objective (NA = 0.85), an additional beam splitter (BS), a lens L3 and a mirror placed after the vacuum chamber. The additional mirror is mounted on a piezoelectric actuator, enabling us to modulate its position along the optical axis, with a precision below 0.05 nm. Inset: Sketch of the different fields interacting in the focal region. The new field $\mathcal{E}_{\text{conv}}$ is created by the reflection from the piezo-actuated mirror followed by the transmission through the membrane. It interferes with the trapping field $\mathcal{E}_{\text{trap}}$ and the field reflected from the membrane $\mathcal{E}_{\text{refl}}$. The standing-wave pattern is now resulting from the interference between the three fields.

focal region. The forward propagating trapping field $\mathcal{E}_{\text{trap}}$ is partially reflected by the membrane ($\mathcal{E}_{\text{refl}}$) and partially transmitted through the membrane. The transmitted field hits the piezo-mirror and gets partially transmitted again through the membrane, to give the field $\mathcal{E}_{\text{conv}}$.

5.3 Theoretical considerations

In this section, we calculate the intensity distribution along the optical axis z in the focal region (see inset Fig. 5.1). The treatment follows the methods introduced in Sec. 3.2.2, with the important difference that

5. ACTIVE CONTROL OF THE PARTICLE-TO-SURFACE DISTANCE

we include a counter-propagating beam $\mathcal{E}_{\text{conv}}$, such that the intensity distribution in the focal region arises from the interference of not two but three fields $\mathcal{E}_{\text{trap}}$, $\mathcal{E}_{\text{refl}}$ and $\mathcal{E}_{\text{conv}}$. The interference between $\mathcal{E}_{\text{trap}}$ and $\mathcal{E}_{\text{refl}}$ is calculated following Eq. (3.3), with a membrane thickness of $t_{\text{mbn}} = 200$ nm and a membrane refractive index of 2.54. We assume $\mathcal{E}_{\text{conv}}$ to be a Gaussian beam strongly focused with the collection lens of the form $\mathcal{E}_{\text{conv}} = \mathcal{E}_{\text{conv}} e^{i\phi_{\text{CB}} \mathbf{n}_x}$, where ϕ_{CB} is the adjustable phase. $\mathcal{E}_{\text{conv}}$ is calculated using the model described in Sec. 2.2.1 and with the parameters summarized in Table 5.1. To calculate the total field, we perform $D\mathcal{E}_{\text{conv}} + \mathcal{E}_{\text{trap}} + \mathcal{E}_{\text{refl}}$, where D is an amplitude correction factor. D includes the power losses due to the optical elements in the beam path (beam splitters, lenses, windows, transmission through the membrane). We plot the resulting optical potential along the optical axis z as a function of the phase ϕ_{CB} in Fig. 5.2(b), for a focus-to-surface distance $d_{\text{foc}} = 0$ and $D = 0.3$. The purple line at $z = 0$ represents the membrane (thickness $t_{\text{mbn}} = 200$ nm) and Fig. 5.2(a) shows in red the potential profile extracted from (b), at the position indicated by the dashed red line. A change of ϕ_{CB} shifts the optical potential wells along z . We observe that well 2 for $\phi_{\text{CB}} = 0$ becomes well 1 for $\phi_{\text{CB}} > 2\pi$. Accordingly, by varying the phase ϕ_{CB} , we can continuously tune the particle-to-surface distance d_{part} without the particle having to jump into a different well. It turns out that the

Table 5.1: Parameters used in the calculation of $\mathcal{E}_{\text{conv}}$.

Parameter	Value
Wavelength	1064 nm
NA (collection lens)	0.83
Focal length (collection lens)	15 mm

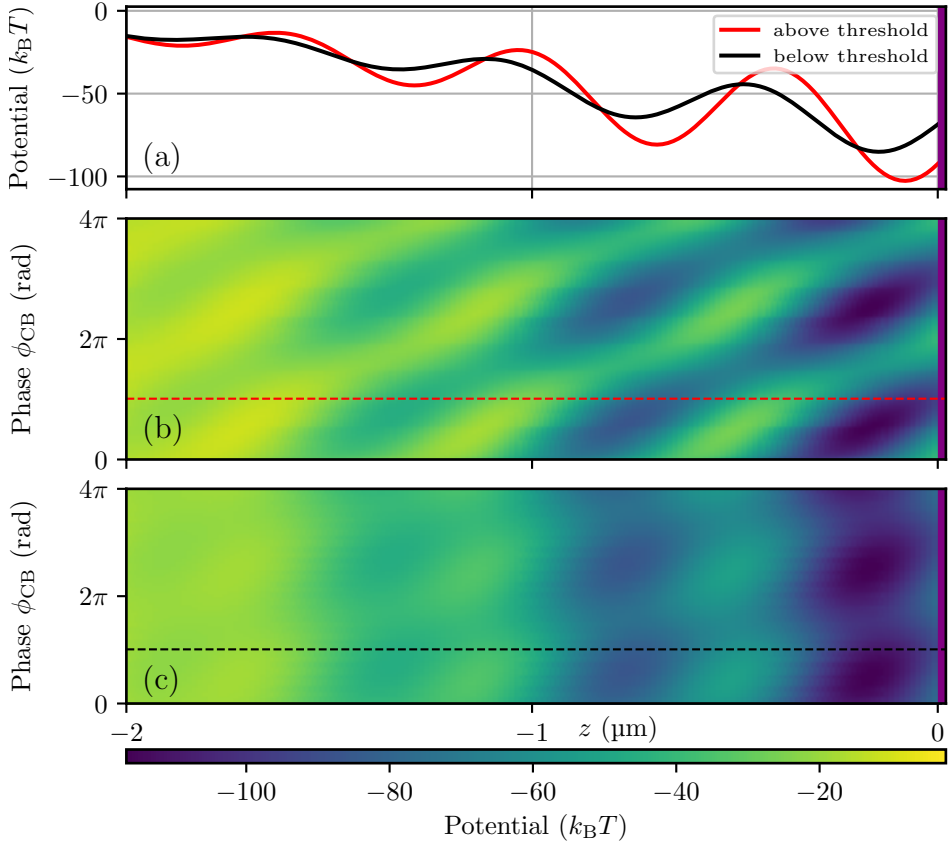


Figure 5.2: Calculated optical potential along z for $d_{\text{foc}} = 0$. (a) Potential profiles for $\phi_{\text{CB}} = \pi$, in the above-threshold configuration (red) and in the below-threshold configuration (black). (b) Potential as a function of the phase ϕ_{CB} of the additional reflected field $\mathcal{E}_{\text{conv}}$ for the above-threshold configuration. The dashed red line corresponds to the red profile in (a). An increase in the phase ϕ_{CB} , originating from a displacement of the piezo-mirror, results in a linear and continuous shift of the potential wells towards the membrane. The membrane is represented by a purple slice (thickness not to scale). (c) Potential as a function of the phase ϕ_{CB} for the below-threshold configuration. The dashed black line corresponds to the black profile in (a). A change in the phase ϕ_{CB} results in an oscillation of the well position around a mean value and not into a continuous shift. The position of a well cannot be tuned more than a few tens of nm.

membrane thickness is a critical experimental parameter. The main difference between different membrane thicknesses is the reflection coefficient. We show in Fig. 5.2(c) a plot corresponding to the one in Fig. 5.2(b), but where D has been reduced by 80% ($D = 0.06$). We notice that a change in the phase ϕ_{CB} is not sufficient anymore to shift the wells along z . The depth of the wells varies with ϕ_{CB} but their position along z stays constant. That means there exists a threshold for the intensity of the “tunable field” $\mathcal{E}_{\text{conv}}$, below which the change in phase ϕ_{CB} does not change the z position of the potential wells ($D = 0.3$ seems to be the threshold value of D allowing the shift of the wells along z , as we also have to ensure that the well where the particle resides remains deeper than $10k_{\text{B}}T$ at all times [43]). In other words, for the potential landscape to be dominated by the trapping field and the field reflected from the mirror (instead of the field reflected by the membrane), enough power needs to reach the piezo-mirror, *i.e.*, the reflection coefficient of the membrane has to be small enough (if the transmission through the other optical elements has already been optimized). The 500 nm-thick membrane (used in the previous chapters) reflects 51%¹ of the power for normal incidence, which appeared to be too much for this application. This is the reason why we turned towards a 200 nm-thick membrane, which reflects only 2%¹ of the power (the smallest reflection coefficient available to us), allowing more power to go through the membrane and to be reflected on the piezo-mirror. We hope it will yield a value of D above threshold, enabling the well shifting.

¹This value is calculated for normal incidence and for a dielectric constant of SiN of 6.5.

5.4 Experimental tuning of d_{part} with a conveyor belt

In this section, we perform the tuning of d_{part} with the 200 nm-thick membrane. We start with the conveyor belt *switched off* by placing a beam block in front of the piezo-mirror. The 136 nm-diameter nanoparticle is trapped and discharged following the procedure described in Sec. 2.1.4. Then, the membrane approach protocol is conducted as described in Chap. 3 until the particle is in well 2 (monitored with the interferometric technique described in Chap. 4). Only then, the piezo-mirror is unblocked, *turning on* the conveyor belt. As long as no voltage is applied to the piezo-mirror, the potential wells are not shifting along z . We start simultaneously the recording of the back-focal-plane images allowing the measurement of d_{part} and the ramping

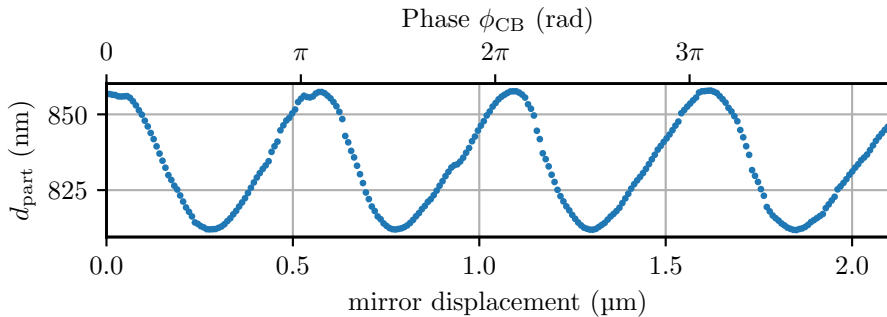


Figure 5.3: Distance d_{part} extracted from the analysis of the measured back-focal-plane images as a function of the mirror displacement and the phase ϕ_{CB} . The phase ϕ_{CB} change is proportional to the mirror displacement, which is proportional to the applied voltage on the piezoelectric actuator. The value d_{part} oscillates with a $\lambda/2$ periodicity around a mean value of 835 nm. According to our model, we are in the regime below threshold, where d_{part} cannot be continuously shifted because of lack of power in the conveyor belt beam.

of the voltage applied to the piezo-mirror. We show in Fig. 5.3 the value of d_{part} extracted from the back-focal-plane images as a function of the piezo-mirror displacement (which is linear with the applied voltage). We observe that d_{part} can indeed be tuned over a 50 nm range by changing the phase ϕ_{CB} (which is linear with the mirror displacement). However, we do not observe a linear shift of the distance d_{part} as expected in Fig. 5.2(b). Instead, we observe an oscillation of d_{part} (of periodicity $\lambda/2$, as expected) around a mean value, indicating that we are in the case represented on Fig. 5.2(c), below the power threshold. We conclude that, experimentally, $D < 0.3$, even with the 200 nm-thick membrane.

We notice that, in Fig. 5.3, the mean value d_{part} (≈ 835 nm) is different from the $1.04 \mu\text{m}$ measured in Chap. 4 although the particle is in well 2. This is because we use a thinner membrane in this chapter, and as we mentioned previously (see Sec. 4.2.2), the positions of the potential wells highly depend on the refractive index and the thickness of the membrane. The fact that we use an objective with a different NA might also play a role.

5.5 Conclusion

We have demonstrated a proof-of-principle of a conveyor belt system to tune the particle-to-surface distance d_{part} while the particle remains in the same well. Using this technique, we should be able to control and vary the distance d_{part} , which would no longer be determined solely by the standing-wave pattern created by the reflection from the membrane. Currently, we can vary d_{part} over 50 nm around 835 nm due to experimental limitations, namely power losses. To circumvent these issues, and benefit fully from the capability of the conveyor-belt system, we need to harvest a bigger fraction of the trapping power to be sent onto the actuated mirror. A suggestion is to use an anti-

reflection coated surface in order to reduce reflections from the surface to a minimum. Commercially available coatings can reach reflectivities of less than 0.1%, however, only for a limited range of small angles of incidence. In contrast, for our application, the coated surface is placed in the focus of a high-NA objective, where the incident light impinges on the surface with many different angles of incidence (up to 64° for the highest incidence angle when using an objective with $\text{NA}=0.9$). Moreover, most of the optical power resides in the high angles components of the field, angles for which the reflectivity is higher than for normal incidence. As a result, the total power reflected from an anti-reflection coated surface will typically not be below 1% in our configuration. Another way to circumvent these technical hurdles would be to replace the piezo-mirror with a plate beam splitter (90:10 R:T) mounted on a translation stage in the vacuum chamber, directly after the collection lens. Doing so would increase the power arriving at the piezo-mirror since there are no vacuum window or additional beam splitters for the light to traverse. Moreover, it would drastically reduce vibration-induced instabilities of the piezo-mirror, that impact directly on the optical potential. Additionally, we could replace the collection lens by an objective, to benefit from a better quality and confinement of the focus of the $\mathcal{E}_{\text{conv}}$ field. The best configuration would be a symmetric system, with the trapping and the collecting objectives being the same. This way, the two counter-propagating beams would overlap better.

Chapter 6

Towards sensing of surface forces

With our levitated nanoparticle at a subwavelength distance from a surface, we enter the range at which surface forces become measurable. Two well-known types of such forces are the Casimir and the Van der Waals force. As previously mentioned in Chap. 1, these forces originate from the existence of vacuum fluctuations, and the different names represent limiting cases for the expression of this attractive force. The name *Van der Waals forces* applies in the regime of atomic separations of a few nanometers at most, where retardation effects can be neglected [4]. The same attractive force is called *Casimir force* when the objects are further apart, which is the case in this thesis. The functional form of Casimir forces depends on the distance between the two bodies relative to their size, and on their shapes. The configuration that we use in this thesis is the sphere-plane configuration, with the levitated particle being the sphere and the dielectric membrane being the plane. If the separation between the sphere and the plane is smaller than the radius of the sphere (proximity force approximation), the

Casimir force is of the form [5, 19]

$$F_c = -\eta \frac{\hbar r c \pi^3}{360(d_{\text{part}} - r)^3}, \quad (6.1)$$

where r is the particle radius, d_{part} is the distance between the center of the sphere and the surface, and η is a dimensionless prefactor accounting for the fact that we do not have perfect conductors [79, 80]. However, if the separation between the sphere and the plane is larger than r , then the force takes the Casimir-Polder form [19]

$$F_{\text{cp}} = -\frac{3\hbar c \alpha}{8\pi^2 \epsilon_0} \frac{1}{d_{\text{part}}^5}. \quad (6.2)$$

Let's consider a sphere of radius 68 nm at 450 nm¹ from a SiN membrane, which are the parameters realized in the experiment discussed in Chaps. 3 and 4. The particle-to-surface distance is bigger than the radius of the sphere, therefore we are in the *large distance regime*, where the Eq. (6.2) should apply. Considering that we proposed in Chap. 5 a method to reduce the distance d_{part} to reach the regime where $d_{\text{part}} \approx r$, our experimental system may allow us to investigate the transition from the Casimir regime, described by Eq. (6.1), to the Casimir-Polder regime, described by Eq. (6.2).

Having discussed the length scales involved in a measurement of short-range forces using an optically levitated nanoparticle, let us turn to the force sensitivity required to carry out such a measurement. For $d_{\text{part}} = 450$ nm, we estimate $F_{\text{cp}} \approx 70$ aN. However, the particle is additionally subject to the optical forces that form the trap. For a particle in well 1, we estimate optical forces of the order of a few pN for typical oscillation amplitudes at room temperature, *i.e.*, 5 orders of magnitude larger than the Casimir force. The equilibrium

¹center-to-surface distance

position displacement induced by the Casimir force can be estimated to first order to be ≈ 0.5 nm. However, the measurement of such a displacement is impossible in our case for two main reasons. First, measuring a displacement requires to have a reference measurement, which would mean to measure the equilibrium position without the Casimir force, which is impossible because the surface creates the optical potential. There is no way of deactivating the Casimir force to realize a reference measurement. Second, this displacement is very small, which means we would need to measure for a long time to resolve it. Unfortunately, during this time, drifts would impact the detector signal more than the displacement we want to measure. Therefore, we can not expect to be able to detect surface forces while the particle is trapped. That is why we consider using a free-fall force-sensing scheme, based on Ref. [42, pp. 121ff.], that we detail in the following section.

6.1 A free-falling particle as a force sensor

Recent work within the Photonics group at ETH Zurich has shown the use of a free-falling particle as a very sensitive sensor for static forces [41]. In this section, we describe the underlying concept, depicted in Fig. 6.1. The particle is trapped and cooled to low-amplitude oscillations (a). At one instance of time, the trapping laser is *switched off*, so the particle is not subject to optical forces anymore (b). It can therefore interact with the remaining forces F , for example gravity (hence the name *free-fall*) or electric forces if the particle is charged. After a short time τ , the trap is *switched on* again, catching the particle that has been displaced by the static forces (c). This displacement results in a larger oscillation amplitude after the free-fall as compared to before. Measuring the oscillation amplitude allows us to retrieve the

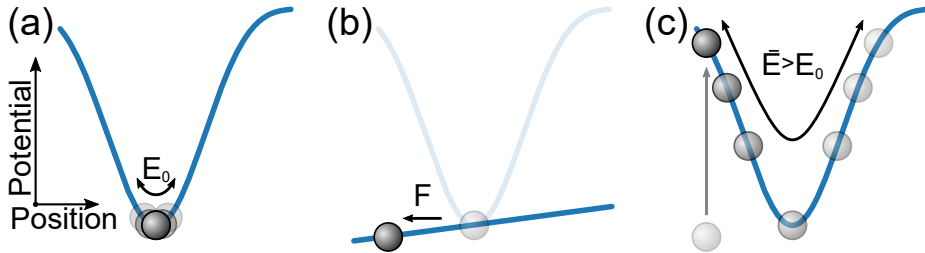


Figure 6.1: Principle of a force measurement with a free-falling particle. (a) A nanoparticle is levitated in an optical potential. The particle's COM motion has been cooled along the three oscillation axes. (b) The trapping laser is switched off, and the particle is subject to the remaining force F , resulting in a particle displacement along the direction of the force. (c) After a very short time, the laser is switched back on and the particle is recaptured in the optical potential. It oscillates with a larger amplitude than in (a) as it acquired potential energy during the fall in (b). The oscillation amplitude is related to the displacement acquired during the free-fall and therefore to the magnitude of the force F . Adapted with permission from Ref. [41].

displacement and therefore to deduce the force the particle has been subject to during the free-fall. A force sensitivity of 10 aN has been demonstrated, which is sufficient to detect the Casimir force acting on a particle residing in well 1² [41]. A crucial point in the free-fall experiments is the efficient cooling of the particle's center-of-mass (COM) motion before the free-fall, which we implement in the next section.

²Well 1 is the well closest to the membrane, as introduced in Sec. 3.3.

6.2 Feedback cooling the center-of-mass motion of a particle

As the particle is not standing still in the trap when the laser is switched off, it still has kinetic energy and therefore a finite velocity at the moment when it is released from the optical trap. The particle will therefore continue to move with this velocity during the fall duration τ and will be displaced. The larger the initial velocity, the larger the displacement. The displacement induced by the remaining velocity scales linearly with the fall duration τ , whereas the displacement due to the investigated force acting on the particle scales quadratically with the fall duration, as we will derive in the next section. Accordingly, a certain minimum fall duration is required for the displacement due to the force acting on the particle to overcome the displacement due to the initial velocity. Importantly, the overall displacement during the fall is limited by the finite size of our optical trap, since we have to recapture the particle after the fall. Therefore, we need to reduce the initial velocity of the particle to reduce its effect on the particle displacement. Only then, the displacement due to the investigated force becomes detectable within a fall duration compatible with the size of our trap.

After motivating the implementation of a cooling scheme for the particle's COM motion, we present in the following the experimental realization. We cool the COM motion using a parametric feedback scheme [27, 43]. The experimental setup is described in Fig. 6.2. In comparison to the setup used in Chaps. 3 and 4, an additional electro-optic modulator (EOM) has been placed after the laser to modulate the beam intensity. A phase-locked loop (PLL) is detecting the particle's oscillation frequency (and phase). We generate a second harmonic signal (with the appropriate phase) and feed this signal to the EOM. As a result, the intensity, *i.e.*, the trap stiffness, is modulated at twice the

6. TOWARDS SENSING OF SURFACE FORCES

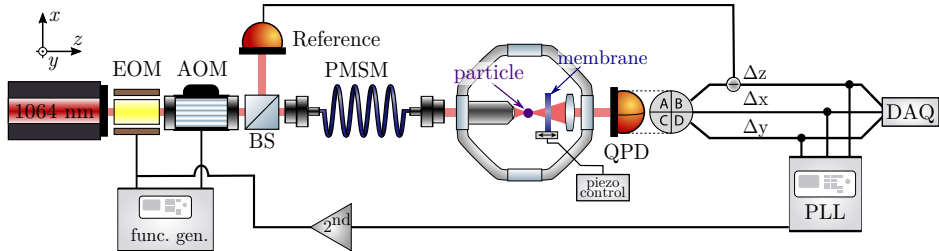


Figure 6.2: Experimental setup for the feedback cooling scheme and free-fall measurements. The electro-optic modulator (EOM) placed after the laser allows the intensity modulation that is necessary for feedback cooling the particle's COM motion. The phase locked loop (PLL) detector is tracking the particle oscillation frequencies, and the second harmonic signals are generated and fed into the EOM for the laser intensity modulation. An acousto-optic modulator (AOM) is added in series with the EOM to enable the high-contrast intensity modulation required for the free-fall. The laser beam can be switched off by simultaneously controlling the EOM and the AOM with function generators.

oscillation frequency³. We note that the trapping objective used in this chapter is an Olympus 100x (NA = 0.85, focal length $f = 1.8$ mm) [42, pp. 127f.].

After introducing the experimental setup necessary to perform feedback cooling of the particle's COM motion, we present some results. We place the discharged particle in well 1, we cool its COM motion, and we record, at 10^{-4} mbar, a 1 s-long time trace of the cooled particle position along z . From this calibrated time trace⁴, we calculate the PSD S_{zz} and plot it in Fig 6.3 in orange. For comparison, we plot in green the PSD of the uncooled particle at 1.5 mbar. To calculate the COM temperature, *i.e.*, the total energy E_{tot} of the particle, we

³The acousto-optic modulator (AOM) and the function generators (func. gen.) in Fig. 6.2 are not used for feedback cooling but will be utilized for the free-fall experiments described in the next section.

⁴The calibration is done following the procedure explained in Sec. 2.2.4.

6.2. Feedback cooling the center-of-mass motion of a particle

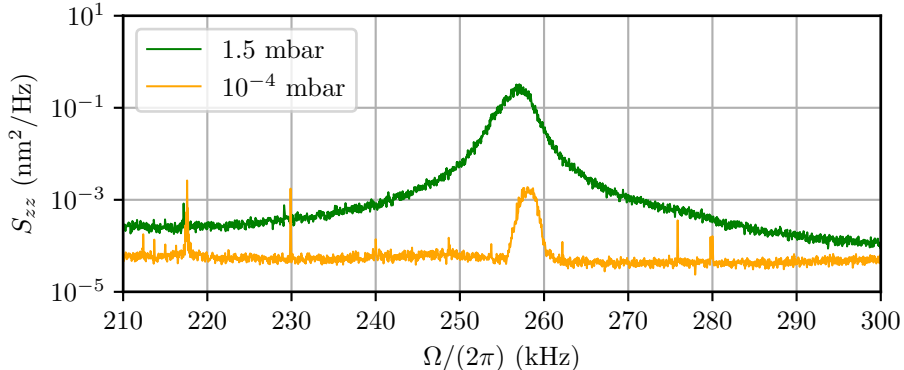


Figure 6.3: Power spectral density S_{zz} calculated from the time traces of the positions along z . The green PSD corresponds to an uncooled particle (1.5 mbar). The orange PSD corresponds to the particle cooled to 1 K (10^{-4} mbar). The particle's COM temperature is proportional to the area under the peak.

refer to Sec. 2.2.2, where we found for a harmonic oscillator, that $\langle E_{\text{pot}} \rangle = \frac{1}{2}k_{\text{B}}T = \langle E_{\text{kin}} \rangle$. Thus, the total energy is given by $\langle E_{\text{tot}} \rangle = \langle E_{\text{pot}} \rangle + \langle E_{\text{kin}} \rangle = k_{\text{B}}T = m\Omega_0^2 \langle q(t)^2 \rangle$. We have seen that $\langle q(t)^2 \rangle$ is the integrated area below the PSD. Accordingly, we calculate for this cooled particle a COM temperature of 1 K. We note that the peak of the cooled oscillator in Fig. 6.3 has a non-Lorentzian shape. This is due to frequency fluctuations that become significant whenever the oscillator is cooled close to the membrane. Indeed, at high pressures, the linewidth is dominated by the gas damping, whereas at low pressures, under feedback cooling, frequency fluctuations that may originate from the instability of the membrane, become apparent. During the 1 s-long acquisition, the z frequency of the particle fluctuates and the resulting peak in the PSD is an average over these frequency fluctuations.

6.3 Free-fall measurement without surface

Besides a low initial COM temperature, another key ingredient to controllably let a particle fall is a fast and high-contrast switching of the trapping beam. We want no transient regime to influence the particle motion, nor a residual trap induced by remaining intensity in the focus. To achieve such a high-contrast intensity ratio, we introduce an AOM (see Fig. 6.2) after the EOM as an additional intensity modulator. Similarly to Ref. [42, pp. 124f.], the EOM extinction ratio is 50:1 and the AOM on:off ratio reaches 30000:1. If both modulators are switched at the same time, we can obtain a power extinction ratio of $1.5 \times 10^6:1$. The modulators are controlled by two functions generators as depicted in Fig. 6.2. Additionally, we need a fast switching time of the beam for the particle to suddenly fall, and not to slowly equilibrate with transient optical potentials. Therefore, we need a switching time much faster than the oscillation period of the particle ($\approx 1 \mu\text{s}$). Experimentally, we measure a switching time below 100 ns [41].

The procedure for a free-fall measurement is sketched in Fig. 6.4(a). We first trap, discharge and cool the particle (both trap and feedback (FB) are on). At $t = 0$, we switch the trap and the feedback off, using the EOM and the AOM. The particle is freely falling for a duration τ , after which the trap is switched back on, but the feedback remains deactivated. The entire measurement cycle including preparation and readout lasts typically 90 ms. The neutrality of the particle during the measurement is crucial to avoid electrostatic forces to influence the particle displacement. We want the only force acting on the particle to be the force under investigation, which is gravity in this experiment, and a Casimir-type force in the future. To ensure the particle remains uncharged throughout the experiment, we have found it necessary to physically shield the pressure gauge with an aluminium sheet, as

6.3. Free-fall measurement without surface

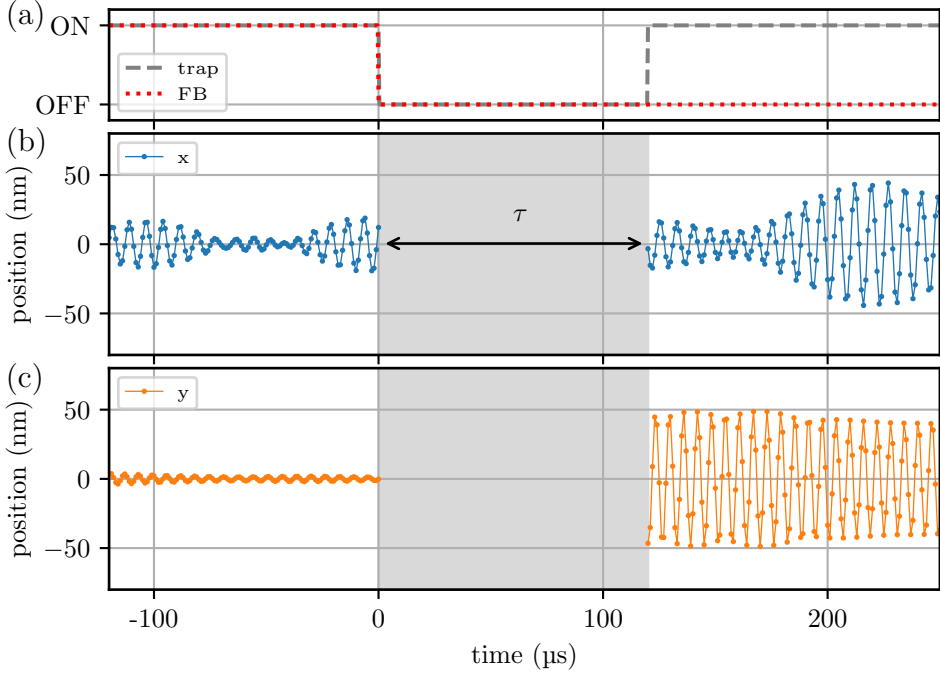


Figure 6.4: (a) Control signals for trap and feedback during a free-fall measurement. The system is initialized by feedback-cooling the motion of the particle levitated in the optical trap. Both the feedback and the trap are switched off at $t = 0$ for a duration τ ($120 \mu\text{s}$ in this example). At $t = \tau$, the trap is switched back on but the feedback remains deactivated. (b) Time trace of the particle position along x around the fall. For $t < 0$, the COM motion is cooled to 10 K. After a fall duration of $\tau = 120 \mu\text{s}$, the particle is caught again by the trap and oscillates with larger amplitudes than before the fall due to the displacement during the free evolution. (c) Time trace of the particle position along y around the fall. Similarly to (b), the particle is cooled to 3 K before the fall and oscillates with larger amplitude after the free-fall. The ratio between after/before oscillation amplitude is larger than for x , due to gravity acting in the y direction during the free-fall.

charged particles are emitted when the hot cathode sensor is on (see Sec. 2.1.3).

We record 90 ms-long times traces of the particle position along x and y for a fall duration of $\tau = 120 \mu\text{s}$ and show them in Fig. 6.4(b) and (c), respectively. In Fig. 6.4(b), before $t = 0$, the particle is cooled to 10 K and we therefore observe small oscillation amplitudes of less than 10 nm. At $t = 0$, the trapping laser is switched off, so we have no signal, *i.e.*, no scattering from the particle, during the fall duration τ . At $t = \tau$, the trap is switched back on, and the particle is trapped again. We observe now a higher oscillation amplitude than before the fall.

The time trace of the positions along y in Fig. 6.4(c) is very similar, with the particle initially cooled at 3 K. We observe that the difference in amplitude before and after the fall is bigger than for x . We attribute this finding to the fact that gravity acts along the y axis and therefore has displaced the particle during the fall in the y direction.

In order to verify that the effect we observed is due to the gravitational force, we investigate the evolution of the COM energy of the particle as a function of the fall duration. If we calculate the total energy of a particle, with initial position and velocity $(q_{\text{ini}}, \dot{q}_{\text{ini}})$, after a free evolution without external forces, we obtain

$$\begin{aligned} \langle E_{\text{tot}}^q \rangle (\tau) &= \langle E_{\text{pot}}^q \rangle + \langle E_{\text{kin}}^q \rangle + \langle E_{\text{pot,acquired}}^q \rangle \\ \langle E_{\text{tot}}^q \rangle (\tau) &= \frac{1}{2} m \Omega_0^2 \langle q_{\text{ini}}^2 \rangle + \frac{1}{2} m \langle \dot{q}_{\text{ini}}^2 \rangle + \frac{1}{2} m \Omega_0^2 \langle (\dot{q}_{\text{ini}} \tau)^2 \rangle \end{aligned} \quad (6.3)$$

with $\langle E_{\text{pot,acquired}}^q \rangle$ the potential energy acquired during the free evolution. The velocity stays invariant during a free evolution, so no kinetic energy was acquired. The displacement of the particle due to its initial velocity is $\dot{q}_{\text{ini}} \tau$, hence the expression for $\langle E_{\text{pot,acquired}}^q \rangle$. For a harmonic oscillator, we deduce for the total energy after the fall $\langle E_{\text{tot}}^q \rangle (\tau)$ [42,

p. 138]

$$\begin{aligned}\langle E_{\text{tot}}^q \rangle(\tau) &= k_{\text{B}}T + \frac{1}{2}m\Omega_0^2\tau^2 \langle \dot{q}_{\text{ini}}^2 \rangle \\ \langle E_{\text{tot}}^q \rangle(\tau) &= k_{\text{B}}T \left(1 + \frac{\Omega_0^2}{2}\tau^2 \right).\end{aligned}\tag{6.4}$$

We see that the total energy of the particle scales quadratically with the fall duration when no force is acting on the particle during the free evolution.

Now, if we assume that there is a static force F acting on the particle along the axis q ($q \in \{x, y, z\}$), we obtain for the total energy of the particle

$$\langle E_{\text{tot}}^q \rangle(\tau) = k_{\text{B}}T \left(1 + \frac{\Omega_0^2}{2}\tau^2 \right) + \frac{1}{2m}F^2\tau^2 \left(1 + \frac{1}{4}\Omega_0^2\tau^2 \right).\tag{6.5}$$

The presence of a static force results in a τ^4 scaling of the energy for long fall durations. The scaling of the particle energy with the fall duration can therefore indicate the presence or the absence of a force acting on the particle. We are aware that, as the Casimir force is distance dependent, the magnitude of the force will increase over time during the free fall. In this thesis, we consider, as a first approximation, the case where the force is minimal, *i.e.*, the largest separation between the particle and the surface, in order to check the feasibility of our experiment.

To experimentally measure the particle energy, we record time traces of the positions, similar to those shown in Fig. 6.4(b,c). We calculate the PSD from the time trace for $t > \tau$ and the variance of the position by integrating the PSD, as described by Eq. (2.15). We deduce the energy of the particle (expressed as a temperature) from the expression of the potential energy.

6. TOWARDS SENSING OF SURFACE FORCES

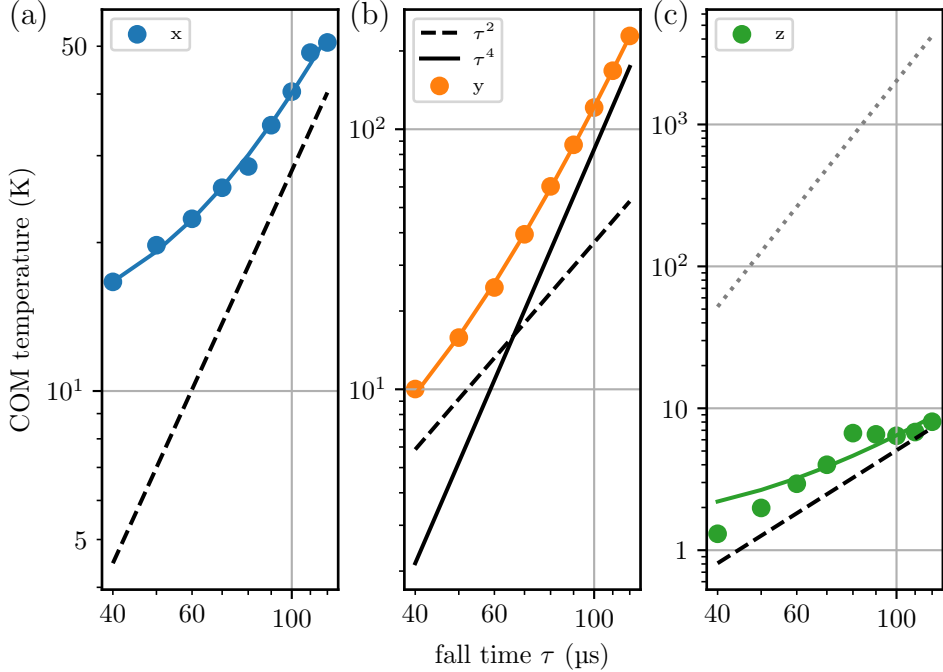


Figure 6.5: COM temperature as a function of fall durations τ . (a) For the x -mode, the evolution of the COM temperature (blue data) scales with τ^2 as shown by the fit (dashed line). The quadratic component is so small that it is not displayed on the graph (Initial COM temperature = 10 K). (b) For the y -mode, the COM temperature scales with τ^4 for large fall durations, as shown by the quartic fit (solid black line), revealing the existence of a force (gravity) acting along y during the free evolution of the particle (Initial COM temperature = 3 K). (c) Similarly to x , the COM temperature of the z -mode scales with τ^2 (dashed line), confirming the absence of a force acting along z (the particle has been cooled to 22 mK prior to free-fall). As a dotted line, we show the evolution of the total energy in the z -mode if Casimir forces would act on the particle. The amplitude assumed for the Casimir forces is 70 aN. We conclude that our sensitivity along z is good enough to detect such a force. The statistical error is smaller than the markers for all the data points. However, we note that a systematic error is observed, especially for the z axis. We assume it originates from drifts of the system over time but a further investigation would be required to confirm this hypothesis.

In order to account for the randomness of the initial conditions and get statistical results, we repeat the measurement cycle sketched in Fig. 6.4(a) a thousand times for each fall duration. We plot in Fig. 6.5 the results of these measurements, for fall durations from 40 μs to 120 μs , for x , y and z . These measurements were carried at a pressure of 2×10^{-6} mbar with an uncharged particle.

As we have theoretically derived the expected energy scaling with the fall duration, we fit the data with the sum of a quadratic (dashed black line) and a quartic (solid black line) function. For x and z (a,c), we observe a dependence of the energy with τ^2 , showing that no detectable force is acting on the particle along these axes. However, the evolution of the energy along the y axis (b) shows a τ^4 scaling for fall durations $\tau > 70 \mu\text{s}$. This is the signature of the presence of a static force, acting along the y axis, which corresponds to gravity. From the fitting coefficient, we calculate the magnitude of this force to be 4.3 aN, yielding a gravitational acceleration of 1.5 N/kg. We can attribute the discrepancy of the result to imprecisions on the calibration of the time traces [49] and to a possible overestimation of the particle mass. The particle mass is indeed omnipresent in all the calculations leading to the value of the measured force. Therefore a small error on the mass can have a big impact on the deduced force value.

6.4 Perspectives

We have shown our ability to detect a small static force such as gravity. We plot in Fig. 6.5(c) as a dotted line the expected scaling of the energy in the presence of a 70 aN static force (estimation of the Casimir force in well 1), that would act on the particle along the optical axis z . We can clearly detect such a force with the sensitivity of our measurement. The challenge is now to perform these 1000 repetitions of the free-fall close to the membrane (in well 1). Experimental difficulties arise from

the required long-term stability of the system regarding drifts and frequency noise. Indeed, reaching a pressure of $\approx 10^{-6}$ mbar starting at ambient conditions requires several hours, during which vibrations or drifts can affect the membrane. As the membrane creates the standing wave, the particle is closely coupled to the membrane motion, becoming much more sensitive to the environment than when being solely trapped in a standard optical trap. So far, a complete cycle of 1000 free-falls has not been successfully completed with the particle being in well 1.

In trying to identify the source of the instabilities, we analyzed the frequency stability of the oscillator and we present the results in the following. Indeed, the oscillation frequency is an indicator of the trap fluctuations. Moreover, frequency fluctuations affect the performance of the parametric feedback cooling. To characterize the frequency stability, we use a well-known technique, the Allan variance, also called two-sample variance. All the details of this method can be found in Refs [42, 81]. The Allan variance helps to identify noise types and to understand probable measurement limitations. The variance is calculated as the expectation value of the square of the difference between two consecutive values, following Eqs. (3.1) and (3.2) from Ref. [42]. We show in Fig. 6.6 the Allan deviation (the square root of the Allan variance) of the z -mode in the configuration “particle in well 1”. On the horizontal axis, the integration time \mathcal{T} corresponds to how long we measure the oscillator frequency. The red data points represent the frequency fluctuations of a particle in well 1 at 1×10^{-1} mbar. We observe for short integration times a decrease in frequency fluctuations the longer the measurement, which is an averaging effect. The slope is $\mathcal{T}^{-1/2}$ as indicated by the dashed line in Fig. 6.6 and characterizes white noise [81]. We find the optimum measurement time to be ≈ 10 s. For longer integration time, the Allan deviation increases again due to slow drifts in the system. The error bars on the Allan deviation have been calculated according to Eq. (3.3) of Ref. [42]. The black data points correspond to the particle in well 1

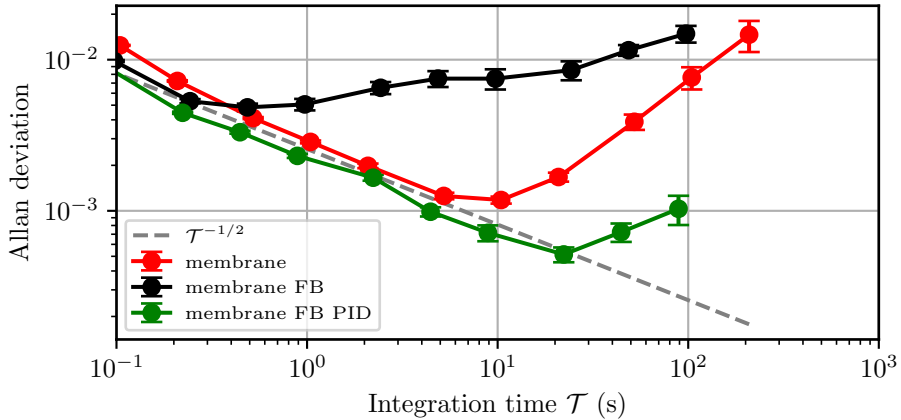


Figure 6.6: Allan deviation of the oscillation frequency Ω_z for a particle in well 1. The red data is measured at 10^{-1} mbar. The black data is recorded at 10^{-4} mbar with the feedback cooling activated. The optimum measurement time has drastically decreased compared to high pressures (red). Drifts have a more significant impact. The green data was measured in the same conditions as the black (pressure range and feedback cooling), but a PID loop was additionally controlling the membrane position, locked on Ω_z . The long term drifts can be eliminated by using the PID loop, therefore increasing the optimum measurement time. We note that the white noise, scaling with $\mathcal{T}^{-1/2}$ (dashed line), is similar in the three configurations.

at a pressure of 2×10^{-4} mbar, with the feedback cooling activated. We see that the optimum measurement time decreased drastically to below 1 s compared to high pressures, and that drifts become significant earlier at low pressures. The white noise contribution is similar than in the high pressure case. In order to reduce the drifts that could be the reason for the instability at low pressures, we set up a PID loop that corrects the membrane position along the optical axis z as a function of the oscillation frequency Ω_z . We plot in Fig. 6.6, as green data points, the Allan deviation for similar conditions than for the black data points but with the PID loop activated. We observe that

the drifts are indeed reduced, and that the optimal measurement time increased to 20 s. However, the correction for drifts was not enough to make the free-fall measurements close to the interface possible. We still need to investigate further what causes the instability of the system. If the source cannot be found and eliminated, technical alternatives are considered, such as an anti-reflection coated surface to replace the membrane. We hope to reduce drastically the influence of the membrane on the trapping potential and therefore efficiently decouple the particle from the membrane vibrations. This however constitutes a new approach to the positioning of the levitated particle close to a surface, which does not involve a standing wave.

Chapter 7

Outlook

Throughout this thesis, we have developed, characterized, and understood a protocol that enables the precise positioning of an optically levitated nanoparticle in close proximity to an interface. The configuration implemented in this work can be utilized for studies involving microscale effects. In Chap. 6, we have suggested to use the levitated particle as a sensor for short-range forces, such as Casimir forces, and we have demonstrated the feasibility of such a measurement with our experimental setup. Besides, our system offers other applications and we would like to mention in this last chapter three additional uses of the proximity of a levitated particle to a surface. The first one aims at integrating optically levitated objects into photonic circuits by coupling the motion of this object to an electromagnetic field which is guided in the photonic circuit. The second application turns towards thermodynamic studies at the micro- and nanoscale [82], where we envision to investigate the radiative heat transfer between a nanoparticle and a surface [83]. Finally, the third study focuses on the measurement of rotational friction in vacuum [84].

7.1 Integrating optical traps on a chip

We have considered in this thesis a standard optical trapping setup with a free space laser. Nevertheless, with the ongoing miniaturization of technologies, we might want to consider also miniaturizing and integrating optical traps into more complex and multitasking structures such as integrated photonic circuits. Levitation has emerged as a precious tool for the development of inertial sensors [85, 86, 87, 88]. The development of more sensitive and more stable inertial sensors has exponentially increased during the last decades, especially for navigation systems (smartphones, automobiles) [89]. Using levitated sensors, the sensitivity is no longer limited by mechanical losses due to clamping [90].

If we want to integrate optical levitation into chips, the challenge is to replace the external trapping laser by a trapping field generated in optical resonators on the chip. The intensity gradients necessary for particle trapping, as we have seen in Chap. 2, can be realized by coupling the levitated particle to a field confined in a resonator. The self-induced back-action (SIBA) effect, where the particle motion couples to the intra-resonator trapping field [91], has been used to develop such traps. The most common optical resonators used for on-chip trapping are plasmonic structures and photonic crystals [92, 93, 94, 95, 96]. Since these traps are relying on the optical near field (the SIBA effect scales with the mode volume overlap between the particle and the resonator), the particle needs to be in very close proximity to the structure in order to interact maximally with the field in the resonator. Therefore, in most configurations, we want the particle to be trapped just above the structure. At these short separations, surface forces will have a significant effect on the particle, as we have shown in Chap. 6. Therefore, we think that the tool we developed can be used to measure these surface forces due to the proximity of the structure, and gain a deeper understanding of the forces competing in the trapping

region. Realizing such on-chip optical traps has several advantages. The input power in these trapping structures can be drastically reduced compared to free-space trapping due the enhancement factor of the resonators. Moreover, specifically engineered structures could allow specific shaping of the trapping potential, offering more versatility than the standard focus of a laser beam. Those improvements could bring optical traps even closer to industrial applications.

7.2 Radiative heat transfer at the microscale

The second application we suggest, using the configuration of a levitated nanoparticle at subwavelength distance from an interface, is the study of radiative heat transfer.

Levitated nanoparticles have an internal temperature, that can be measured and controlled [63, 64]. We have developed the positioning of a levitated particle close to a surface. If the particle and the surface have different temperatures, there will be a heat exchange between the two bodies. This heat transfer is characterized by the thermal wavelength λ_{thermal} . With our particle placed at a submicron distance from the surface, we are in the regime where the separation between the two bodies is smaller than the thermal wavelength (in our case, we estimate $\lambda_{\text{thermal}} = \hbar c / (k_{\text{B}} T) \approx 2 \mu\text{m}$ assuming a particle internal temperature around 1000 K [42, 97]). In this regime, the radiative heat transfer is supported by evanescent fields, which do not contribute to the far-field radiation. Therefore, in the near-field regime, heat transfer rates can be enhanced [97, 98, 99, 100, 101, 102]. Levitated nanoparticles seem a very suitable system for the study of thermodynamics at the microscopic scale [82, 97, 103]. Indeed, they offer the advantage of a simple sphere/plane geometry (perfect sphere

7. OUTLOOK

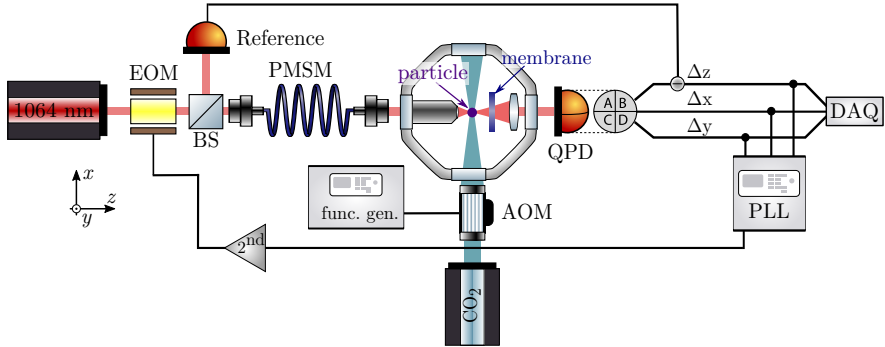


Figure 7.1: Experimental setup suited to perform a relaxation measurement, inspired by Ref [63]. The optical trapping setup presented in previous chapters remains unchanged. We add a CO_2 laser ($\lambda_{\text{CO}_2} = 10.6 \mu\text{m}$) weakly focused on the particle. This additional laser does not affect the trap [42, p. 98] but increases the internal temperature of the nanoparticle due to high absorption of silica at a wavelength of $10.6 \mu\text{m}$ [52]. An AOM, controlled by a function generator, is used to switch on and off the heating beam.

compared to scanning probes) and of a very good isolation from the environment (no clamping to external structures, that would introduce an additional heat transfer channel). Studying thermal exchange in the near-field regime opens up routes for several applications such as thermophotovoltaics or heat-assisted magnetic recording [104, 105, 106, 107, 108, 109, 110, 111].

In the following, we explain a measurement principle that would allow us to measure the heat transfer between the levitated particle and the SiN membrane. Based on the theory developed in Refs. [83, 102], we suggest to measure the time the internal temperature of the particle needs to equilibrate back to the gas temperature after being heated for a short time. This time is called the thermal relaxation time of the levitated particle. The thermal relaxation time is expected to vary periodically with the separation between the two objects [83]. The

goal is therefore to measure the dependence of the thermal relaxation time as a function of the particle-to-surface distance, as calculated in Fig. 2 of Ref. [83]. To this end, we would perform an experiment similar to the one from Ref. [63] where the internal temperature of the particle is increased by weakly focusing a CO₂ laser on the particle for a short time. We then measure the time it needs to equilibrate back to the bath temperature (see Fig. 5.2 in Ref. [42]).

Figure 7.1 shows the experimental setup for such a measurement. A CO₂ laser is used to heat the particle because silica has a high absorption at this laser wavelength ($\lambda_{\text{CO}_2} = 10.6 \mu\text{m}$) [52]. The rest of the setup is identical to the one used in this thesis. For the measurement, the particle is placed in a specific well (following the protocol described in Chap. 3) and feedback cooled to a few K. At $t = 0$, the CO₂ laser is switched on for 1 s using the AOM as an amplitude modulator, similarly to Chap. 6. The CO₂ laser pulse heats the internal temperature of the particle, due to the strong absorptivity of silica at this wavelength. The particle's internal temperature can be directly monitored via the oscillation frequency in the trap, as the material properties are temperature dependent [63]. Therefore, by recording the time evolution of the particle's oscillation, we can deduce the time evolution of the internal temperature of the particle. We can therefore measure the internal temperature cooling rate from the exponential decay of the oscillation frequency, after the CO₂ laser has been switched off. Repeating this measurement for different particle-to-surface distances would enable to provide an experimental evolution of the radiative heat transfer as a function of distance. Nevertheless, we will undoubtedly face technical challenges. The first one is that we have to ensure that the CO₂ laser does not heat the surface because we need a temperature gradient between the particle and the surface. Therefore, we propose to turn towards a ZnSe surface [112], due to a very low absorption of ZnSe around 10 μm (and also at 1064 nm). Secondly, we need to ensure that the cooling rate due to the surface is significant compared to the other

dissipation channels. Indeed, at pressures higher than 10^{-3} mbar, the convective dissipation of energy via the gas [46] dominates over black body radiation (see Fig 5.7(a) in Ref. [42]). As we want to observe the influence of the surface on the black body radiation of the particle, we need to operate below 10^{-3} mbar.

7.3 Vacuum friction

If we consider two neutral objects, one being translational invariant like a plane, that move relative and parallel to each other, they are subject to a dissipative force, even though they are not in contact. This force is called vacuum friction [57, 84, 113, 114]. This non-conservative force originates from thermal fluctuations of the polarization. In dissipative materials (where the imaginary part of the dielectric constant is non-zero), the fluctuation-dissipation theorem leads to a fluctuation of the polarization in the material. If the two objects are in relative motion, then the image charges induced on the opposite surface will lag behind and tend to pull back the fluctuating charges. To be able to observe such a phenomenon, we need two objects in parallel relative motion, very close to each other, because the friction force scales strongly with the separation distance [113]. Let's consider the configuration we have implemented in this thesis, *i.e.*, a levitated particle at submicron distance from a surface.

We see two opportunities in using this system for the purpose of observing vacuum friction. The first one relies on the motion of the trapped particle transverse to the optical axis (*i.e.*, along x and y). The particle should experience the vacuum friction force when oscillating very close to the surface. We speculate that we should be able to observe the additional damping due to this friction force by measuring the width of the oscillation peaks for x and y in the PSD, since this width is related to the damping, as explained in Sec. 2.2.2. We expect

to witness a broader peak when the particle is close to the surface compared to when it is levitating in free space. However, non-linearities and frequency fluctuations might be experimental hurdles.

The second configuration we propose is a rotating particle in close proximity to a surface. Indeed, we have recently demonstrated that levitated nanoparticles in vacuum can be rotated, even up to 1 GHz rotation frequency [115, 116, 117]. The rotation of the nanoparticle is triggered by shining a circularly polarized light onto it, which can be experimentally realized by adding a quarter-wave plate in the beam path before the trapping objective. Due to its rotation, the particle should also experience vacuum friction, and the steady state angular velocity should decrease when the particle is close to a surface compared to when it is in free space. Therefore, by combining both the abilities to bring the particle very close to a surface and to rotate this particle, we could potentially offer a configuration where the investigation of vacuum friction can be undertaken.

List of Symbols

(x, y, z)	Cartesian coordinates
(ρ, θ, ϕ)	spherical coordinates
$\alpha = \alpha' + i\alpha''$	particle polarisability
α_{eff}	effective particle polarizability
$\epsilon(\omega)$	complex relative permittivity of the particle
ϵ_0	vacuum dielectric constant
$\epsilon_m(\omega)$	relative permittivity of the surrounding medium
$\eta(z)$	Gouy phase
γ	damping rate
λ	wavelength of light in vacuum
\mathcal{T}	time length of a time trace of the particle position
\mathcal{V}	particle volume
k	trap stiffness
μ_0	vacuum permeability
ω	optical angular frequency
ω_{cap}	frequency of the alternating voltage applied to the capacitor

LIST OF SYMBOLS

Ω_q	mechanical angular frequency along direction i
τ	fall duration
\mathcal{E}	electric field
\mathbf{p}	dipole moment
\mathbf{q}	particle position
c	speed of light
c_{calib}	calibration factor
d_{foc}	focus-to-surface distance
d_{part}	particle-to-surface distance
E	energy
f	focal length
I	intensity
$k = 2\pi/\lambda$	wavenumber in vacuum
k_{B}	Boltzmann constant
m	nominal particle mass
P	power
Q	charge of the particle
r	particle radius
$r_{1,2}^{(\text{p,s})}$	reflection Fresnel coefficient for the interface between two semi-infinite media 1 and 2

$r_{\text{slab}}^{(p,s)}$	reflection Fresnel coefficients for a dielectric slab with finite thickness
S_{qq}	double-sided power spectral density of variable q in angular frequency
T	temperature
t_{mbn}	membrane thickness
U	optical potential
V	voltage
$w_{x,y,z}$	beam waist along the direction x , y or z
z_0	Rayleigh length

List of Figures

2.1	Schematic of the basic optical trapping setup with the charge control system	9
2.2	Time trace of the particle position and power spectral density	11
2.3	Discharging the particle	14
2.4	Focusing a Gaussian beam, schematic and intensity in the focal plane	18
2.5	Optical potential of a strongly focused beam	20
2.6	Quadrant photodetector	27
2.7	Calibration of the particle signal	29
3.1	Experimental setup with a membrane behind the particle .	33
3.2	Relevant geometrical parameters (not to scale) in the configuration with the membrane of thickness t_{mbn}	34
3.3	Voltage recorded on the photodetector PD1 as the membrane position is swept across the focus towards the objective	36
3.4	PSD of the particle position along z as a function of the distance focus-to-surface d_{foc} and corresponding reconstructed optical potentials	38
3.5	Intensity distribution for $d_{foc} = 40 \mu\text{m}$	42
3.6	Calculated optical potential for $d_{foc} \approx 40 \mu\text{m}$	44
3.7	Simulation of the particle oscillations along z for a membrane approach from $41 \mu\text{m}$ to $39 \mu\text{m}$	47
3.8	Measured power spectral density of the particle motion for decreasing focus-to-surface distances d_{foc} , recorded on the z detector	49

LIST OF FIGURES

3.9	Time trace of the particle position along the z axis around $d_{\text{foc}} = 1.924 \mu\text{m}$	51
3.10	Measured power spectral density of the particle motion for decreasing focus-to-surface distances d_{foc} , recorded on the z detector, for a different measurement than in Fig. 3.8	52
3.11	Reconstructed optical potential along the z axis for $d_{\text{foc}} = 390 \text{ nm}$	54
3.12	Calculated intensity distribution for $d_{\text{foc}} = 500 \text{ nm}$ and corresponding calculated optical potential landscape	56
3.13	Evolution of the calculated potential landscape around the focal region as we vary d_{foc}	57
3.14	Calculated oscillation frequency Ω_z as a function of focus-to-surface distance d_{foc} for the first six wells	58
3.15	Sketches of the optical potential along the optical axis as the membrane is moved towards the focal plane, illustrating the transition of the particle from well 4 to well 3.	60
4.1	Experimental setup with the addition of a green laser for the interferometric measurement of d_{part}	67
4.2	Measured back-focal-plane image for $d_{\text{foc}} \approx 4.2 \mu\text{m}$ and geometry of the interferometric measurements	68
4.3	Calculated back-focal-plane intensity distribution, using the parameters from Tab. 4.1, $d_{\text{part}} = 3 \mu\text{m}$ and $t_{\text{mbn}} = 500 \text{ nm}$	71
4.4	Back-focal-plane imaging of a nanoparticle levitated in front of a SiN membrane	73
4.5	Values of d_{part} extracted from the fit of the measured back-focal-plane images as a function of d_{foc}	76
4.6	Effect of the Gouy phase on the optical potential	78
5.1	Experimental setup allowing for a shift of the potential wells along the optical axis	83

5.2	Calculated optical potential along z for $d_{\text{foc}} = 0$ as a function of ϕ_{CB} and D	85
5.3	Distance d_{part} extracted from the analysis of the measured back-focal-plane images as a function of the mirror displacement and the phase ϕ_{CB}	87
6.1	Principle of a force measurement with a free-falling particle [41]	94
6.2	Experimental setup for the feedback cooling scheme and free-fall measurements	96
6.3	Power spectral density S_{zz} with and without feedback cooling	97
6.4	Free-fall measurement cycle and time traces for x and y before and after the free-fall	99
6.5	COM temperature as a function of fall durations τ	102
6.6	Allan deviation of the oscillation frequency Ω_z for a particle in well 1	105
7.1	Experimental setup to study radiative heat transfer	110

References

- [1] G. E. Moore. “Cramming more components onto integrated circuits”. *Proc. IEEE* 86 (1), p. 82, 1998.
- [2] C. Quigg. “Elementary Particles and Forces”. *Sci. Amer.* 252 (4), p. 84, 1985.
- [3] D. J. Griffiths. *Introduction to Elementary Particles*. Wiley-VCH, 2004.
- [4] G. L. Klimchitskaya, U. Mohideen, and V. M. Mostepanenko. “The Casimir force between real materials: Experiment and theory”. *Rev. Mod. Phys.* 81 (4), p. 1827, 2009.
- [5] H. Casimir. “On the attraction between two perfectly conducting plates”. *Proc. K. Ned. Akad.* 360, p. 793, 1948.
- [6] J. Bárcenas, L. Reyes, and R. Esquivel-Sirvent. “Scaling of micro- and nanodevices actuated by Casimir forces”. *Appl. Phys. Lett.* 87 (26), p. 263106, 2005.
- [7] J. N. Ding, S. Z. Wen, and Y. G. Meng. “Theoretical study of the sticking of a membrane strip in MEMS under the Casimir effect”. *J. Micromech. Microeng.* 11 (3), p. 202, 2001.
- [8] F. M. Serry, D. Walliser, and G. J. Maclay. “The role of the Casimir effect in the static deflection and stiction of membrane strips in microelectromechanical systems (MEMS)”. *J. Appl. Phys.* 84 (5), p. 2501, 1998.
- [9] A. Almasi, P. Brax, D. Iannuzzi, and R. I. Sedmik. “Force sensor for chameleon and Casimir force experiments with parallel-plate configuration”. *Phys. Rev. D* 91 (10), p. 102002, 2015.

REFERENCES

- [10] U. Mohideen and A. Roy. “Precision Measurement of the Casimir Force from 0.1 to 0.9 μm ”. *Phys. Rev. Lett.* 81 (21), p. 4549, 1998.
- [11] J. L. Garrett, D. A. T. Somers, and J. N. Munday. “Measurement of the Casimir Force between Two Spheres”. *Phys. Rev. Lett.* 120 (4), p. 040401, 2018.
- [12] B. W. Harris, F. Chen, and U. Mohideen. “Precision measurement of the Casimir force using gold surfaces”. *Phys. Rev. A* 62 (5), p. 052109, 2000.
- [13] R. S. Decca, D. López, E. Fischbach, and D. E. Krause. “Measurement of the Casimir Force between Dissimilar Metals”. *Phys. Rev. Lett.* 91 (5), p. 3, 2003.
- [14] Y. Bao, R. Guérout, J. Lussange, A. Lambrecht, R. A. Cirelli, F. Klemens, W. M. Mansfield, C. S. Pai, and H. B. Chan. “Casimir force on a surface with shallow nanoscale corrugations: Geometry and finite conductivity effects”. *Phys. Rev. Lett.* 105 (25), p. 250402, 2010.
- [15] A. O. Sushkov, W. J. Kim, D. A. R. Dalvit, and S. K. Lamoreaux. “Observation of the thermal Casimir force”. *Nat. Phys.* 7 (3), p. 230, 2011.
- [16] A. Landragin, J. Y. Courtois, G. Labeyrie, N. Vansteenkiste, C. I. Westbrook, and A. Aspect. “Measurement of the van der Waals Force in an Atomic Mirror”. *Phys. Rev. Lett.* 77 (8), p. 1464, 1996.
- [17] J. M. Obrecht, R. J. Wild, M. Antezza, L. P. Pitaevskii, S. Stringari, and E. A. Cornell. “Measurement of the temperature dependence of the casimir-polder force”. *Phys. Rev. Lett.* 98 (6), p. 063201, 2007.

-
- [18] A. Anderson, S. Haroche, E. A. Hinds, W. Jhe, and D. Meschede. “Measuring the van der Waals forces between a Rydberg atom and a metallic surface”. *Phys. Rev. A* 37 (9), p. 3594, 1988.
- [19] A. A. Geraci, S. B. Papp, and J. Kitching. “Short-Range Force Detection Using Optically Cooled Levitated Microspheres”. *Phys. Rev. Lett.* 105 (10), p. 101101, 2010.
- [20] A. Ashkin. “Acceleration and Trapping of Particles by Radiation Pressure”. *Phys. Rev. Lett.* 24 (4), p. 156, 1970.
- [21] A. Ashkin, J. M. Dziedzic, J. E. Bjorkholm, and S. Chu. “Observation of a single-beam gradient force optical trap for dielectric particles”. *Opt. Lett.* 11 (5), p. 288, 1986.
- [22] Y. Tsaturyan, A. Barg, E. S. Polzik, and A. Schliesser. “Ultrasound nanomechanical resonators via soft clamping and dissipation dilution”. *Nat. Nanotechnol.* 12 (8), p. 776, 2017.
- [23] M. D. Wang, H. Yin, R. Landick, J. Gelles, and S. M. Block. “Stretching DNA with optical tweezers”. *Biophys. J.* 72 (3), p. 1335, 1997.
- [24] S. M. Block, L. S. B. Goldstein, and B. J. Schnapp. “Bead movement by single kinesin molecules studied with optical tweezers”. *Nature* 348 (6299), p. 348, 1990.
- [25] A. Grant. “Ashkin, Mourou, and Strickland share 2018 Nobel Prize in Physics”. *Phys. Today* 2018.
- [26] A. Ashkin and J. M. Dziedzic. “Optical levitation in high vacuum”. *Appl. Phys. Lett.* 28 (6), p. 333, 1976.
- [27] J. Gieseler, B. Deutsch, R. Quidant, and L. Novotny. “Subkelvin Parametric Feedback Cooling of a Laser-Trapped Nanoparticle”. *Phys. Rev. Lett.* 109 (10), p. 103603, 2012.

REFERENCES

- [28] V. Jain, J. Gieseler, C. Moritz, C. Dellago, R. Quidant, and L. Novotny. “Direct Measurement of Photon Recoil from a Levitated Nanoparticle”. *Phys. Rev. Lett.* 116 (24), p. 243601, 2016.
- [29] A. Pontin, P. F. Barker, and N. P. Bullier. “Millikelvin cooling of the center-of-mass motion of a levitated nanoparticle”. In: *Optical Trapping and Optical Micromanipulation XIV*. Ed. by K. Dholakia and G. C. Spalding. SPIE, 2017, p. 56.
- [30] M. Aspelmeyer, T. J. Kippenberg, and F. Marquardt. “Cavity optomechanics”. *Rev. Mod. Phys.* 86 (4), p. 1391, 2014.
- [31] Z.-Q. Yin, A. Geraci, and T. Li. “Optomechanics of levitated dielectric particles”. *Int. J. Mod. Phys. B* 27 (26), p. 1330018, 2013.
- [32] M. Armano and *et al.* “Sub-Femto-g Free Fall for Space-Based Gravitational Wave Observatories: LISA Pathfinder Results”. *Phys. Rev. Lett.* 116 (23), p. 231101, 2016.
- [33] D. Hempston, J. Vovrosh, M. Toroš, G. Winstone, M. Rashid, and H. Ulbricht. “Force sensing with an optically levitated charged nanoparticle”. *Appl. Phys. Lett.* 111 (13), p. 133111, 2017.
- [34] F. Monteiro, S. Ghosh, A. G. Fine, and D. C. Moore. “Optical levitation of 10-ng spheres with nano-g acceleration sensitivity”. *Phys. Rev. A* 96 (6), p. 063841, 2017.
- [35] A. Arvanitaki and A. A. Geraci. “Detecting High-Frequency Gravitational Waves with Optically Levitated Sensors”. *Phys. Rev. Lett.* 110 (7), p. 071105, 2013.
- [36] G. Ranjit, M. Cunningham, K. Casey, and A. A. Geraci. “Zep-tonewton force sensing with nanospheres in an optical lattice”. *Phys. Rev. A* 93 (5), p. 053801, 2016.

-
- [37] A. Jonáš, P. Zemánek, and E.-L. Florin. “Single-beam trapping in front of reflective surfaces”. *Opt. Lett.* 26 (19), p. 1466, 2001.
- [38] R. S. Dutra, P. A. M. Neto, H. M. Nussenzveig, and H. Flyvbjerg. “Theory of optical-tweezers forces near a plane interface”. *Phys. Rev. A* 94 (5), p. 053848, 2016.
- [39] Z. Xu and T. Li. “Detecting Casimir torque with an optically levitated nanorod”. *Phys. Rev. A* 96 (3), p. 033843, 2017.
- [40] G. Winstone, M. Rademacher, R. Bennett, S. Buhmann, and H. Ulbricht. “Direct measurement of short-range forces with a levitated nanoparticle”. *arXiv 1712.01426* 2017.
- [41] E. Hebestreit, M. Frimmer, R. Reimann, and L. Novotny. “Sensing Static Forces with Free-Falling Nanoparticles”. *Phys. Rev. Lett.* 121 (6), p. 063602, 2018.
- [42] E. Hebestreit. “Thermal Properties of Levitated Nanoparticles”. PhD thesis. ETH Zurich, 2017.
- [43] J. Gieseler. “Dynamics of Optically Levitated Nanoparticles in High Vacuum”. PhD thesis. ICFO Barcelona, 2014.
- [44] V. Jain. “Levitated Optomechanics at the Photon Recoil Limit”. PhD thesis. ETH Zurich, 2017.
- [45] L. Rondin, J. Gieseler, F. Ricci, R. Quidant, C. Dellago, and L. Novotny. “Direct measurement of Kramers turnover with a levitated nanoparticle”. *Nat. Nanotechnol.* 12 (12), p. 1130, 2017.
- [46] D. E. Chang, C. A. Regal, S. B. Papp, D. J. Wilson, J. Ye, O. Painter, H. J. Kimble, and P. Zoller. “Cavity opto-mechanics using an optically levitated nanosphere”. *PNAS* 107 (3), p. 1005, 2010.

REFERENCES

- [47] N. Kiesel, F. Blaser, U. Delic, D. Grass, R. Kaltenbaek, and M. Aspelmeyer. “Cavity cooling of an optically levitated submicron particle”. *PNAS* 110 (35), p. 14180, 2013.
- [48] T. Li, S. Kheifets, and M. G. Raizen. “Millikelvin cooling of an optically trapped microsphere in vacuum”. *Nat. Phys.* 7 (7), p. 527, 2011.
- [49] E. Hebestreit, M. Frimmer, R. Reimann, C. Dellago, F. Ricci, and L. Novotny. “Calibration and energy measurement of optically levitated nanoparticle sensors”. *Rev. Sci. Instrum.* 89 (3) 2018.
- [50] M. E. Gehm, K. M. O’Hara, T. A. Savard, and J. E. Thomas. “Dynamics of noise-induced heating in atom traps”. *Phys. Rev. A* 58 (5), p. 3914, 1998.
- [51] M. Khudaverdyan. “A controlled one and two atom-cavity system”. PhD thesis. Rheinische Friedrich-Wilhelms-Universität Bonn, 2009.
- [52] R. Kitamura, L. Pilon, and M. Jonasz. “Optical constants of silica glass from extreme ultraviolet to far infrared at near room temperature”. *Appl. Opt.* 46 (33), p. 8118, 2007.
- [53] *Thyracont Vacuum Instruments*. URL: <https://thyracont-vacuum.com/products/smartline-vacuum-transducers/vsh-smartline-vacuum-transducer/vsh8xd1-smartline-vacuum-transducer-with-lcd-display/>.
- [54] T. Sugimoto. *Fine Particles: Synthesis, Characterization, and Mechanisms of Growth*. Surfactant Science. Taylor & Francis, 2000.
- [55] M. Brownnutt, M. Kumph, P. Rabl, and R. Blatt. “Ion-trap measurements of electric-field noise near surfaces”. *Rev. Mod. Phys.* 87 (4), p. 1419, 2015.

-
- [56] M. Frimmer, K. Luszcz, S. Ferreiro, V. Jain, E. Hebestreit, and L. Novotny. “Controlling the net charge on a nanoparticle optically levitated in vacuum”. *Phys. Rev. A* 95 (6), p. 061801, 2017.
- [57] L. Novotny and B. Hecht. *Principles of Nano-Optics*. 2nd ed. Cambridge University Press, 2006.
- [58] C. Bohren and D. Huffman. *Absorption and Scattering of Light by Small Particles*. Wiley-VCH Verlag GmbH, 1998.
- [59] H. B. Callen and T. A. Welton. “Irreversibility and generalized noise”. *Phys. Rev.* 83 (1), p. 34, 1951.
- [60] C. Langevin and D. Huffman. *Sur la theorie du mouvement brownien*. Vol. 146. 1908.
- [61] F. Marquardt. *Quantum-optical phenomena in nanophysics. Fluctuation spectra*. 2010. URL: <https://www.video.uni-erlangen.de/clip/id/946.html>.
- [62] A. A. Clerk, M. H. Devoret, S. M. Girvin, F. Marquardt, and R. J. Schoelkopf. “Introduction to quantum noise, measurement, and amplification”. *Rev. Mod. Phys.* 82, p. 1155, 2010.
- [63] E. Hebestreit, R. Reimann, M. Frimmer, and L. Novotny. “Measuring the internal temperature of a levitated nanoparticle in high vacuum”. *Phys. Rev. A* 97 (4), p. 43803, 2018.
- [64] J. Millen, T. Deesuwana, P. Barker, and J. Anders. “Nanoscale temperature measurements using non-equilibrium Brownian dynamics of a levitated nanosphere”. *Nat. Nanotechnol.* 9 (6), p. 425, 2014.
- [65] C. Tischer, S. Altmann, S. Fišinger, J. K. Hörber, E. H. Stelzer, and E. L. Florin. “Three-dimensional thermal noise imaging”. *Appl. Phys. Lett.* 79 (23), p. 3878, 2001.

- [66] R. Diehl, E. Hebestreit, R. Reimann, F. Tebbenjohanns, M. Frimmer, and L. Novotny. “Optical levitation and feedback cooling of a nanoparticle at subwavelength distances from a membrane”. *Phys. Rev. A* 98 (1), p. 013851, 2018.
- [67] L. Landau and E. Lifshitz. “Chapter III - The Gibbs Distribution”. In: *Statistical Physics (Third Edition)*. Ed. by L. Landau and E. Lifshitz. Third Edition. Oxford: Butterworth-Heinemann, 1980, p. 79.
- [68] L. Novotny. “Strong coupling, energy splitting, and level crossings: A classical perspective”. *Am. J. Phys* 78 (11), p. 1199, 2010.
- [69] E. Schwerin. “Ober Spannungen und Formänderungen kreisringformiger Membranen.” *Ztschr. f. angew. Math. und Mech.* 6, p. 482, 1929.
- [70] C. Jin, A. Davoodabadi, J. Li, Y. Wang, and T. Singler. “Spherical indentation of a freestanding circular membrane revisited: Analytical solutions and experiments”. *J. Mech. Phys. Solids* 100 (August 2016), p. 85, 2017.
- [71] B. J. Davis, M. Dogan, B. B. Goldberg, W. C. Karl, M. S. Ünlü, and A. K. Swan. “4Pi spectral self-interference microscopy”. *J. Opt. Soc. Am. A* 24 (12), p. 3762, 2007.
- [72] L. Dai, I. Gregor, I. von der Hocht, T. Ruckstuhl, and J. Enderlein. “Measuring large numerical apertures by imaging the angular distribution of radiation of fluorescing molecules”. *Opt. Express* 13 (23), p. 9409, 2005.
- [73] J. D. Thompson, T. G. Tiecke, N. P. de Leon, J. Feist, A. V. Akimov, M. Gullans, A. S. Zibrov, V. Vuletic, and M. D. Lukin. “Coupling a Single Trapped Atom to a Nanoscale Optical Cavity”. *Science* 340 (6137), p. 1202, 2013.

-
- [74] L. Magrini, R. A. Norte, R. Riedinger, I. Marinković, D. Grass, U. Delić, S. Gröblacher, S. Hong, and M. Aspelmeyer. “Nanophotonic near-field levitated optomechanics”. *arXiv 1804.06676* 2018.
- [75] S. Kuhr. “Deterministic Delivery of a Single Atom”. *Science* 293 (5528), p. 278, 2001.
- [76] D. Schrader, S. Kuhr, W. Alt, M. Müller, V. Gomer, and D. Meschede. “An optical conveyor belt for single neutral atoms”. *Appl. Phys. B: Lasers Opt.* 73 (8), p. 819, 2001.
- [77] T. Čižmár, M. Šiler, M. Šerý, P. Zemánek, V. Garcés-Chávez, and K. Dholakia. “Optical sorting and detection of submicrometer objects in a motional standing wave”. *Phys. Rev. B* 74 (3), p. 035105, 2006.
- [78] D. Grass, J. Fesel, S. G. Hofer, N. Kiesel, and M. Aspelmeyer. “Optical trapping and control of nanoparticles inside evacuated hollow core photonic crystal fibers”. *Appl. Phys. Lett.* 108 (22), p. 221103, 2016.
- [79] A. Lambrecht and S. Reynaud. “Casimir force between metallic mirrors”. *Eur. Phys. J. D* 16 (1-3), p. 309, 2000.
- [80] H. B.G. C. Polder and D. “The influence of retardation on the London-van der Waals forces”. *Phys. Rev.* 73, p. 360, 1948.
- [81] D. Allan. “Statistics of atomic frequency standards”. *Proc. IEEE* 54 (2), p. 221, 1966.
- [82] J. Gieseler and J. Millen. “Levitated Nanoparticles for Microscopic Thermodynamics—A Review”. *Entropy* 20 (5), p. 326, 2018.
- [83] M Tschikin, S.-A. Biehs, F. Rosa, and P. Ben-Abdallah. “Radiative cooling of nanoparticles close to a surface”. *Eur. Phys. J. B* 85 (7), p. 233, 2012.

- [84] A. I. Volokitin and B. N. Persson. “Theory of friction: The contribution from a fluctuating electromagnetic field”. *J. Phys. Condens. Matter* 11 (2), p. 345, 1999.
- [85] N. Barbour and G. Schmidt. “Inertial sensor technology trends”. *IEEE Sens. J.* 1 (4), p. 332, 2001.
- [86] M. Kraft, M. M. Farooqui, and A. G. R. Evans. “Modelling and Design of an Electrostatically Levitated Disk for Inertial Sensing Applications”. *J. Micromechanics Microengineering* 11, p. 423, 2001.
- [87] B. Ando, S. Baglio, V. Marletta, and A. Valastro. “Short-Range Inertial Sensor Exploiting Magnetic Levitation and an Inductive Readout Strategy”. *IEEE Trans. Instrum. Meas.* 67 (5), p. 1238, 2018.
- [88] J. Prat-Camps, C. Teo, C. C. Rusconi, W. Wieczorek, and O. Romero-Isart. “Ultrasensitive Inertial and Force Sensors with Diamagnetically Levitated Magnets”. *Phys. Rev. Appl* 8 (3), p. 034002, 2017.
- [89] J.-O. Nilsson and I. Skog. “Inertial sensor arrays — A literature review”. In: *2016 European Navigation Conference (ENC)*. ii. IEEE, 2016, p. 1.
- [90] M. Imboden and P. Mohanty. “Dissipation in nanoelectromechanical systems”. *Phys. Rep.* 534 (3), p. 89, 2014.
- [91] L. Neumeier, R. Quidant, and D. E. Chang. “Self-induced back-action optical trapping in nanophotonic systems”. *New J. Phys.* 17 (12), p. 123008, 2015.
- [92] N. Descharmes, U. P. Dharanipathy, Z. Diao, M. Tonin, and R. Houdré. “Observation of Backaction and Self-Induced Trapping in a Planar Hollow Photonic Crystal Cavity”. *Phys. Rev. Lett.* 110 (12), p. 123601, 2013.

-
- [93] M. L. Juan, R. Gordon, Y. Pang, F. Eftekhari, and R. Quidant. “Self-induced back-action optical trapping of dielectric nanoparticles”. *Nat. Phys.* 5 (12), p. 915, 2009.
- [94] P. Mestres, J. Berthelot, S. S. Acimovic, and R. Quidant. “Unraveling the optomechanical nature of plasmonic trapping”. *Light Sci. Appl* 5 (7), e16092, 2016.
- [95] P. Padhy, M. Zaman, P. Hansen, and L. Hesselink. “On the substrate contribution to the back action trapping of plasmonic nanoparticles on resonant near-field traps in plasmonic films”. *Opt. Express* 25 (21), p. 5581, 2017.
- [96] P. Schein, P. Kang, D. O’Dell, and D. Erickson. “Nanophotonic Force Microscopy: Characterizing Particle–Surface Interactions Using Near-Field Photonics”. *Nano Lett.* 15 (2), p. 1414, 2015.
- [97] R. Messina, M. Tschikin, S.-A. Biehs, and P. Ben-Abdallah. “Fluctuation-electrodynamics theory and dynamics of heat transfer in systems of multiple dipoles”. *Phys. Rev. B* 88 (10), p. 104307, 2013.
- [98] D. Polder and M. Van Hove. “Theory of radiative heat transfer between closely spaced bodies”. *Phys. Rev. B* 4 (10), p. 3303, 1971.
- [99] J. Loomis and H. Maris. “Theory of heat transfer by evanescent electromagnetic waves”. *Phys. Rev. B* 50 (24), p. 18517, 1994.
- [100] A. I. Volokitin and B. N. J. Persson. “Radiative heat transfer between nanostructures”. *Phys. Rev. B* 63 (20), p. 205404, 2001.
- [101] A. Narayanaswamy, S. Shen, and G. Chen. “Near-field radiative heat transfer between a sphere and a substrate”. *Phys. Rev. B* 78 (11), p. 115303, 2008.

REFERENCES

- [102] J. P. Mulet, K. Joulain, R. Carminati, and J. J. Greffet. “Nanoscale radiative heat transfer between a small particle and a plane surface”. *Appl. Phys. Lett.* 78 (19), p. 2931, 2001.
- [103] A. E. R. Lopez, C. Gonzalez-Ballester, and O. Romero-Isart. “Internal Quantum Dynamics of a Nanoparticle in a Thermal Electromagnetic Field: a Minimal Model”. *arXiv 1807.03811* 2018.
- [104] J. B. Pendry. “Radiative exchange of heat between nanostructures”. *J. Phys.: Condens. Matter* 11 (35), p. 6621, 1999.
- [105] M. Krüger, T. Emig, and M. Kardar. “Nonequilibrium Electromagnetic Fluctuations: Heat Transfer and Interactions”. *Phys. Rev. Lett.* 106 (21), p. 210404, 2011.
- [106] C. Otey and S. Fan. “Numerically exact calculation of electromagnetic heat transfer between a dielectric sphere and plate”. *Phys. Rev. B* 84 (24), p. 245431, 2011.
- [107] M. Laroche, R. Carminati, and J. J. Greffet. “Near-field thermophotovoltaic energy conversion”. *J. Appl. Phys.* 100 (6) 2006.
- [108] S. Basu, Z. M. Zhang, and C. J. Fu. “Review of near-field thermal radiation and its application to energy conversion”. *Int. J. Energy Res.* 33 (13), p. 1203, 2009.
- [109] W. A. Challener et al. “Heat-assisted magnetic recording by a near-field transducer with efficient optical energy transfer”. *Nat. Photonics* 3 (4), p. 220, 2009.
- [110] E. Rousseau, A. Siria, G. Jourdan, S. Volz, F. Comin, J. Chevrier, and J. J. Greffet. “Radiative heat transfer at the nanoscale”. *Nat. Photonics* 3 (9), p. 514, 2009.
- [111] B. Guha, C. Otey, C. B. Poitras, S. Fan, and M. Lipson. “Near-field radiative cooling of nanostructures”. *Nano Lett.* 12 (9), p. 4546, 2012.

-
- [112] *Cystran UV-visible-IR specialist optics*. URL: <https://www.cystran.co.uk/optical-materials/zinc-selenide-znse>.
- [113] G. V. Dedkov and A. A. Kyasov. “Electromagnetic friction forces on the scanning probe asperity moving near surface”. *Phys. Lett. A* 259 (1), p. 38, 1999.
- [114] M. Tomassone and A. Widom. “Electronic friction forces on molecules moving near metals”. *Phys. Rev. B* 56 (8), p. 4938, 1997.
- [115] R. Reimann, M. Doderer, E. Hebestreit, R. Diehl, M. Frimmer, D. Windey, F. Tebbenjohanns, and L. Novotny. “GHz Rotation of an Optically Trapped Nanoparticle in Vacuum”. *Phys. Rev. Lett.* 121 (3), p. 033602, 2018.
- [116] J. Ahn, Z. Xu, J. Bang, Y. H. Deng, T. M. Hoang, Q. Han, R. M. Ma, and T. Li. “Optically Levitated Nanodumbbell Torsion Balance and GHz Nanomechanical Rotor”. *Phys. Rev. Lett.* 121 (3), p. 33603, 2018.
- [117] F. Monteiro, S. Ghosh, E. C. van Assendelft, and D. C. Moore. “Optical rotation of levitated spheres in high vacuum”. *Phys. Rev. A* 97 (5), p. 051802, 2018.

List of Publications

Publication Related to this Thesis

Diehl, R., Hebestreit, E., Reimann, R., Tebbenjohanns, F., Frimmer, M., and Novotny, L. *Optical levitation and feedback cooling of a nanoparticle at subwavelength distances from a membrane*. Physical Review A, **98**(1), 013851 (2018).

Other Publications by the Author

Reimann, R., Doderer, M., Hebestreit, E., **Diehl, R.**, Frimmer, M., Windey, D., Tebbenjohanns, F. and Novotny, L. *GHz Rotation of an Optically Trapped Nanoparticle in Vacuum*. Physical Review Letters, **121**(3), 033602 (2018).

A. Descombin, P. Poncharal, A. Pascale-Hamri, M. Choueib, **R. Diehl**, P. Vincent, S.T. Purcell, A. Ayari, and S. Perisanu *Giant, Voltage Tuned, Q-factors of Single Wall Carbon Nanotubes and Graphene at Room Temperature*. Submitted (2018).

Diehl, R., Choueib, M., Choubak, S., Martel, R., Perisanu, S., Ayari, A., Vincent, P., Purcell, S.T. and Poncharal, P. to be published (2019).

Curriculum Vitae

Rozenn Diehl, born on September 28th, 1991 in Saint-Nazaire, France

Professional Experience

- 2014–2018 Doctoral Student and Research Assistant
Photonics Laboratory, ETH Zurich, Switzerland
- 2014 Research Assistant
Institut Lumière-Matière, Lyon, France
- 2013 Research Assistant
Institut des Sciences Analytiques, Lyon, France
- 2013 Research Assistant
Laboratoire de Mécanique des Contacts et des Structures, Lyon, France
- 2012 Research Assistant
Laboratoire de Spectroscopie Ionique et Moléculaire, Lyon, France

Education

- 2012–2014 Master of Science, Nanoscale Engineering
Ecole Centrale de Lyon, Lyon, France
- 2011–2012 Bachelor of Science, Physics
Université Claude Bernard, Lyon, France
- 2009–2011 Classes Préparatoires aux Grandes Ecoles, Math-Physics
Lycée du Parc, Lyon, France